

***RAPID DIFFUSION IN THE  
BRAIN EXTRACELLULAR  
SPACE – BIOPHYSICAL  
CONSTRAINTS AND  
PHYSIOLOGICAL  
IMPLICATIONS***

Candidate: Mr. Kaiyu Zheng

Supervisor: Prof. Dmitri Rusakov

Co-supervisor: Prof. Matthew Walker

First Submission: 11 September 2008

Final Submission: 21 January 2009



I, Kaiyu Zheng, declare that this thesis and the work presented in it are my own and has been generated by me as the result of my own original research. Where I have consulted the published or unpublished work of others, this is always clearly attributed. Parts of this work have been published or in the process of publication (see Publications section for details).

# Abstract

Physiological experiments backed by biophysical models have shown that, in central glutamatergic synapses, changes in extracellular diffusivity or glutamate transporter functions exert significant influences on the excitatory transmission. Failures of transporter functions have also been related to neurological disorders. The underlying biophysical mechanisms remain poorly understood.

Here, we first combine two-photon excitation imaging with electrophysiology to estimate the diffusivity of small soluble molecules, such as glutamate in the hippocampal neuropil (area CA1). Next, we adopt time-resolved fluorescence anisotropy imaging microscopy to establish the previously unknown instantaneous diffusivity of small molecules in the extracellular space. The result indicates that nanometer-scale diffusivity in the brain extracellular space is 25-30% slower than that in free medium. Accounting for this retardation may have fundamental consequences for accurate interpretation of diffusion-limited reactions in the brain.

To obtain insight into the mechanisms contributing to the excitatory signal formation, we incorporate these results in a newly developed Monte-Carlo model of the typical environment of small excitatory synapses including unevenly distributed receptors and transporters. In addition, we build a macroscopic three-dimensional compartmental model of the hippocampal neuropil based on available experimental data to examine the effect of transporter distribution on the extracellular landscape of glutamate.

Monte-Carlo simulations show to what extent altering diffusivity inside or outside the synaptic cleft affect synaptic responses. Modelling also predicts that extrasynaptic transporters have little effect on fast synaptic transmission through AMPARs and NMDARs. However, they influence the responses of high-affinity extrasynaptic receptors, such as NMDA or metabotropic receptors. Conversely, intracleft glutamate transporters should significantly attenuate activation of synaptic transmission. On a larger neuropil scale, failure of >95% transporters is required for any significant elevation of glutamate (above 1-2  $\mu\text{M}$ ) to occur.

Our data shed light on fundamental biophysical constraints important for a better understanding of excitatory signal formation in central neural circuits.

# Contents

Abstract .....	3
Contents .....	4
List of Figures.....	6
List of Tables and Equations .....	8
List of Abbreviations.....	9
Publications .....	10
Acknowledgment.....	11
CHAPTER 1. Introduction .....	12
1.1. Diffusion of Neurotransmitters Shapes Synaptic Transmission.....	13
1.2. Extracellular Diffusivity as an Indicator of Neurological Disorders.....	16
1.3. The Hippocampus as a Subject of Investigation .....	18
1.4. Diffusion in Complex Environments.....	20
1.5. Existing Methods of Diffusivity Measurement in the Brain Extracellular Space	23
CHAPTER 2. Methods .....	29
2.1. Experimental Preparation .....	29
2.2. Electrophysiology .....	29
2.3. Two-photon Excitation Imaging of a Point Source Diffusion .....	30
2.4. Computational Models and Simulations .....	35
2.4.1. Three-Dimensional Monte-Carlo Simulation of Synaptic Transmission .....	35
2.4.2. Three-Dimensional Compartmental Model for Macroscopic Diffusion .....	43
2.5. Time-Resolved Fluorescent Anisotropy Imaging Microscopy (TRFAIM).....	46
2.5.1. Theoretical Background .....	46
2.5.2. Technical Setup .....	56
2.5.3. Protocol .....	57
2.5.4. Analysis Method .....	58
CHAPTER 3. Results: Measurement of Extracellular Diffusivity in The Hippocampal Neuropil – A Macroscopic View .....	62
CHAPTER 4. Results: Diffusion Coefficient of Glutamate in The Synaptic Cleft Estimated Using Dextran Retardation – A Microscopic View .....	66
CHAPTER 5. Results: Instantaneous Diffusion of Small Molecules in The Brain Extracellular Space Measured Using TRFAIM – A Nanoscopic View.....	71

---

CHAPTER 6. Results: Diffusion of Glutamate in the Synaptic Cleft and its Influence on Postsynaptic Responses – A Microscopic View.....	74
CHAPTER 7. Results: Extracellular Landscape of Glutamate in The Neuropil – A Macroscopic View .....	83
CHAPTER 8. Discussion.....	86
Bibliography.....	97
Appendix A. Two-Dimensional Monte-Carlo Model.....	107
Appendix B. Derivation of photo-bleaching factor .....	111
Appendix C. Linux Cluster Configuration .....	112
Appendix D. Three-Dimensional Compartmental Model Pseudo Code .....	115
Appendix E. Three Dimensional Monte-Carlo Model Pseudo-Code .....	116
Appendix F. Point Source Analysis Pseudo-Code .....	117
Appendix G. TR-FAIM Analysis Pseudo-Code.....	118

# List of Figures

Figure 1 Extracellular Field Potential in CA1 and CA3 of Hippocampus after Diffusion Measurements Indicate Unchanged Physiological Viability.....	30
Figure 2 Two-Photon Scanning Point Source Diffusion Setup Schematic.....	31
Figure 3 Micropipette Dimension and 2D Gaussian Profile of Ejected Indicator ....	32
Figure 4 Gaussian Diffusion Profile of a point-source and a spherical source at $t = 100\text{ms}$ , $300\text{ms}$ .....	33
Figure 5 Point Source: Fitting a theoretical curve to the experimental profile .....	35
Figure 6 AMPAR, NMDAR and EAAT1-2/EAAT3 kinetic schematics .....	37
Figure 7 A Monte-Carlo model of the characteristic Schaffer collateral CA1 pyramidal cell synapse .....	40
Figure 8 3D Monte Carlo Simulation Test Schemes .....	42
Figure 9 Diffusion Equivalence between Monte Carlo and Compartmental Model	45
Figure 10 Illustration of TRFAIM Principle.....	47
Figure 11 Illustration of Linearity between rotational and translational diffusivity	50
Figure 12 Single Components of Time-dependant anisotropy decay.....	51
Figure 13 Rotational Correlation Time in Fixed-tissue samples.....	52
Figure 14 Hippocampal CA1 Under Cross-polariser Imaging Show Birefringence...	53
Figure 15 Photobleaching is roughly linear for sequential acquisition and can be corrected for.....	54
Figure 16 Correction for Photobleaching and G-factor.....	55
Figure 17 TRFAIM Optical Setup Schematic .....	56
Figure 18 Slice Transportation Chamber Schematic .....	57
Figure 19 TRFAIM Analysis Procedure.....	58
Figure 20 Analysis programme recovers predefined image template.....	59
Figure 21 Measurement of extracellular diffusivity in the CA1 <i>s.r.</i> using point source diffusion .....	63
Figure 22 Diffusion Retardation of extracellular AF350 by Dextran in hippocampal neuropil .....	67
Figure 23 Diffusion Retardation by Dextran Affects Postsynaptic Responses.....	68
Figure 24 Estimating the intrasynaptic diffusivity of glutamate .....	69
Figure 25 A Map of Instantaneous Extracellular Diffusivity in Area CA1 of the Hippocampus.....	73

---

Figure 26 Effects of Transporter Distance and Coverage Symmetry (2D MC Model) on Fast Synaptic Responses.....	75
Figure 27 Effect of Transporter Density (MC Models) .....	77
Figure 28 Transporter Effect on Repetitive Stimulation .....	78
Figure 29 Intrasympaptic Transporter Effect on AMPARs responses .....	79
Figure 30 TBOA Experiments.....	79
Figure 31 Extrasynaptic Receptors .....	81
Figure 32 Macroscopic Glutamate Density Affects Glutamate Concentration Gradient.....	84
Figure 33 Macroscopic Transporter Density Shapes Glutamate Concentration Gradient.....	85
Figure 34 Scales of Diffusion of Glutamate (modified from Nicholson <i>et al.</i> , 2001).....	89
Figure 35 Two-dimensional Monte Carlo Simulation Environment.....	108
Figure 36 2D Monte Carlo Simulation Test Scenarios.....	109
Figure 37 PC Cluster Image.....	112

# List of Tables and Equations

Table 1 AMPAR, NMDAR, EAAT1/2, EAAT3 Reaction Kinetic Scheme Constants .....	38
Table 2 Summary of Glutamate Diffusivity at Different Scales .....	88
Equation 1 Point Source Diffusion Equation in Spherical Coordinate .....	33
Equation 2 Compartmental Model Simple Forward Step Scheme .....	44
Equation 3 Time Dependent fluorescent anisotropy calculated from experimental measures .....	46

## List of Abbreviations

ACSF	Artificial Cerebral Spinal Fluid
ADC	Apparent Diffusion Coefficient
AF350	Alexa Fluor 350
AMPA	Alpha-amino-3-hydroxy-5-methyl-4-isoxazolepropionic acid
AMPA	AMPA receptor
CA1, CA3	Cornu Ammonis 1,3
CSF	Cerebral Spinal Fluid
DIC	Differential Interference Contrast
DW-MRI	Diffusion Weighted Magnetic Resonance Imaging
EAAT	Excitatory Amino Acid Transporter
ECS	Extracellular Space
EM	Electron Microscopy
EPSC	Excitatory Post Synaptic Current
fm	Free Medium, notation convenience, equivalent to ACSF
FRAP	Fluorescence Recovery After Photobleaching
FCS	Fluorescence Correlation Spectroscopy
IOI	Integrated Optical Imaging
MC	Monte Carlo
mEPSC	miniature Excitatory Post Synaptic Current
mGluR	metabotropic Glutamate Receptor
MRI	Magnetic Resonance Imaging
NA	Numerical Aperture
NMDA	N-methyl D-aspartate
NMDAR	NMDA receptor
PMT	Photo-multiplier tube
ROI	Real-time Optical Imaging
s.o.	stratum oriens
s.p.	stratum pyramidale
s.r.	stratum radiatum
TCSPC	Time Correlated Single Photon Counting
TRFAIM	Time-Resolved Fluorescence Anisotropy Imaging Microscopy
TTX	Tetradotoxin

# Publications

## Papers

Zheng K, Scimemi A, Rusakov DA (2008) Receptor actions of synaptically released glutamate: the role of transporters on the scale from nanometres to microns. *Biophys J*, Vol 95, 4584-4596(doi:10.1529/biophysj.108.129874).

Zheng K, Levitt JA, Sargent N, Suhling K, Rusakov DA (2008) Nanodiffusion in the brain extracellular space (submitted, in revision).

Henneberger C, Popov V, Medvedev N, Kraev I, Zheng K, Rusakov DA, Stewart MG (2008) Astroglia selectively approach synapses on thin dendritic spines (submitted, in revision).

Zheng K, Savtchenko L, Pucovska U, Rusakov DA (2008) The intra-cleft diffusion coefficient of glutamate (in preparation).

## Abstracts

Zheng K, Rusakov DA; *Extracellular transients of neurotransmitter: space and time constraints for release and uptake*; British Neuroscience Assoc. Abstr., vol 18, P89, 2005

Zheng K, Savtchenko LP, Rusakov DA; *Diffusion of glutamate in the synaptic cleft*; Proc Physiol Soc 3, PC171, 2006

Rusakov D. A., Pucovska U., Savtchenko L. P. & Zheng K; *Rapid actions of glutamate in the synaptic environment*; FENS Abstr., vol. 3, A064.4, 2006

# Acknowledgment

I would like to first of all thank Dmitri Rusakov for have given me the opportunity to dip my head into the field of neuroscience four years. Over the four years, Dmitri has altruistically provided many valuable discussion and guidance which sometimes with ignorance and stubbornness I failed to follow. I am truly grateful to all the possible support Dmitri has provided me with in order to make all these works come true.

I am extremely glad that collaboration with Klaus Suhling at King's College whom has been most generous in providing equipments and discussion, has produced fruitful results.

I am also greatly indebted to the MRC, if not for their generous financial support over the three years; it would not have been possible to finish the works that are being presented here.

Many colleagues in the experimental epilepsy department have introduced me with great patience to the world of biological science, particularly Ricardo Scott, Annalisa Scimemi, Arnaud Ruiz, Dimitri Kullmann, Christian Hennenberger, Leonid Savtchenko and Joost Heeroma.

Finally, an impassionate tribute to my grandparents, my aunt and uncle and parents, for sacrificing part of their lives so that I could fullfill mine.

## CHAPTER 1. INTRODUCTION

The neuron doctrine postulates that the functional unit of the brain is the neuron. The term neuron was first coined by Wilhelm von Waldeyer in 1891 after Cajal's extensive histological and anatomical observations of cerebellum using Golgi's silver chromate salt staining technique. Cajal's discovery and Golgi's staining method were presented at their 1906's Nobel Prize lectures (Cajal, 1906; Golgi, 1906). Histological studies by His and von Kölliker during 1890s showed the axo-dendritic structures of neurons. It is then evident that signal transduction of nerve impulses between neurons must occur at axonal and dendritic contacts. However the transduction mechanism at such site was not known. Otto Loewi's famous experiments in 1921 finding that vagus nerve control heart rate via acetylcholine (Kandel *et al*, 2000) propelled the chemical transduction mechanism as a more likely candidate for nerve impulse propagation. Experiments in neuromuscular junction where curare blocks excitation from Claude Bernard's experiments showed similar chemical transduction mechanism. Henry Dale also carried out systematic studies with acetylcholine as a chemical transmission molecule (Dale, 1936). Dale and Loewi shared the Nobel Prize for their works on the chemical transmission between nerves. However the debate between synaptic electrical and chemical transmission was not conclusive. One of the main believers in electrical transmission was John Eccles, based on slow time course of vagus inhibition and other peripheral nervous systems. By the 1940s, both Stephen Kuffler (Kuffler, 1942) and Eccles (Eccles, 1982) himself measured synaptic delays in neuromuscular junction and central nervous systems, from which results could only be explained by chemical transmission hypothesis as electrical transmission hypothesis should not result in delay at synapses. With the advance in electron microscopy, detail structure of the synapse could be visualised (Robertis & Bennett, 1955). Chemical transduction has since been proven to be by far the most common transduction mechanism in all major transmissions between neurons in central nervous systems.

The chemical transmission involves five basic steps. The nerve action potential arrives at the presynaptic terminal. The action potential triggers

release of neurotransmitters. The neurotransmitters diffuse in the extracellular space until they reach ligand binding sites and bind with certain probability. The bound proteins, if are receptors, would undergo conformational changes to allow small ions flow through them, hence change local ion concentrations and the transmembrane potentials. This change subsequently allows action potentials to be generated at the postsynaptic terminals and propagate further. This reliance on chemicals being released into the synaptic cleft between neuronal synaptic terminals as messengers for channel activations signifies the great importance of diffusion-reaction processes of such particles in the compact extracellular environment. There are considerable facts in the process of chemical transduction, ranging from release mechanism to interactions between many proteins.

In this thesis, we shall focus on the process of diffusion and diffusion-reaction during the chemical transmission. In particular we aim first to establish the fundamental property of diffusivity for neurotransmitter glutamate in the synaptic cleft, extracellular space outside the synaptic cleft and apparent diffusivity over large volume of tissues containing thousands of synapses. Then we shall use biophysical models to examine effects of diffusion-reaction process on synaptic transmission and over large volume of tissues containing thousands of synapses. The diffusion of neurotransmitter is not only important because it is a fundamental physical property in the chemical transmission, but also because water self-diffusion changes (i.e. equivalent to intrinsic medium viscosity) have been observed in many neurological disorders such as epilepsy.

### **1.1. Diffusion of Neurotransmitters Shapes Synaptic Transmission**

The brain, in simplistic terms, is a porous medium filled with chemicals arranged in specific ways to undergo specific chemical reactions. As with most chemical reactions, the rates of reaction are diffusivity-dependent and concentration-dependant. At the simplest level, the visual structure of the

brain mainly consists of white matter and gray matter, which represent, respectively myelinated cell axons, and cell bodies with non-myelinated axons and dendrites. All these cell structures are extremely densely packed as one can visualise in using ultra-thin slices of brain tissue under high-resolution transmission electron microscopy. This packaging corresponds to a spatially highly tortuous and complex extracellular environment where neurotransmitters such as glutamate are released into the extracellular space and diffuse rapidly until they react with other membrane surface proteins such as receptors and transporters. These reactions can lead to protein conformation changes and allow selective ions to be transported cross the membrane through protein channels; this changes the local membrane potential, from which the signal can be propagated. In order to satisfy conditions for activating certain numbers of receptors (or any other binding proteins such as transporters), a required amount of neurotransmitters have to be present locally through means of diffusion in the highly crowded and complex extracellular space, where parameters such as tortuosity, effective surface reactant affinities and medium viscosities, will all be important factors. However, the strength of influences on signal transduction from those different factors will differ depending on the spatial and temporal scales we examine, because some factors such as tortuosity only become significant beyond few hundreds of nanometres whereas other factors such as medium viscosity influences at nanometer scales.

On a short time scale of  $10^{-6}$ ~ $10^{-9}$ s and within  $10^{-7}$ ~ $10^{-9}$ m in space (approximate distance the neurotransmitter would've diffused in that amount of time), the passive diffusion of neurotransmitters mainly takes place in the synaptic cleft area and shapes the fast synaptic transmission profile through the activation of fast ionotropic receptor channels such as Alpha-amino-3-hydroxy-5-methyl-4-isoxazolepropionic acid receptors (AMPA) and N-methyl D-aspartate receptors (NMDARs)(Otis *et al.*, 1996). Diffusion in the cleft could be very different from normal aqueous diffusion as the medium composition is different (Longsworth, 1953; Berstad, 1988). The high density protein matrix in the cleft may also cause anisotropic diffusion (Sykova & Vargova, 2007), where diffusion has preferential directions due to highly

directional structures in the spatial domain. Electric fields generated in the synaptic cleft after release due to ion flows interacting with charged neurotransmitter like glutamate, have also been shown to slow down diffusion of glutamate (Savtchenko *et al.*, 2000; Savtchenko *et al.*, 2005; Sylantsev *et al.*, 2008), although the rising phase of the postsynaptic response is not significantly affected by such influences there are noticeable effect on the falling phase of the postsynaptic responses. Various factors that change the diffusion of neurotransmitters would ultimately give rise to a change in the time course of the neurotransmitter concentration profile. This consequently changes the fast synaptic responses as shown in recent study of the effects of increasing high affinity receptor activation via diffusion retardation (Min *et al.*, 1998). The causes of diffusion profile change arises from many different mechanisms such as medium viscosity, molecular buffering, but the ultimate result is that they change diffusivity of the chemicals in the synaptic environment and it is this change in diffusion whether it is prolonged lingering or hastened dissipation, that modulates fast synaptic responses.

On a medium time scale of  $10^{-3}\sim 10^{-6}$ s and spatial scale of  $10^{-6}\sim 10^{-7}$ m, which includes the perisynaptic region, the transporters on the glial membranes near the synaptic cleft could alter diffusion profiles (Diamond & Jahr, 1997; Diamond 2001; Lehre & Rusakov, 2002) by trapping neurotransmitters near the synaptic cleft. This in turn changes the postsynaptic response, mainly by reducing activation of high-affinity NMDA receptors but not low affinity AMPA receptors (due to insufficient number) in the extrasynaptic regions by prolonging the concentration of glutamate around the synaptic cleft (Otis *et al.*, 1996; Holmes, 1995). Conversely, the blockade of such transporters results in significant increases in the postsynaptic responses (Diamond & Jahr, 1997; Tong & Jahr, 1994). Experimental observations of physiological alterations in extracellular diffusivity due to osmotic challenge, intense excitation and glial changes have been reported (Kume-kick *et al.*, 2002; Chen & Nicholson, 2000; Krizaj *et al.*, 1996; Hrabetova *et al.*, 2003). Altering the transporter density or distribution could also affect the diffusion profile significantly outside even the perisynaptic area (Lehre & Rusakov, 2002). The effect of the buffering provided by the transporters could then work as a shield

against the spill-in effect from neighbouring synapses, as well as extend influence on specific neighbouring synapses through spill-over (Arnth-Jensen *et al.*, 2002; Diamond, 2002; Rusakov, 2001; Piet *et al.*, 2004; Diamond, 2001).

When considering on the time scale of  $10^0\sim 10^{-3}$ s and spatial dimensions of  $10^{-6}\sim 10^{-4}$ m, the tortuous and complex environment of the extracellular space (Nicholson & Sykova, 1998; Nicholson, 2001), in addition to proteins acting as source and sink for chemicals (Rice *et al.*, 1985; Kullmann, 1999), will affect long-range diffusion of signalling molecules. This type of signalling is often termed volume transmission. Changes in the long range diffusion could influence integrated network activities (Liang, 1995; Bhalla, 2004), the cross-talk effects between neighbouring pools of synapses (Sykova, 2004b; Piet *et al.*, 2004). The sink and source roles different proteins play, such as glutamate transporter internalise glutamate molecules in the extracellular space, cause ambient chemical concentration gradient to form as coverage and properties of proteins and cells that expresses those proteins differ from region to region. By modulating ambient neurotransmitter gradient, tonic activation mediated via different channels maybe influenced (Sah *et al.*, 1989; Eghbali *et al.*, 1997), which in turn could prompt the generation and spread of seizures (Demarque *et al.*, 2004; Tanaka *et al.*, 1997), and result in neurotoxicity phenomena (Wang *et al.*, 1998; Garthwaite *et al.*, 1992; Obrenovitch, 1999) related to neurological disorders.

## **1.2.Extracellular Diffusivity as an Indicator of Neurological Disorders**

Recent advances in high-field MRI (magnetic resonance imaging) and subsequent use of DW-MRI (diffusion weighted MRI) for diffusion measurement (Duong *et al.*, 2001), have been used to show changes in apparent diffusivity of water molecules and exogenous markers in the brain indicating various stages of ischemia (Silva *et al.*, 2002), epilepsy (Wiesmann *et al.*, 1997; Hakyemez *et al.*, 2005; Heiniger *et al.*, 2002), and other neurological disorders (Bozzalli & Cherubini, 2007; Dijkhuizen & Nicolay, 2003; Roberts & Rowley, 2003; Sotak, 2004). It has been shown that changes in ADC

(apparent diffusion coefficient) occur focally in patients with epilepsy even after a single seizure (Fabene *et al.*, 2003; Hufnagel *et al.*, 2003). It has been however difficult to determine whether such diffusion changes are intracellular or extracellular (Harris *et al.*, 2000; Krizaj *et al.*, 1996; Norris, 2001). Part of the difficulty lies within the spatial and temporal resolution of the MRI scans (on the scale of seconds and hundreds of micrometres). Many theories have been proposed to quantify and localise the actual changes in diffusivity that represent the observed effects. Most of these involve the changes of extracellular space due to water molecule migration between the intra- and extra-cellular space causing cells to swell or shrink. There is a current debate about the aetiology of the experimental results from DW-MRI (Roth *et al.*, 2008; Duong *et al.*, 1998), and the origin of ADC change.

It is difficult to find any mechanistic association between detected diffusivity values and the causes of neurological pathology without an accurate knowledge on the scale of extracellular space (on the order of 10nm), which is where the real diffusion changes take place whether in extracellular or intracellular space. Some recent studies have shown changes in extracellular environment and diffusivity during transient ischemia (Homola *et al.*, 2006; Qiao *et al.*, 2002; Perez-pinon *et al.*, 1995) and extracellular diffusivity changes during brain edema (Hrabetova *et al.*, 2003), but have not ruled out simultaneous changes in intracellular diffusivity. Knowledge of the origin of these diffusivity changes and consequences of these changes plays a critical role in identifying underlying causes in neurological disorders.

Epilepsy is one of the most common neurological diseases. It has been estimated that 1 in every 100 people is affected by the condition to various degrees (WHO, 2001). It is also a neurological disease with well accumulated knowledge ever since ancient Greek times. Though the mechanisms of epileptogenesis are still poorly understood, but majority arise from genetic defects and abnormal cell structures due to trauma or infections. Epileptogenesis partly result from malfunctions or mutations in common excitatory components such as glutamatergic transporters (Tanaka *et al.*, 1997; Eid *et al.*, 2008), NMDA receptors (Bayer *et al.*, 1995; Mikuni *et al.*, 1999) and

ion channels (Kullmann, 2002; Rhodes *et al.*, 2005). The hippocampus has high density of such excitatory transmissions as well as being one of the major damage areas in numerous types of epileptic patients, which suggest hippocampus as a prime subject for study. A number of hypotheses with regard to the causes of seizure have been drawn from experiments suggesting possible involvement of extracellular K<sup>+</sup> concentration changes (Bihi *et al.*, 2005; Heinemann *et al.*, 1986; Fisher *et al.*, 1976), gap junctions (Lee *et al.*, 1995; Traub *et al.*, 2001) and Na<sup>+</sup> channel malfunctions (Meisler & Kearney, 2005), diffusivity changes (Kimiwada *et al.*, 2006).

Apart from channel mutations, changes in hippocampal morphology, cellular redistribution, neuronal death, and gliosis (Bahh *et al.*, 1999; Gorter *et al.*, 2003), whether as a consequence of trauma or previous seizures, can also exacerbate further seizures. These structural changes will result in diffusion profile changes (generally a reduction in ADC), which one can detect using DW-MRI. This has been used as a tool to isolate regions of seizure focal point (Diehl, 2001 *et al.*; Wieshmann *et al.*, 1999). Despite diffusion changes measured with MRI and DW-MRI are being routinely carried out in epileptic patient examinations, they are at the moment only useful for locate problematic volumes. Therefore, measuring diffusion changes at smaller spatial scales, how do they correlates to DW-MRI measurements, understanding how these diffusion changes affects signal transductions and ultimately find the reasons for the changes in diffusion, are important for epilepsy treatments and diagnosis.

### 1.3. The Hippocampus as a Subject of Investigation

Diffusion changes detected by MRI in the hippocampus have been related to many forms of epilepsy (Kimiwada *et al.*, 2006; Wieshmann *et al.*, 1999). The cellular organisation and synaptic circuitry in hippocampus have been intensely studied and are well-established. The three-dimension structure of hippocampal Schaffer collaterals – CA1 pyramidal cell synapses has been documented in great detail (Ventura & Harris, 1999; Schikorski & Stevens, 1997; Shepherd & Harris, 1998). Therefore, it is an ideal candidate for our study into the effect of diffusion on neural communication.

The distribution of the major excitatory ionotropic receptors, AMPA, NMDA, Kainate have been established through combinations of electrophysiology, fluorescence imaging, immunocytochemistry and electron microscopy (Nusser *et al.*, 1998; Tanaka *et al.*, 2005; Takumi *et al.*, 1999). The average number of AMPARs and NMDARs in the postsynaptic membrane of pyramidal cells in area CA1 (*stratum radiatum*) has been put at 80 and 20 respectively, and they tend to form in a Gaussian distribution from the centre of the postsynaptic membrane (Nusser *et al.*, 1998; Racca *et al.*, 2002; Tanaka *et al.*, 2005). In fact, immuno-specific labelling and electron microscopy (EM) methodologies have provided a static picture, since the results come from fixed tissues. In live preparations, a much more dynamical picture emerges including rapid receptors trafficking on the membrane (Choquet & Triller, 2003) and in and out of the membrane to the cellular reserves (Carroll *et al.*, 2001). However those processes generally takes place on a much longer time scale compare to the fast excitatory postsynaptic signals. On faster time scale compare to receptor trafficking, are the slower-acting metabotropic receptors (e.g. metabotropic glutamate receptors (mGluR1)). The fast excitatory postsynaptic signals mediated by the fast ionotropic receptors are on the scale of milliseconds, however with metabotropic receptors, the reaction kinetics and signal transduction pathways involve many protein reaction cascades which inevitably make them a lot slower. Hence we will not consider the metabotropic receptors due to the time scale we are investigating for fast synaptic transmissions and their relatively low population inside the synaptic cleft. The structure and kinetics of both ionotropic glutamatergic receptors AMPARs and NMDARs are well-known and studied (Jonas *et al.*, 1993; Bergles & Jahr, 1998; McBain & Mayer, 1994). This puts them in an ideal position for our simulation studies.

Another crucial player in the synaptic transmission is the glutamate transporters. Excitatory amino acid transporter (EAAT) 1, 2 and 3 are the major glutamatergic transporters (with different acronyms in rodent models) distributed in hippocampal areas in human (Lehre & Danbolt, 1998; Rothstein *et al.*, 1994; Mennerick *et al.*, 1998). Their binding kinetics are also relatively well-established (Wadiche *et al.*, 1995). They function by co-transport one H<sup>+</sup>

and three Na<sup>+</sup> ions, and the counter-transport of one K<sup>+</sup> ion (Erecinska & Silver, 1990). They are generally situated near synapses on glial membranes and are thought to provide shielding purposes (Bergles & Jahr, 1998; Oliet *et al.*, 2001; Rusakov, 2001; Tzingounis & Wadiche, 2007) by competing with local receptors. However the proximity of the transporters are different at different type of synapses, such as cerebella mossy-fibre and parallel-fibre synapses, from which contradictory results from transporter blockade experiments have been reported (Mennerick & Zorumski, 1995; Chaudhry *et al.*, 1995). The failure in transporters' functionalities could be potentially critical to local environment and possible neurotoxicity from neurotransmitters such as glutamate (Selkirk *et al.*, 2005). This also modifies the diffusion profile of the neurotransmitters and hence provides yet another route to possible signalling changes. The role of the glutamatergic transporters is still a hotly pursued topic, therefore we will aim to use biophysical models to examine their effects on synaptic transmission at a single synapse.

The geometry of synaptic environment in the hippocampus has been studied mainly using transmission electron microscopy. It has been argued the 'average' shape of a 'typical' hippocampal area CA1 synapse could be approximated using the superpositioned averages of many such synapses (Rusakov & Kullmann, 1998a). Such data enable a study of microscopic diffusions in the synaptic environment of hippocampal excitatory synapses. The larger-scale cellular environment is less well known, although many macroscopic parameters such as extracellular volume fractions and space tortuosity (Nicholson & Phillips, 1979; Nicholson & Sykova, 1998), average synapse density (Rusakov *et al.*, 1998; Geinisman *et al.*, 1992), transporter density are well-established. Space tortuosity and extracellular volume fractions have been extensively measured in the hippocampus in both normal and abnormal conditions (Sykova, 2005).

#### **1.4. Diffusion in Complex Environments**

Diffusion is a basic physical process of random particle movements in an attempt by the system to equilibrate any chemical potential that exists in an environment in order to maximise entropy. It obeys simple parabolic PDE

(partial differential equation) derived from continuity law ( $\partial C/\partial t = -\nabla \cdot j$ ) and Fick's first law ( $j = -D \cdot \nabla C$ ), which is  $\partial C/\partial t = D(\nabla^2 C)$ ; where  $C$  is the concentration,  $D$  is the diffusivity of particles,  $j$  is the flux of particles, . The relationship between macroscopic diffusion and microscopic movements (i.e. Brownian motion) in terms of the mean free path was established by Einstein in 1912.

Although diffusion process itself is simple, the complexity of the neuropil environment (spatial complexity impose non-3D tortuous diffusion pathway and chemical reaction complexity add temporal and spatial dependent chemical potentials) makes quantitative analysis difficult, if not impossible. In fact, numerical solutions to diffusion in porous media have been largely of interests to chemical engineers because catalysts used for chemical reactions are mostly porous solids, as well as concrete and soil erosions in mechanical engineering and geology, and polymer physics. Yet there are no theoretical solutions in those fields, therefore we are not aim to develop novel theoretical formulations for diffusion in complex environment but only to utilise numerical methods for biophysical simulations of such process.

Simplified views of homogeneous isotropic three dimensional diffusions as equations suggest with Fick's laws do not always apply to complex systems such as the brain extracellular space. Many forms of diffusion occur in such environments, for example directional preferences of diffusion due to cellular structures such as axons and dendrites results in macroscopic anisotropy (Sykova, 2004b). Anisotropic diffusion could also occur on a microscopic level due to scaffolding protein orientations (Sykova & Vargova, 2007). Anomalous diffusion, where mean squared displacement of a particle is not a linear function of time (i.e. do not obey Fick's law stated earlier), in which case superdiffusion (faster than normal diffusion) due to active transport or subdiffusion (slower than normal diffusion) due to macromolecular overcrowding can occur. Small soluble molecules such as glutamate have been shown to exhibit subdiffusion result from extracellular protein overcrowding in the synaptic cleft (Saftenu, 2005). The tortuous environment also leads to fractal diffusions. As the name suggests the dimensionality of the extracellular space is not a true three dimensional space. This is clear from any EM

photography of brain tissues, that extracellular space is a highly connected and convoluted collection of 2D planes. Despite all these complexities, it is possible to approximate diffusion in a porous medium in accordance with the classical physical laws if appropriate regimes are used and correct assumptions are taken care of (Nicholson & Phillips, 1979).

Experimental measurements of neurotransmitter diffusion in brain structures have been quantitatively studied with ionophoresis, fluorescent recovery after photobleaching (FRAP) and integrated optical imaging (IOI) as reviewed by Nicholson *et al.*, 2001. They have shown that diffusion of small ions in the extracellular space largely depends on the tissue volume fraction and tortuosity, generally obeying the Fick's law (Nicholson & Phillips, 1981). As detailed below, measures of those two parameters have been obtained using a variety of techniques (Hrabetova, 2005; Nicholson & Sykova, 1998), which we shall review in the next section. The porous medium approximation generally applies on a macroscopic scale (hundreds of micrometres to millimetres) which exceeds characteristic dimensions of individual cellular obstacles, such as diameter of axon and dendrite or even small cell bodies of interneurons. The microscopic diffusion within the synaptic cleft or between the walls of cellular membranes is less well quantified, either theoretically or experimentally (Nielsen *et al.*, 2004; Rusakov & Kullmann, 1998b; Hrabe *et al.*, 2004; Tao & Nicholson, 2004). Most of the theory involves a simplified view of the environment, and simulation results reproduce experimental data only to a certain degree. To the best of my knowledge, there is no reported direct microscopic diffusion measurement in the synaptic cleft or in the extracellular space on the nanometer scales. Measurements inferred from electrophysiological observations coupled with dextran-dependent diffusion retardation yield the microscopic diffusivity in the synaptic cleft at  $\sim 0.33 \mu\text{m}^2\text{ms}^{-1}$  (Nielsen, 2004). The lack of direct measurements is due to the fact that contemporary optical methods have resolution limits which do not permit direct probing at the scale of  $\sim 20\text{nm}$ .

## 1.5. Existing Methods of Diffusivity Measurement in the Brain Extracellular Space

There have been many diffusivity measurements employed by neuroscientists. They fall mainly into two categories: (i) conductance or resistivity based and (ii) fluorescence imaging based. We shall review these two categories and their advantages and shortfalls.

One of the simplest measurements one could take is the tissue resistance (Van Harreveld *et al.*, 1971; Matsuoka & Hossmann, 1982; Korf *et al.*, 1988). This method relies on the changes in extracellular space or ion concentration variability causing impedance changes in the brain tissue, which could be picked up by an electric circuit. This method however only measures relative changes in the extracellular space volume fractions (extracellular space volume/total tissue volume). To measure the absolute tissue volume fraction and its tortuosity in the brain, an iontophoretic method was introduced.

The real-time iontophoretic method (RTI) (Sykova, 2004b; Nicholson & Sykova, 1998) is based on continuously ejecting small amount of membrane-impermeable ions (e.g. tetraethylammonium) into the extracellular space with a small current in the microelectrode. After ions diffuse outwards, the current change at a distant (typically  $>100\mu\text{m}$ ) is then picked up by ion-selective microelectrodes and fitted to a non-linear model (Nicholson & Phillips, 1981) of iontophoresis based on three free parameters: volume fraction, tortuosity and non-specific concentration dependent uptake. Absolute values of these three parameters and their dynamic changes in nervous tissue can now thus be obtained both *in vivo* and *in vitro* (Sykova, 2004b).

One drawback of both methods lies with their invasiveness. As large electrodes and glass pipettes are introduced into the region of interests, the tissue is compressed possibly distorting the extracellular space architecture. One might not expect the tortuosity to change much, but reduction in volume fraction near the intrusion sites would seem a plausible consequence. The resistive method also suffers from non-selectivity. Extracellular changes in ion

concentrations could easily cause fluctuations in the measurements as such changes alter the conductance of the extracellular medium. The ionophoresis although highly selective with use of exogenous particles, it relies on elaborate non-linear theoretical schemes with multiple variable parameters that need to be fitted onto experimental data with complicated growth and decay forms. As once von Neumann said 'with four parameters I can fit an elephant, and with five I can make him wiggle his trunk' (Dyson, 2004), it is difficult to obtain accurate measures of parameters in complicated models with multiple parameters, especially if there are dependencies between the parameters, though the three parameters in the RTI method were argued to be independent of each other (Sykova & Vargova, 2007). But with non-specific concentration dependent uptake being an parameter than can not be firmly contributed to some solid physiological processes or properties, the error of the parameters extracted can be large to say the least.

Another category of methodology are fluorescence optical methods, which are largely invented for chemistry experiments originally. The main advantage when compared to the ionophoresis is that it measures diffusion directly through visual means and can avoid use charged molecules. One of the older methods is fluorescence correlation spectroscopy (FCS). It was developed in 1974 by Magde *et al* for analysis of chemical diffusion and reactions (Magde *et al.*, 1972). It utilises the fact that signal of background fluorescence will fluctuate in a correlated fashion corresponding to the reaction rates and diffusion of the fluorescence markers. An increase in diffusivity could simply be viewed as a decrease in signal autocorrelation. Although the method is simple and established, difficulties come as most of the time we do not know how and what does the fluorescence marker react to in extracellular space and what is the best approximation for the optical illuminated extracellular space on the scale measurements are taken. Hence which model to be used for fitting the data is a highly difficult issue to wrestle with even with very experienced FCS experimentalists. Apart from that, the method is particularly difficult in cells, and has not been tried in slice tissues due to high optical scattering properties of brain slices, and numerous other obstacles such as select right concentration level to use in order to avoid the

exacerbated influence of noise in brain slice environment (Personal communication with Petra Schwille).

Another simple measurement of the ADCs of fluorescent dye or molecules tagged with fluorescent dye is integrative optical imaging (IOI) (Nicholson & Tao, 1993). The principle of the method depends on the assumptions that diffusion obeys simple 3D diffusion equations convoluted onto a kernel that approximate the spatial geometry of the extracellular space. As a fluorescent dye is pressure injected from a glass micropipette into the tissue and its 2D planar distribution is then measured optically using a CCD camera. The profile of the distribution can then be fitted with the model. This method also relies heavily on theoretical models being correct. Particularly approximation of the spatial geometry of the extracellular space introduces considerable errors between model and data. As indicated in the Nicholson and Tao paper, signals in the 2D Gaussian profile that were lower than 25% of the maximum signal (i.e. around the rim of the 2D Gaussian profile) deviate from the model, so these part of the data were excluded from the fitting process. Another obvious drawback is that not only micropipette has to be introduced but also a pressure is being exerted from the pipette tip through injection.

Fluorescence recovery after photobleaching (FRAP) has recently emerged as a method that enable diffusion measurement on a smaller scale compare to IOI (Braeckmans *et al.*, 2007; Sniekers & Van Donkellar, 2005; Trugnan *et al.*, 2004) . The principle relies on the diffusion correlated recovery of fluorescence intensity in the fluorescence void or partial void which was created by intense laser light destroying some fluorescence properties of the dye molecules in that region. Variety of such methods exists, such as ellipsoid spot (Papadopoulos *et al.*, 2005; Mazza *et al.*, 2008) and line FRAP (Sniekers & Van Donkella, 2005). The method is non-invasive, and based on reaction-diffusion properties of the fluorescence dye in the extracellular environment much like the FCS. The main advantage of FRAP over FCS is the signal is much higher than FCS, which makes fitting much less prone to noise. The theory required to fit the FRAP curves require good knowledge of photobleaching

efficiency and photobleaching volume shape, which both dependent on laser power and photo properties of individual fluorophores. Although they are not complicated to quantify in free medium because shape of the fluorescent void created can be accurately modelled, but it is proven to be less straightforward in the tissue medium due to scattering (Lubkin & Wan, 2006). The main problem with slice tissues is that scattering makes laser power and photobleaching volumes inside the slice tissue dependent on depth and cannot be measured accurately, which then makes selecting some model parameters difficult, such as the photobleaching rate with respect to laser power inside the slice, the point spread function (PSF) of the laser spot in turbid medium such as brain tissues (Kirby & Delpy, 1996; Dong *et al.*, 2003). Although two-photon mode is advantageous (Patterson & Piston, 2000) in PSF estimation compare to confocal, because the excitation volume in two-photon mode is highly restricted to a small ellipsoid volume with much smaller deviation in slices compare to single-photon mode. However, despite that advantage the modelling and the significance of photobleaching of non-linear order are not well understood either (Chen *et al.*, 2003), which means photobleaching rate in two-photon mode is different to that in single-photon mode which is still being used in two-photon FRAP. Recent incorporation of standing wave FRAP also provides a promising possibility towards nanometer diffusivity measurement (Davis & Bardeen, 2002). This cleverly uses interference patterns from two laser sources to create a standing wave pattern across the tissue, where the width of the bright fringes can be as small as tens of nanometres. However, in either single-photon or two-photon mode or new standing wave FRAP, intense laser power is required to achieve total or partial photobleaching. This could easily heat up the sample locally, which would overestimate diffusivity if not destroy the tissues locally.

In summary, the existing methods measure diffusion on a spatial scale of millimetres down to micrometres, except FCS and standing wave FRAP. However both latter methodologies are under-developed for mediums with high optical scattering properties such as slices. Within the brain slice environment all existing optical methods also suffer from finding the correct theoretical models with quantified experimental parameters and validated

assumptions. Therefore diffusion on nanoscopic or picoscopic scale in brain extracellular space has not hitherto been examined. In principle, however, it is possible to do so through time-resolved fluorescence spectroscopy and time-resolved fluorescence anisotropy imaging (Small & Isenberg, 1977; Anderson, 1991). These methods also share some problems with previous discussed optical methods due to scattering and absorption in biological tissues. But due to the drastic improvement in photon detections methods in recent years it has been possible to apply such methodologies in samples other than cuvette solutions (Partikian *et al.*, 1998; VanDeVen *et al.*, 2005; Elson *et al.*, 2004), most notably in cell cultures. We have now developed this new approach to establish the diffusivity of small molecules in extracellular space on a picoseconds scale in *ex vivo* brain tissue slices. The principle and application of the method will be discussed in Section 2.5.

### **Summary**

The main aim of this thesis is to first establish glutamate diffusivity at different spatial and temporal scales, from tens of micrometers to nanometres. This should provide many fundamental parameters for the future in constructing accurate biophysical models from single channel to volume transmissions. Using these accurately measured diffusivity values, we will then explore the microscopic effects of glutamate diffusivity and many attributes of glutamate transporters (such as density and position) on intrasynaptic and extrasynaptic transmissions, and the macroscopic effect on the ambient glutamate landscape. In determine the glutamate diffusivity, we first establish in CHAPTER 3 the macroscopic value on the scale of  $\sim 10^{-5}\text{m}$ , using the point source diffusion method of the smallest fluorophore available. In CHAPTER 4, we will utilise the nonlinear relationship in diffusivity changes and synaptic response changes to establish the glutamate diffusivity in the synaptic cleft on the scale of  $\sim 10^{-7}\text{m}$ . Then we will apply a newly developed optical method (Section 2.5) to establish the previously unknown glutamate diffusivity at nanoscopic level in CHAPTER 5. Once we've obtained accurate measurements of glutamate diffusivity at all spatial scales, we put them first

into full 3D Monte-Carlo simulations (CHAPTER 6) to test the influence of glutamate diffusivity and transporters on intrasynaptic and extrasynaptic responses. Secondly, in CHAPTER 7, we put the macroscopic glutamate diffusivity values into 3D compartmental model to examine the effects of glutamate transporters on long range glutamate diffusion and ambient glutamate concentration levels.

## CHAPTER 2. METHODS

### 2.1. Experimental Preparation

All animal procedures followed the Animal (Scientific Procedures) Act, 1986.

Young male Sprague-Dawley rats (3-4weeks old) were sacrificed with an overdose of intraperitoneal injection pentobarbitone (140mg/Kg). We dissected out both hippocampi in ice-cold sucrose solutions containing (in mM): sucrose 70, NaCl 80, KCl 2.5, MgCl<sub>2</sub> 7, CaCl<sub>2</sub> 0.5, NaHCO<sub>3</sub> 25, NaH<sub>2</sub>PO<sub>4</sub> 1.25, and glucose 22 (bubbled with a 95% O<sub>2</sub>-5% CO<sub>2</sub> mixture osmolarity ~300-304mOsm determined by VAPRO 5520 vapour pressure osmometer). Both hippocampi are placed in agar block and transverse hippocampal slices (~300-350µm thick angle 15 degree) were obtained using vibrating blade microtome (VT1000S, Leica Instrument GmbH, Nussloch, Germany). After cut slices were transferred to an interface chamber containing EBSS medium (Invitrogen, Paisley, UK) supplemented with 1 mM CaCl<sub>2</sub> and 2 mM MgCl<sub>2</sub>. Slices were stored in the chamber for at least an hour before they were transferred and hold down by nylon wire mesh in submersion-type imaging/recording chambers superfused with artificial CSF containing (in mM): NaCl 124, KCl 5, NaHCO<sub>3</sub> 26, NaH<sub>2</sub>PO<sub>4</sub> 1.25, D-glucose 10, MgCl<sub>2</sub> 1.3, CaCl<sub>2</sub> 1.5. All solutions are bubbled with a 95% O<sub>2</sub>-5% CO<sub>2</sub> mixture, and with a measured osmolarity of ~300-310mOsm.

### 2.2. Electrophysiology

Field potentials were recorded in slices before and after imaging experiments, to test the slice viability. Extracellular stimuli were delivered by a bipolar stimulating electrode in Schaffer Collaterals for orthodromic stimulation. Recording pipette (~5MΩ, AgCl coated wire) pulled from borosilicate glass capillary tubing was filled with same extracellular perfusion solution and placed between the *stratum pyramidale* and stratum radiatum of CA1.

Extracellular signals measured against a Ag/AgCl ground pallet in the bath medium, were recorded through an Axoclamp amplifier (Axon Instruments, USA). Slices were deemed healthy after a total of 5-6hrs after transportation (See Figure 1), storage and experimentation on the slice by confirmation of pair pulse facilitation of the extracellular field signal in both CA1 and CA3 after stimulation at the Schaffer collaterals. Visual inspections through confocal microscope (Olympus BX-50) were also carried out on slices before and after imaging to ensure tissue is generally healthy.

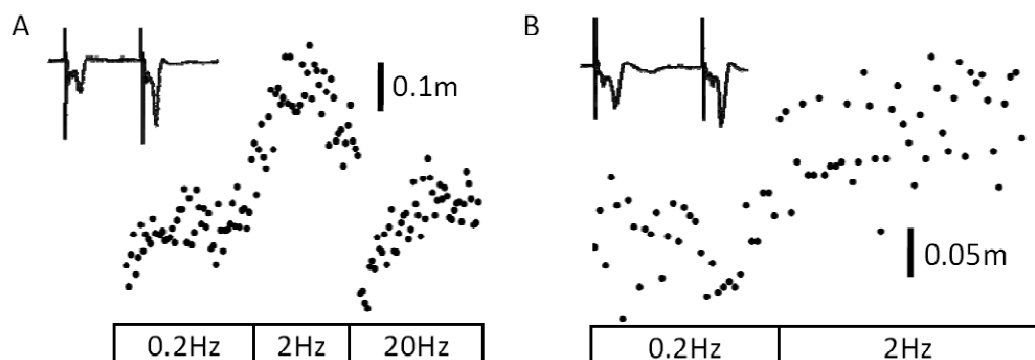


**Figure 1 Extracellular Field Potential in CA1 and CA3 of Hippocampus after Diffusion Measurements Indicate Unchanged Physiological Viability**

A: Pair pulse protocol measured in hippocampal CA1 by stimulating in Schaffer Collateral with various frequencies (as labelled), inset single pair pulse example  
 B: Same protocol measured in CA3

### 2.3. Two-photon Excitation Imaging of a Point Source Diffusion

The two-photon excitation imaging technique was used because it takes advantage of the fact that multi-photon excitation occurs only within a thin ( $\sim 1\mu\text{m}$ ) focal layer of the illuminated tissue volume (Zipfel & Webb, 2001). This layer is normally much wider than typical extracellular gaps ( $\sim 25\text{nm}$ ) while being much thinner than the regions of measurement ( $\sim 50\mu\text{m}$ ), implying that recorded fluorescence is approximately a point source diffusion evolving in space and time, hence provides direct readout of the indicator concentration profile in the focal plane.

Two-photon imaging is performed on a multi-photon microscopy installation comprising a Radiance 2100 imaging system (BioRad-Zeiss) which is mounted on an upright Olympus BX50 microscope (Olympus water

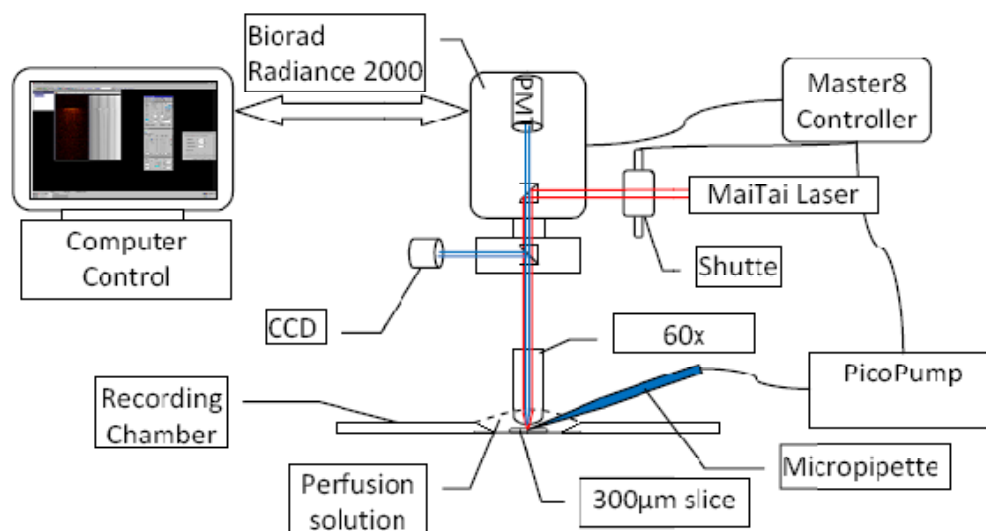


**Figure 2 Two-Photon Scanning Point Source Diffusion Setup Schematic**

immersion objective 60 $\times$ , NA = 0.9; 40 $\times$  objective, NA = 0.5; 10 $\times$  objective, NA = 0.25) and is integrated with a MaiTai (SpectraPhysics) Ti-Sapphire infrared femtosecond pulse laser (Scott & Rusakov, 2006) (Figure 2).

A micropipette pulled from Sutter Instrument P-97 (Figure 3A shows both DIC and fluorescence images confirming 1.0-1.5 $\mu$ m tip diameter) was filled with a fluorescent indicator Alexa Fluor 350 (hydrazide, sodium salt, Molecular Probes, MW 349.29, Figure 10E illustrates the molecular structure, emission maximum at approximately 444 nm, pipette concentration 0.2mM), connected to a pressure line (PicoPump, WPI) and lowered into a submersion type recording chamber perfused with artificial CSF (for composition refer to Section 2.1) where transverse hippocampal slices obtained as described above had been secured with a light weight nylon grid. The pipette was inserted 50 - 70 $\mu$ m deep into transverse hippocampal slices' CA1 *stratum radiatum* neuropil region with no obvious obstruction of cell bodies in front of the pipette tip.

Because the two photon absorption spectra of these indicators are not the same as single photon absorption spectra as usually provided by the manufacturer, the optimum excitation wavelength in two photon mode was

hence established empirically to  $\lambda_x = 790\text{nm}$  by scanning the excitation laser between 700nm and 850nm. The time-average laser power under objective was 0.3–0.4mW; no detectable photobleaching of the indicator (confined to the glass pipette) was seen at this range of power within few seconds of continuous exposure.

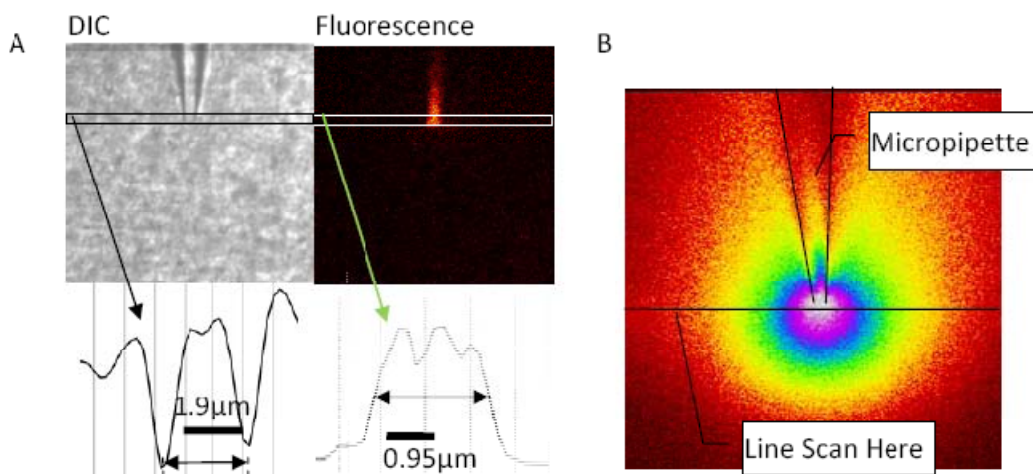


**Figure 3 Micropipette Dimension and 2D Gaussian Profile of Ejected Indicator**

A: DIC (Differential Interference Contrast) and fluorescent image of micropipette, where the bar indicating ROI where signal integrations took place which gives the results as shown below each image

B: 2D central cross-section of the 3D diffusion profile of AF350 during a prolonged pressure ejection showing near perfect Gaussian profile; Line scan position (for all two-photon ejection experiments) is just in front of the micropipette orifice to minimise any deviation from theory and

The system was focused, in a scanning frame mode, on the pipette tip; we then adjusted the holding pressure to eliminate any detectable leakage of the fluorescent indicator. A brief pressure pulse (<20 ms long, ~10 psi) ejects indicators and form a circular Gaussian fluorescence transient, as expected from the point source diffusion (Figure 3B). Because detected fluorescence in these conditions should be proportional to the indicator concentration, we recorded the time course of the spatial fluorescence profile using the line scan mode: a single scanning line (rate 500Hz) was positioned immediately in front of the point of ejection (Figure 3B), and the pressure pulse was triggered 100 ms after the scanning onset; the scanning sweep lasted 1s. In each experimental phase, 10 line scan sweeps, 30s apart, were recorded and stored as a set of 8-bit colour-coded images preserving the original brightness values.

The same procedures were repeated with exactly same conditions except 5% 40kDa Dextran were added to the perfusing ACSF with no significant osmolarity changes. The Dextran molecules were added in order to retard the diffusion of neurotransmitters in the extracellular space, so that effects of Dextran on neurotransmitter diffusion and synaptic responses could be measured simultaneously. This provides means to estimate glutamate diffusivity in the synaptic cleft in hippocampal CA1 (CHAPTER 4).

Diffusion analysis of acquired sets of images was performed using a MATLAB-based (MathWorks) program developed in-house (See Appendix F for pseudo code). The programme assumes uniform 3D diffusion from a point source. The validity of the assumptions of the model has been addressed in (Savtchenko & Rusakov, 2004). A Gaussian profile is expected at the source (i.e. at the tip of the pipettes) according to classical solution for instantaneous point-source diffusion (Equation 1), where  $C(r,t)$  is the space-time a profile,  $Q$  is the total amount of ejected diffusing substance (a scaling

$$C(r,t) = \frac{Q}{8(\pi Dt)^{3/2}} \exp\left(-\frac{r^2}{4Dt}\right)$$

**Equation 1 Point Source Diffusion Equation in Spherical Coordinate**

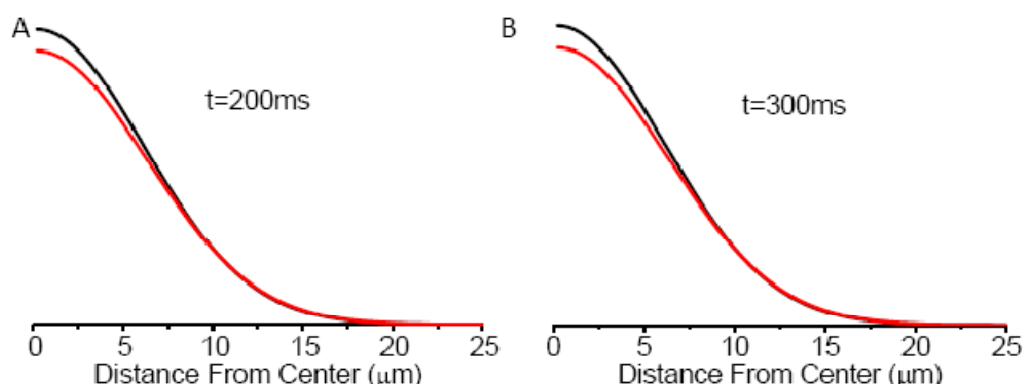


**Figure 4 Gaussian Diffusion Profile of a point-source and a spherical source at t = 100ms, 300ms**

Black Trace: Ideal Point Source; Red Trace: Worst Possible Case of Spherical Source of 6 $\mu$ m in diameter; Axis of Abscissa: Distance in  $\mu$ m; Axis of Ordinate: Amplitude (Arb. Unit)

factor which can be ignored during fitting procedure) and  $D$  is the diffusion coefficient. However, because the ejection pulse was not instantaneous (5-10ms) and the pipette tip has a finite dimension of 1-2 $\mu$ m in diameter, in principle this does not constitute an ideal point source. Direct measurements

of the ejection flux from our standard protocol showed that when we incorporate these values into the solutions for a spherical (as opposed to point) instantaneous diffusion source, the expected concentration profiles on a scale  $>50\text{nm}$  only deviated by 5% FWHM and less than 1-2% by area under the curve from those in the point-source case (Figure 4). This confidently confirmed the validity of our point-source approach to the problem. Another advantage of the instantaneous point-source approach was that individual pulses were too short to leave any detectable increment in the residual fluorescence in the region of interest (due to possible non-specific indicator binding and uptake by cells). Because such fluorescence could in principle accumulate above the background level over multiple ejections, we also routinely subtracted the pre-pulse fluorescence profile from the recorded diffusion profiles.

Experimental data was fitted with the discrete form of Equation 1. The parameter  $Dit_i$  was obtained by standard MATLAB non-linear square fitting of the Gaussian fluorescence profile  $I_i(r,t_i)$  (Figure 5B), which is proportional to the concentration profile  $C_i(r,t_i)$ , at every time point  $t_i$  (i.e. Gaussian profile of each line scan at 2ms intervals were fitted) post-pulse. The classical test for linear diffusion (i.e.  $D_i = D = \text{const}$ ) is that the  $Dit_i$  value should increase linearly with  $t_i$ . We observed that this linearity generally holds at  $>50\text{ms}$  (after the initial slight disturbance resulting from the pressure pulse Figure 5C); generally at  $>300\text{ms}$  post-pulse, the signal-to-noise ratio became too low. We therefore normally sampled all fluorescence profiles between 50-300ms (areas sandwiched between two black lines in Figure 5A) and select reasonably linear regions for robust fitting procedures provided by MATLAB, and therefore an estimate for  $D$  in each recorded scan. The robust fitting procedure provided by MATLAB uses iteratively reweighted least squares with a bi-square weighting function, which is tuned to reduce the weighting of the residue from outliers (Figure 5C). This procedure generally produces good fitting to the original data (Figure 5A) and was repeated on all data sets, giving the average value of  $D$ . Fitting procedures were custom written in MATLAB7.

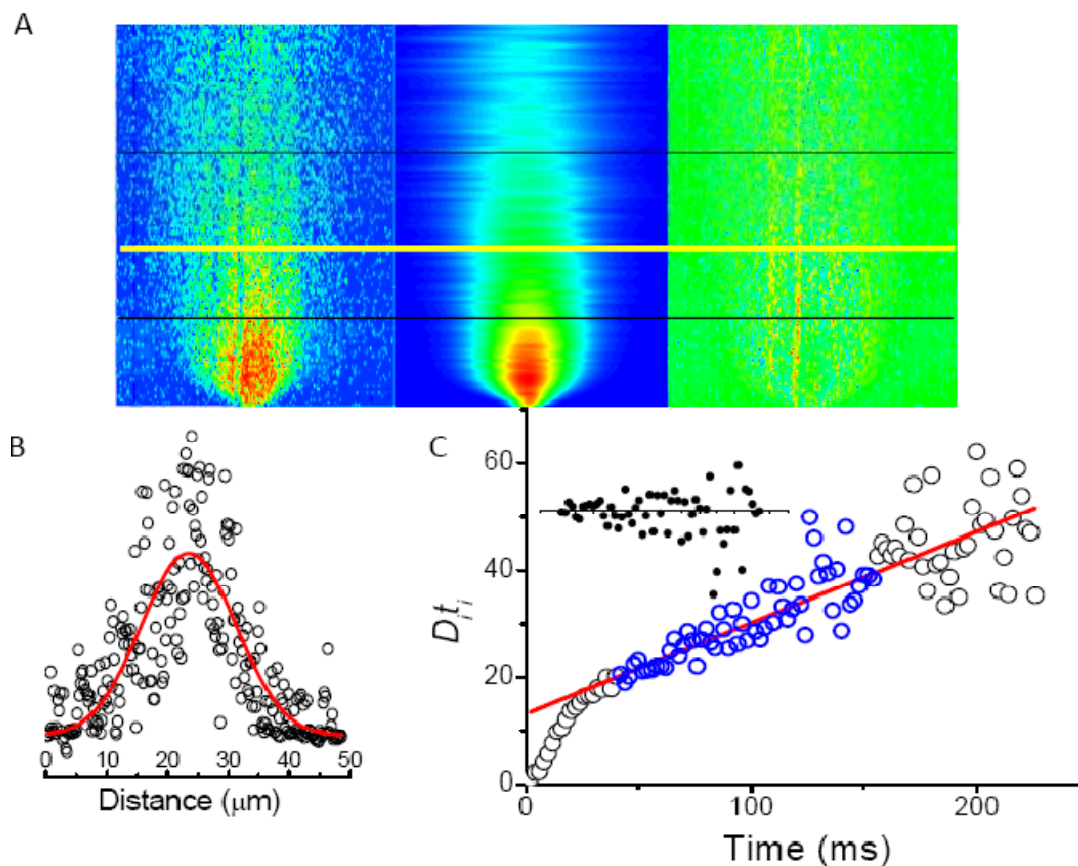


**Figure 5 Point Source: Fitting a theoretical curve to the experimental profile**

A: From left to right, raw image, fitted Image, residue of the fitting respectively; Image width =  $49\mu\text{m}$ , height =  $450\text{ms}$ ; Bottom Black Line at  $t = 42\text{ms}$ , Middle Yellow Line at  $t = 80\text{ms}$ , Top Black Line at  $t = 154\text{ms}$ ; Discrepancy in the residue map shown as bright yellow streaks are cell bodies  
 B: Data at cross-section where the yellow line ( $t = 80\text{ms}$ ) denotes; Black circle is the raw data and the red line is fitted Gaussian profile  
 C:  $Dt_i$  vs  $t_i$  plot showing nonlinear initial segment between  $0\text{-}50\text{ms}$  due to pressure pulse and subsequent linear diffusion; Circular data points are results of the Gaussian fit as illustrated in B; Blue circles are data within linear regions and acceptable S/N ratio as marked between black lines in A; Red line is the robust fit which weights down sporadic points across the blue circles; inset figure is the fitting residue plot of the robust fit

## 2.4. Computational Models and Simulations

### 2.4.1. Three-Dimensional Monte-Carlo Simulation of Synaptic Transmission

In order to simulate on the very small temporal and spatial dimensions of a single synapse and its immediate vicinities (temporal step  $\ll 0.1\text{-}1\mu\text{s}$ , spatial step  $\sim 3\text{-}30\text{nm}$ ), we used Monte Carlo simulations based on the Brownian motion of a particle. Many compartmental models have been employed to illustrate time evolution of a synaptic transmission (Clements,

1996; Otis *et al.*, 1996; Rusakov 2001; Nielsen *et al.*, 2004), since in almost all circumstances theoretical solutions cannot be attained. However compartmental models also suffer from spatial averaging and deterministic diffusion process. When we are dealing with concentrations of nanomolars or less or in nanolitres volumes, the deterministic model do not always portray the reality faithfully. In many cases particles are sparse in the volume and reaction sites are typically small in dimension, hence spatial averaging of concentration for diffusion-reaction models may not be valid. One either has to adopt computationally unreasonable number of compartments or use adaptive compartments. In comparison Monte Carlo method is a better representation of the stochastic system and straightforward to implement. Even though it is computationally intensive, especially in 3D, for small structures and fewer than tens of thousands of reaction particles, it is still reasonably achievable.

At first we used a 2D Monte Carlo model (Appendix A) as a test bed for computational efficiency reasons to test few hypotheses. Results from 2D model show consistencies with other similar 2D models in term of EPSCs profile. However, the number of receptors that were activated seemed always higher than would be expected from mEPSCs if one assumes the AMPARs' conductance state has a conductance of 10nS (Swanson *et al.*, 1997). Reported conductance state/states for AMPARs vary (Derkach *et al.*, 1999; Banke *et al.*, 2000; Jin *et al.*, 2003), which makes higher amplitude from 2D MC model a less critical issue. However, later on, after the completions of 3D MC model, despite some simulation results (such as the effect of transporter density) agree with what 3D model suggests (CHAPTER 6, Figure 27), few experiments show high sensitivity to the model paradigm, in particular the measurement of intracleft diffusivity (CHAPTER 4, Figure 24). The curvature of the nonlinear curve is very sensitive to whether a 2D or a 3D Monte-Carlo method is being used. A full 2D Monte-Carlo simulation would eventually give an estimate for synaptic glutamate diffusivity at  $\sim 0.7\mu\text{m}^2\text{ms}^{-1}$ , which is near the diffusivity in solutions. A two layer compartmental simulation (i.e. dimensionality-wise somewhere between 2D and 3D) of the synaptic cleft as it was done in Nielsen *et al.*, 2004 paper would give an average estimate of  $0.32\mu\text{m}^2\text{ms}^{-1}$ . Therefore, the question of 2D model's validity led us to construct a more realistic and detailed synaptic



assumed to be absorbing to ensure the particles disperse into the surrounding neighbourhoods.

The 3D structure of synapses formed by en-passant boutons of Schaffer Collaterals on dendritic spines of CA1 pyramidal cells in the hippocampus has been documented in detail (Schikorski & Stevens, 1997; Shepherd & Harris, 1998; Ventura & Harris, 1999). Several biophysical Monte Carlo models have been used to simulate a single vesicular release and subsequent responses (Franks *et al.*, 2002; Wu *et al.*, 2007), notably MCell programmes. We aim to test several aspects of different factors that may influence the post-synaptic responses as we have tentatively studied in the 2D model with a much simplified 3D programme than MCell.

AMPAR		NMDAR		EAAT1/EAAT2		EAAT3	
$k_{on1}$	*4.59e6	$k_{on1}$	*10e6	$k_+$	*10e6	$k_+$	*2e7
$k_{off1}$	4260	$k_{off1}$	4.7	$k_-$	200	$k_-$	300
$k_{on2}$	*28.4e6	$k_{on2}$	*5e6	$k_2$	100	$k_2$	500
$k_{off2}$	3260	$k_{off2}$	9.4	$k_3$	40	$k_3$	40
B	4240	B	46.5				
A	900	A	91.6				
$k_{d+1}$	2890						
$k_{d-1}$	39.2						
$k_{d+2}$	172	$k_{d+2}$	8.4				
$k_{d-2}$	0.727	$k_{d-2}$	1.8				
$k_{d+3}$	17.7						
$k_{d-3}$	4						
$k_{d1d2}$	*1.27e6						
$k_{d2d1}$	45.7						
$k_{d2d3}$	16.8						
$k_{d3d2}$	190.4						

**Table 1 AMPAR, NMDAR, EAAT1/2, EAAT3 Reaction Kinetic Scheme Constants**

(Default Unit =  $s^{-1}$ ; \*Unit =  $M^{-1}s^{-1}$ ; AMPAR kinetics (Jonas *et al.*, 1993; NMDAR kinetics (Lester & Jahr, 1998); EAAT1/2 kinetics (Rusakov, 2001); EAAT3 kinetics (Diamond, 2001))

Since 3D Monte Carlo model is a straightforward extension from 2D Monte Carlo model, all the algorithms and parameters are essentially the same apart

from the environment itself is more complicated 3D structure (Figure 7D). To model specific synapses will be extremely time consuming, because many forms will have to be tested to get an average result. Hence it is more sensible to model the 3D synaptic cleft as an image of averages of many synaptic clefts (Rusakov & Kullmann, 1998a). This would tell us a lot more about average behaviours of synaptic transmission than the behaviour of one particular synapse, and at the same time not sacrifice too much of real shape of a 'typical synapse'. The synaptic environment is constructed from a presynaptic part (en-passant boutons) and post-synaptic part (dendritic spine heads), both of which are represented by truncated hemispheres separated by a 300nm wide 20nm high apposition zone including a 200nm wide synaptic cleft (Figure 7D) which is consistent with characteristic 3D structure reported for these synapses (Lehre & Rusakov, 2002; Ventura & Harris, 1999; Shepherd & Harris, 1998; Harris *et al.*, 1992). The synapse was surrounded by a network of 20-30nm wide extracellular gaps, and roughly matches the previously estimated extracellular volume fraction of  $\sim 0.15$  (Hrabetova, 2005; McBain *et al.*, 1990; Perez-Pinon *et al.*, 1995). The extracellular diffusion coefficient for glutamate (excluding spatial tortuosity effect as simulation environment intrinsically included this) was routinely set at  $0.4 \mu\text{m}^2\text{ms}^{-1}$  (unless variable diffusivity is required), between the intra-cleft value of  $\sim 0.23\text{-}0.33 \mu\text{m}^2\text{ms}^{-1}$  estimated from electrophysiological experiments (Nielsen, 2004; in CHAPTER 4) and an average extracellular value of  $\sim 0.56 \mu\text{m}^2\text{ms}^{-1}$  estimated here (CHAPTER 5). In baseline conditions, 80 AMPARs and 20 NMDARs (Takumi *et al.*, 1999; Racca *et al.*, 2000) were scattered randomly within the synaptic active zone. Glutamate glial transporters (EAAT1/2 type) were distributed within two spatial quadrants of the extrasynaptic membranes to match the average extracellular density of  $\sim 0.2\text{mM}$  (Lehre & Danbolt, 1998) and to reflect the uneven pattern of glia surrounding these synapses (Lehre & Rusakov, 2002; Ventura & Harris, 1999). Binding is achieved by checking co-localisation of the released free glutamates and individual sites on the membrane surface which is non-permeable to the glutamate molecules.

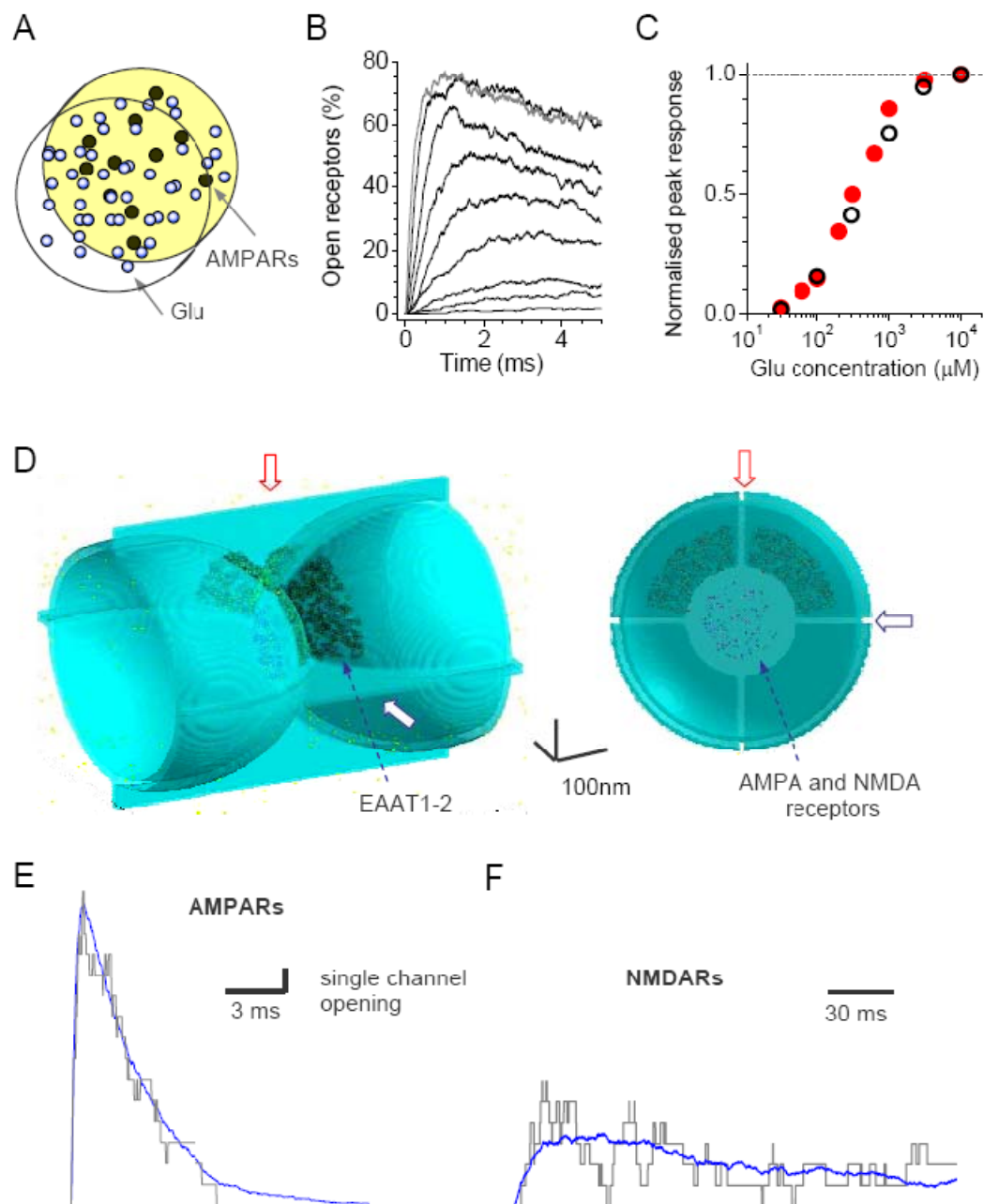


**Figure 7 A Monte-Carlo model of the characteristic Schaffer collateral CA1 pyramidal cell synapse**

A-C: A control simulation test verifying that the model reproduces faithfully the results of an experiment in which glutamate was rapidly applied to outside-out patches of CA1 or CA3 pyramidal cells (Jonas *et al.*, 1993). In a cylindrical volume ( $d \times h = 300 \times 300 \text{ nm}$ ), 20 AMPARs were scattered arbitrarily over one base side, and glutamate molecules were instantaneously injected (uniformly, randomly A) at concentrations of 30, 61, 100, 200, 301, 625, 1000, 3130 and  $10000 \mu\text{M}$ , producing the corresponding current (B; gray trace, response at  $10000 \mu\text{M}$ ). The summary results (C, red circles) match well with the experimental data (hollow circles) of outside-out patch experiments (Jonas *et al.*, 1993)

D: Illustration of 3D geometry of the modelled synaptic environment; left,  $\frac{3}{4}$  view; right, central cross-section projection; arrows indicating some inter-membrane gaps; extrasynaptic membrane regions occupied by transporter molecules are seen (description see text)

E-F: The model outcome showing the opening time course for at baseline conditions (see text for parameters). Gray and blue lines, single run and average of 56 runs respectively.

The model approach to glutamate molecules and proteins interactions are calculated as binding probability for a given catching distance, where only particles within such distance of a protein will be considered for actual reaction probabilities. This is very different to compartmental models' method of local volume concentration equivalence. Other Monte Carlo models in the literature are often vague about detailed binding algorithms, it is therefore much more proper to test our model against real physiological data to see if our approach is a faithful reflection of reality. In this case a simple cylindrical volume is constructed (Figure 7A-C) with 20 AMPARs on the membrane. The volume is initially filled with glutamate molecules for given concentrations. We thus attempted to imitate experiments in outside-out patches excised from CA1 or CA3 pyramidal cells, to which glutamate was applied using a rapid concentration switch (Jonas, 1993). The AMPARs currents generated in our model and the overall dose-response relationship between the glutamate concentration step and the peak AMPAR current were fully consistent with the experimental data (Figure 7B-C).

We further tested computational approaches for the Monte Carlo approach by comparing the outcome of simple simulation scenarios with analytical solutions and multi-compartmental algorithms operating in simpler geometries (Lehre & Rusakov, 2002; Savtchenko & Rusakov, 2007). Indeed, synaptic currents produced by releasing 3000 glutamate molecules in the cleft centre are consistent.

Several schemes were tested in a 3D model as illustrated below in Figure 8. Scheme A shows where the asymmetrically distributed transporter number/density is varied between 0-3000 to see the effect on post-synaptic AMPARs currents in a range of glutamate diffusivities. Scheme B illustrates the insertion of 0-800 intrasynaptic transporters (EAAT4) to test the modulatory significance of such transporters on the AMPARs current. Scheme C draws the setup of a patch of 20 extrasynaptic AMPARs/NMDARs in the presence of EAAT1 or not. Responses from 5ms (for AMPARs-mediated) and 20ms (for NMDARs-mediated) are measured from different distances (0, 145, 250, 340, 420nm) from the centre of release.

Almost all modelling parameters are allowed to be changed in the form of configuration files rather than the code itself. All physiological parameters are set according to the literature as listed in this section.

The simulation programme was written in MATLAB7.0 (Appendix E), but the increase in one extra dimension posing a non-linear increase in the computational powers required. Therefore a Linux cluster was built from 15

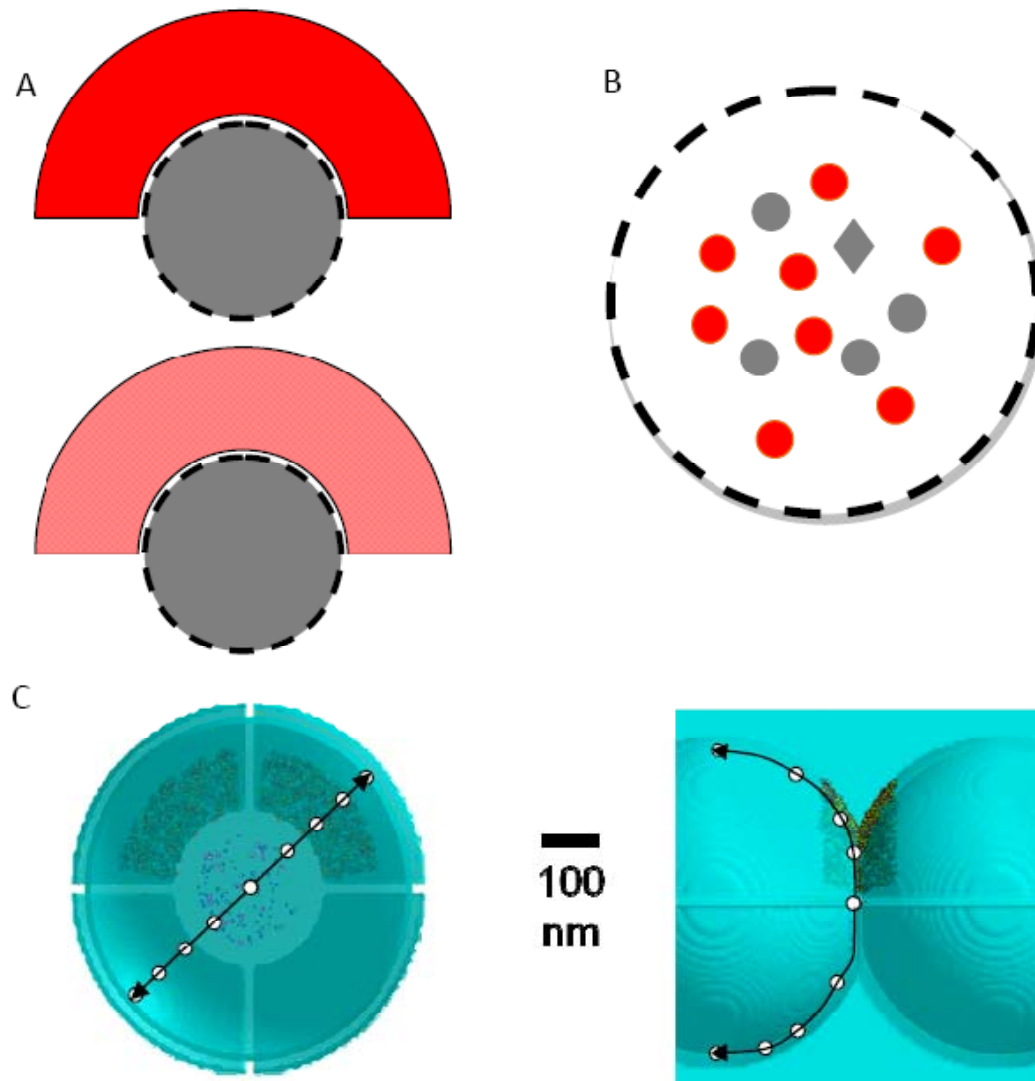


**Figure 8 3D Monte Carlo Simulation Test Schemes**

A: Variable transporter density, where darker red represent 0.2mM and lighter red is 0.1mM; other concentrations are also tested (see text for detailed number), but transporter region shape remains the same; the transporter patch and synaptic cleft is a simplified view of illustration in C  
 B: Test for intrasynaptic transporters, grey circle = AMPARs; grey diamond = NMDARs; red circles = EAAT3s; actual number of proteins are, respectively, 20, 80 and variable (see text)  
 C: Locations of test patch of 20 extrasynaptic receptors (AMPA receptors or NMDARs) as shown in projection by white circles. In the two cases: with (North-East arrow) and without (South-West arrow) the overlapping transporter enriched area.

PentiumIV processor based PCs with hyper threading enabled. Gentoo Linux with kernel version 2.6.15 was installed on the master node and was connected to all 14 slave nodes via a 16-port D-Link Gigabit LAN switch, from which the diskless slave nodes could boot remotely from the master node hard disk into the same Linux environment. All necessary programmes are installed for simulation purposes. The scheduler which allows automatic distribution and book keeping of hundreds required simulation trials, is written in BASH script language (Appendix B).

#### 2.4.2. Three-Dimensional Compartmental Model for Macroscopic Diffusion

One of our goals was to evaluate the dynamics of extracellular glutamate on the scale of synaptic populations. Therefore, we sought to model a relatively large region of the hippocampal area CA1 neuropil. Although a straightforward expansion of the Monte Carlo methodology is in principle possible (Hrabetova *et al.*, 2003; Hrabe *et al.*, 2004), the addition to the system of multiple reactions with large number of unevenly distributed receptors and transporters appears to require unrealistic computational resources. We therefore used concentration profile from our Monte Carlo model of an individual synapse and its environment as an elementary building block for the concentration evolution in a compartmental model of the synaptic neuropil, as explained below.

A simple forward difference Euler's method ( $y_{n+1}=y_n+h \cdot f(x_n,y_n)$ ) in both temporal and spatial grids was used as the quickest implementation to achieve our goal. A three-dimensional  $40 \times 40 \times 40\mu\text{m}$  compartmentalised neuropil environment is constructed as a three-dimensional porous medium (Nicholson & Rice, 1987 & 1986), with the porosity  $\alpha = 0.15$  (Hrabetova, 2005; McBain *et al.*, 1990; Perez-Pinzon *et al.*, 1995) and the apparent (macroscopic) glutamate diffusion coefficient  $D$  set in accordance with the *in situ* measurements (CHAPTER 3). Synaptic release sites for glutamate were scattered randomly, in accordance with the volume density of synapses in area CA1,  $N_V = 2.0 \mu\text{m}^{-3}$  (Rusakov & Kullmann, 1998a). Individual sites were able to release equivalent of 3000 molecules of glutamate at any arbitrarily chosen time point as an

increase in compartments' glutamate concentration. The space was divided into 0.25  $\mu\text{m}$ -wide cubic compartments; due to the need for the spatial resolution to be sufficient to discern individual synapses (the expected nearest-neighbour distance between synapses in this area is  $\sim 0.5 \mu\text{m}$  (Rusakov & Kullmann, 1998a).

The cubic 3D environment contains two pools of releasing synapses, 5 and 10  $\mu\text{m}$  diameters respectively, distanced at 15  $\mu\text{m}$  from centre to centre (Figure 9B). The numerical method used the equations below,

$$F_j^n = -D \frac{\partial c}{\partial r} = -D (c_{j+1}^n - c_j^n); \quad \frac{\partial c}{\partial t} \cong \frac{c_j^{n+1} - c_j^n}{\Delta t} = -\frac{\partial F}{\partial r} \cong -(F_{j+1}^n - F_j^n)$$

**Equation 2 Compartmental Model Simple Forward Step Scheme**

where  $F$  is the flux in and out of each individual compartment;  $c$  is the concentration at that compartment. Numerical stability is ensured by using small spatial and temporal step sizes according to the diffusion coefficient and reaction probabilities ( $p < 0.1$  for the fastest reaction probabilities to ensure Poisson approximation is still valid for independent stochastic processes). Spatial and temporal averaging individual space compartments might in principle distort the time course of extracellular glutamate in the proximity of release sites. To eliminate this source of uncertainty, we first used the Monte Carlo model (Figure 9A inset) to calculate the average glutamate concentration time course within virtual 0.25  $\mu\text{m}$ -wide cubes that make up the simulated environment. Next, we compared the resulting glutamate profiles with those generated by the macroscopic compartmental model in which release events were represented by a volume-average glutamate concentration jump in the synapse-containing 0.25  $\mu\text{m}$  compartment. We found that the concentration time course predicted by the two models produced a reasonable match (Figure 9A). This ensured that the macroscopic compartmental model was based on a plausible representation of microscopic events occurring in the immediate synaptic vicinity.

The model allows parameters to be set and change during simulations. Some basic parameters modelling parameters were set relating to physiological measurements. Release frequencies is set as 20Hz inside the

pools and 0.05Hz everywhere else to provide some form of glutamate leakage (Bouvier *et al.*, 1992), glutamate transporter density 0.2mM (Lehre & Danbolt, 1998), transporter kinetics used are as described before in MC models (Wadiche *et al.*, 1995; Diamond & Jahr, 1997), transporter density, diffusivity and release frequencies will be varied to test various scenarios. Simulation is run till equilibrium is reached in the whole volume by mean of measuring rate of concentration increase has reached zero, or as a fall back in some situations the simulated time had reached 10 seconds and the second derivative of concentration in the whole environment had reached zero.

The programme was written in MATLAB7.0 (Mathwork) as listed in Appendix D together with a standard configuration file for the basic environmental variables. The simulations are run on a Pentium IV processor based PC.

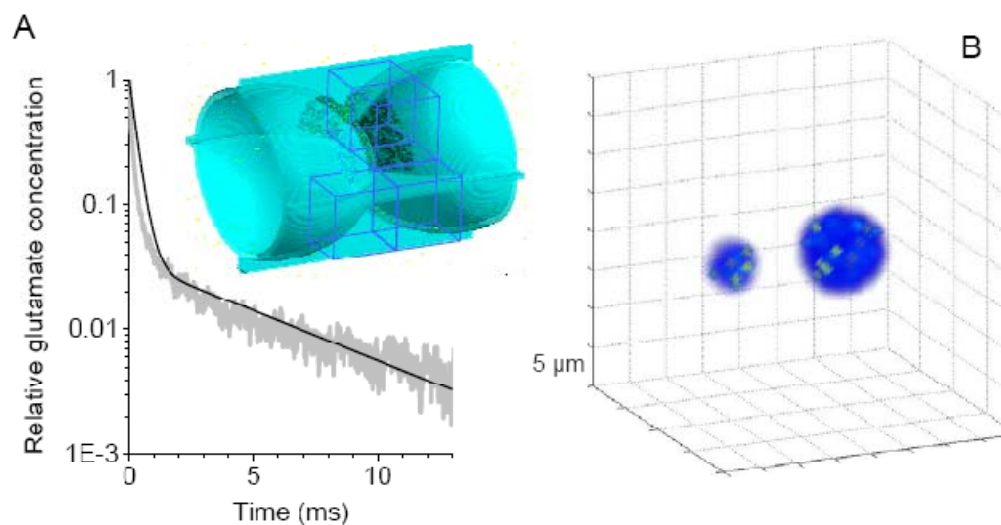


**Figure 9 Diffusion Equivalence between Monte Carlo and Compartmental Model**

A: Matching the concentration profile of MC model of the synaptic environment (Figure 7D) and the macroscopic compartmental model of the neuropil. Inset: in the MC model (geometry shown), the glutamate concentration was averaged over the  $0.25\mu\text{m}$  cubic volumes (indicated); the concentration time course was compared with that calculated using similar (equi-concentration) compartments of the macroscopic model. Release number (3000) and EAAT1 density (0.2mM) were matched. Plot: gray and black lines, glutamate concentration time course in the central synaptic volume calculated using, the MC and the compartmental model respectively

B: 3D impression of the two active synaptic pools in the neuropil. Colours indicate local glutamate concentrations. (See text for parameter details)

## 2.5. Time-Resolved Fluorescent Anisotropy Imaging Microscopy (TRFAIM)

### 2.5.1. Theoretical Background

#### *Fluorescent lifetime and fluorescent anisotropy*

All fluorescence processes have a lifetime ( $\tau$ ) which is defined to be  $1/(\Gamma+k_{nr})$ , where  $\Gamma$  is the emissive rate of the fluorophore and  $k_{nr}$  is the rate of non-radiative decay to the ground state (Figure 10A). However since fluorescence emission is a random process,  $\tau$  would be the average time constant of the decay curve of fluorescence lifetime (Figure 10B). Generally for most fluorophores  $\tau$  is between 1 and 10ns, during which time interaction with the surrounding environment could significantly alter the value of  $\tau$  and hence lifetime of a fluorophore can be very illustrative of the immediate environment where it resides.

Fluorescent anisotropy is based on the principle of preferential photo excitation by polarised light to the same polarisation angle. Depending on the fluorescent lifetime and rotational freedom of the fluorophore, emitted light would be of different polarisation (Figure 10E). This can be simply measured by using parallel and perpendicularly positioned analyser to the excitation plane. The rate of convergence of the parallel and perpendicular intensity is indicated by the time dependent anisotropy decay (Figure 10C-D). The faster the decay the higher is the rotational diffusivity. The time dependent fluorescent anisotropy is defined in Equation 3, where  $r(t)$  is the time

$$r(t) = \frac{I_{//} - B - G(I_{\perp}(t) - B)}{I_{//} - B + 2G(I_{\perp}(t) - B)}$$

**Equation 3** Time Dependent fluorescent anisotropy calculated from experimental measures

dependent anisotropy;  $I_{//}$  is the fluorescent intensity of the parallel analyser;  $I_{\perp}$  is the fluorescent intensity of the perpendicular analyser;  $B$  is the background signal which could be made negligible by increase signal-to-noise ratio;  $G$  is the G-factor reflecting an inherent polarisation error in the detection system (This will be explained later on in this section).

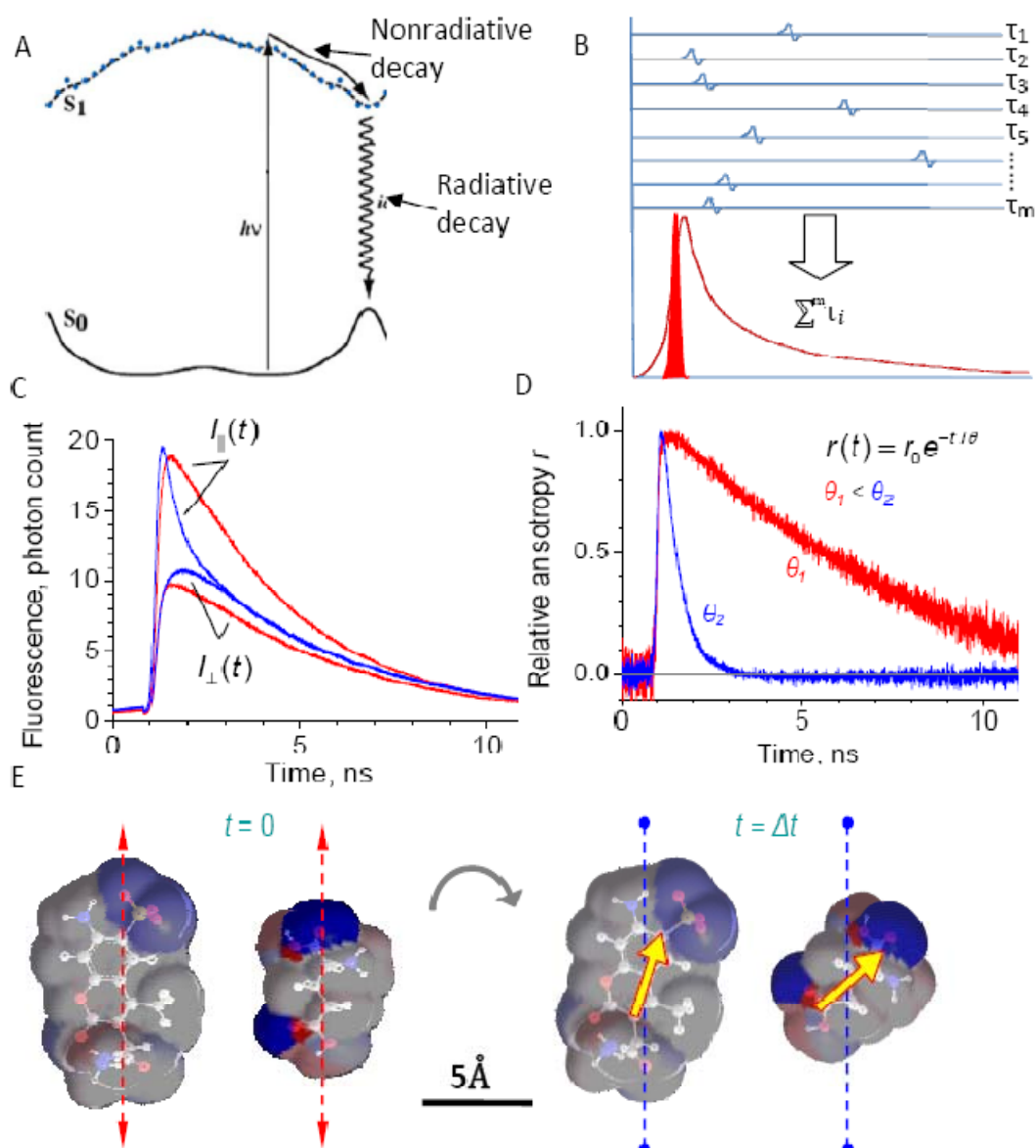


**Figure 10 Illustration of TRFAIM Principle**

A: Fluorescence process illustration of a single photon excitation being absorbed by the molecule, which goes from  $S_0$  singlet ground state to  $S_1$  singlet excited state. Subsequent nonradiative decay and radiative decay brings it back down to  $S_0$  ground state from  $S_1$  state.

B: Experimental exponential decay of lifetime signal as the sum of individual random decays. Red spike shows the timing of the laser excitation pulse

C-D: Test experiments showing clear dissection of the AF350 fluorescence time course in  $\parallel$  &  $\perp$  analyser to the excitation plane, in two free solutions containing 40% (blue, lower viscosity) or 100% (red, higher viscosity) glycerol at room temperature.

E: Molecules (left: AF350, right: glutamate) excited with polarised light at  $t=0$  (left: red arrows, polarisation plane) can move and rotate before emitting at  $t=\Delta t$  (right), because emission polarisation rotates with the structure (yellow arrow). The signal collected by analysers  $\parallel$  &  $\perp$  to the excitation plane will decay at different rate depending on the rotation speed. Scale bar =  $5\text{\AA}$  (Molecule reconstruction calculated from their chemical formula in Chem3D Ultra)

The Fluorescent Lifetime Imaging Microscopy (FLIM) based method has many advantages over other existing fluorescence imaging methods (See 1.5 for pitfalls in current fluorescent imaging methods). Because we are measuring the intrinsic property of a molecule, this generally means that fluorescent lifetime is independent of variations in fluorophore concentrations, illumination intensity, and photobleaching (Lakowicz, 2006). This gives a clear advantage over normal ratiometric imaging method where these factors have to be carefully considered. The non-invasiveness also gives it advantage over ionophoresis method, and in some cases cells exhibits intrinsic fluorescence so no exogenous marker have to be introduced.

### ***Linear Relationship between fluorescence anisotropy and diffusivity***

Rotational diffusion of fluorophores is a dominant cause of fluorescence depolarisation, if the lifetime of the fluorophore is at least an order of magnitude longer than the rotational relaxation time so that during the depolarisation caused by the rotational diffusion there is no contribution from the fluorescent lifetime decay. For a simple spherical rotor molecule only exhibits single exponential decay in fluorescent anisotropy, the decay constant can be directly linked to local viscosity (Figure 11A; Lakowicz, 2006). For small spherical molecules, simple assumptions could be made and the usual Stoke-Einstein, Debye and Perrin equations (Figure 11B) could be applied as the theoretical assumption of these models are based on simple solid spherical particles. With some elementary derivations, one would arrive at the conclusion that lateral diffusivity ( $D_T$ ) is proportional to  $\theta^{-1}$  (Figure 11B). The constant of proportionality is directly related to the square of the hydrodynamic radius of the molecule. Therefore, by measuring fluorescent anisotropy decays using TRFAIM, one can deduce the rotational and hence translational diffusivity of the molecules in that environment.

### ***Basic assumptions***

The pros of TRFAIM and FLIM over traditional fluorescent based method, is the independence over fluorophore concentration, photobleaching, illumination intensity variation. However, TRFAIM and FLIM is easy to

measure, the interpretation of the data requires considerable knowledge of fluorophore properties. Especially when decay signals are not a simple mono-exponential decay, one has to devise theoretical models to understand the data. Our assumption for the model is that the fluorophore we use will be a small spherical molecule obeys basic laws of translational and rotational diffusion.

How plausible then, is the assumption of a small spherical molecule for fluorescence molecule we used in this study, namely Alexa Fluro<sup>®</sup> 350 (AF350; M.W. 326, dimensions:  $10\text{\AA} \times 5\text{\AA} \times 5\text{\AA}$ ; other specification refer to Invitrogen datasheet) (Figure 10E)? Rather than going into complicated and detailed models of many modified theories on rotational diffusion of oblate elliptical molecules (Wegener *et al.*, 1979), many of which could not be experimentally validated, we tested out the simple theory experimentally. By putting AF350 fluorophore into different mix of glycerol and ACSF solution and different mix of dextran and ACSF solution, and then measure  $D_T$  using two-photon excitation method outlined in 2.3 and  $\theta^{-1}$  using TRFAIM, it is evident (Figure 11C) that a linear relationship is present. The measured gradient  $\sim 0.126 \pm 0.01\text{nm}^2$  (in both glycerol and dextran experiments as  $r_a$  should be independent of solution composition) suggests that  $r_a$  for AF350 is  $\sim 0.75\text{nm}$ , which is of the right order of magnitude (about the same as the major axis of the molecule if one calculate all the bond length and angles) considering that the hydration radius (Figure 10E) would be the apparent radius when the fluorophore is in a solution. Therefore we are confident that the simple spherical molecule model is sufficient for our purposes.

Another important assumption that was mentioned earlier is that the time dependent decay has to exhibit a simple exponential decay profile. Theoretically, even for a simple spherical molecule there are at least five decay components, though in theory one could never extract all the components experimentally (Lakowicz, 2006). In practice major components can be distinguished as long as they differs by at least one order of magnitude, and we could assume this is close enough to a single exponential decay during the time window of one of them. The  $r(t)$  of AF350 in various glycerol/ACSF mixture

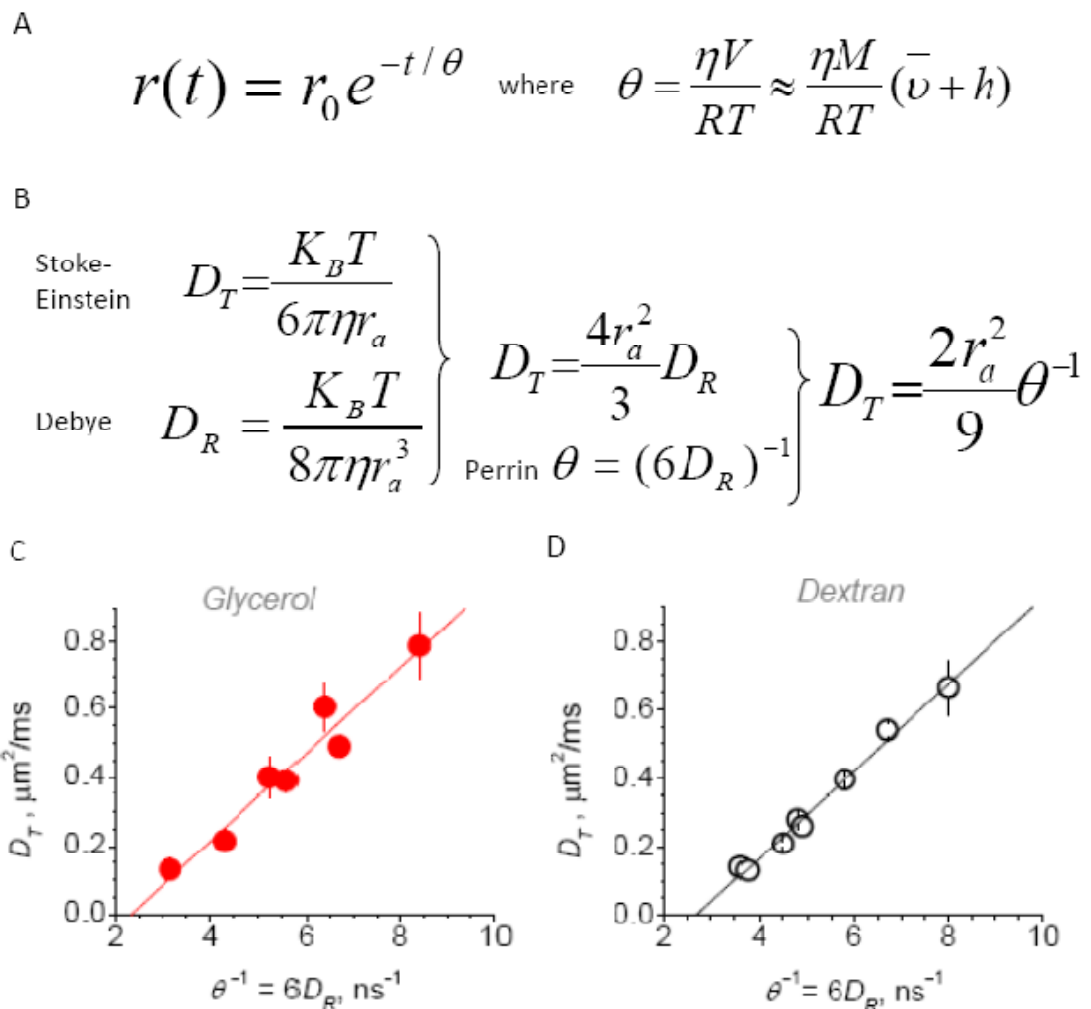


**Figure 11 Illustration of Linearity between rotational and translational diffusivity**

A: Theoretical formulation gives the fluorescent anisotropy decay  $r(t)$  has a decay constant  $\theta$  which is directly related to viscosity  $\eta$ . (note similarity with Einstein's relation)  $\theta$ =Rotational Correlation Time;  $\eta$  = Viscosity;  $V$  = Molecular Volume;  $M$  = Molecular Weight;  $\bar{v}$  = Specific Volume ( $\approx 0.73\text{ml/g}$ );  $h$  = hydration ( $\approx 0.23\text{g H}_2\text{O/g protein}$ )

B: Simple derivation shows linearity between  $D_T$  and  $D_R$  (hence  $\theta$  as well) for small spherical molecule which obeys both Stoke-Einstein and Debye relations;  $r_a$ = hydrodynamic radius;  $D_R$  = rotational diffusivity;  $D_T$ = translational diffusivity;  $\theta$  = Rotational Correlation Time;

C-D: AF350 translational diffusion coefficient  $D_T$  measured with the point-source method (ordinate) is proportional to the rotational diffusivity correlated rotational correlation time measured with TR-FAIM (abscissa) in both glycerol and dextran solutions. This linearity gives an estimated  $r_a$  for AF350 to be approx. 0.75nm (compare with Figure 10E)

shows a clear single decay behaviour as the natural log plot Figure 12A demonstrates. However, in the dextran/ACSF mixture, the same holds true only for low concentration solutions (Figure 12B). At high concentration ( $\geq 20\%$ ), a slower second component is clearly visible (Figure 12B). This could possibly due to dextran macromolecular aggregate to form crosslinks as dextran solutions over 20% by weight are highly viscous solutions (In fact, it

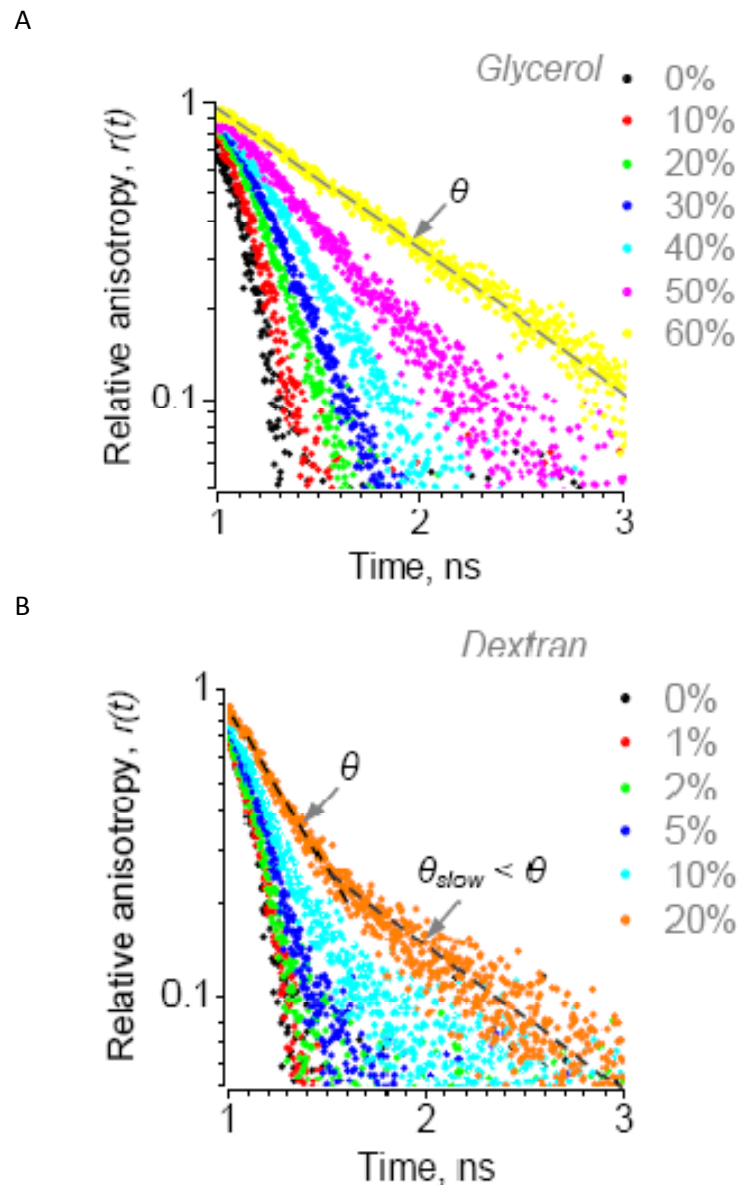


**Figure 12 Single Components of Time-dependant anisotropy decay**

A: Fluorescence anisotropy time course  $r(t)$  for AF350 in solutions of glycerol in ACSF shows a clear single-exponent decay corresponding to a rotational correlation time  $\theta$ ; dots, individual data points; percentage values, glycerol concentrations. Here and thereafter,  $r(t)$  data are normalised with respect to the maximum over the duty cycle for clarity (a theoretical maximum of  $r(t)$  for strictly parallel absorption and emission is 0.57 (Lakowicz, 2006))

B: The AF350  $r(t)$  in solutions of 30kDa dextran in ACSF shows two distinct exponential decay components at higher dextran concentrations (>5%),  $\theta$  and  $\theta_{slow}$ . Other notations are as in A.

took considerable effort to mix such solutions completely). This second slow decay component is most likely a result of such interaction between the fluorescence molecules and high density macromolecules. This feature also presents itself in all the  $r(t)$  results in brain slice tissues (Figure 13). We believe this is due to the interaction of AF350 with lipid membranes and other macromolecules present in the ECS as the same slower component becomes

much more prominent in fixed tissue slices (Figure 13) and it is the only component when the fluorophore is stuck on the nylon wire. Fortunately the rotational correlation time of such immobilised fluorophore is at least one or two orders of magnitude slower than the fast components, hence in order to work out the diffusivity of unbound AF350, all curves are fitted with double exponential decay model, after which we will only concentrate on the fast decay component.

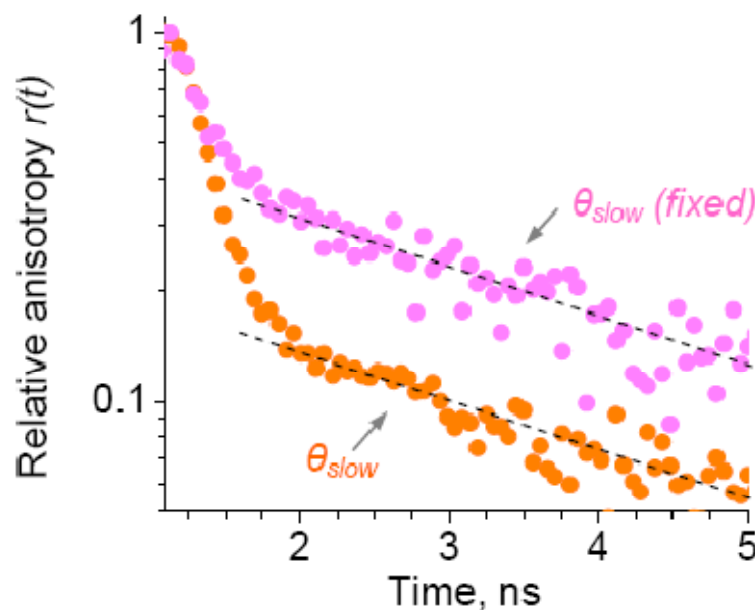


**Figure 13 Rotational Correlation Time in Fixed-tissue samples**

Tissue fixation increases dramatically the fraction of extracellular AF350 molecules showing a 'super-slow' component  $\theta_{slow}$  of the fluorescence rotational correlation time

Birefringence is exhibited from materials that are optically anisotropic, so that two different indices of refraction exist in such material for different polarisations. Birefringent property of neuronal membranes is well documented (Cohen *et al.*, 1968). Methods exist to utilise such properties for action potential measurements (Cohen *et al.*, 1970). Because we are measuring the polarisation plane of the emitted light, properties such as birefringence could introduce bias into our interpretation of the data. A simple cross-polariser imaging method shows extensive birefringence within the slice structure. (Figure 14) Despite this, it is fortunate that we are measuring the time dependent manner of the fluorescent signal, which means the rate of convergence of parallel and perpendicular polarisation (i.e. the decay rate of

$r(t)$  should not alter. Only the initial anisotropy state,  $r_0$ , is affected by this property.

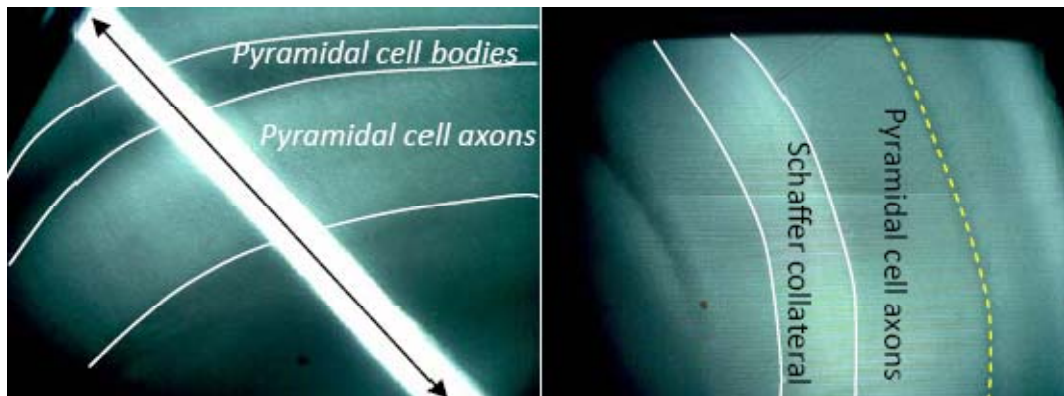


**Figure 14 Hippocampal CA1 Under Cross-polariser Imaging Show Birefringence**

Left: Nylon wire (black arrow) holds the slice underneath shows extreme contrast compare to slices itself which also show contrast with respect to morphological structures. Pyramidal cell axon directions are clearly visible under 40× magnification, the pyramidal cell body also show preferential transmissions

Right: Hippocampal slice shows moderate amount of birefringence contrast and corresponds well to morphological structures; Axons in Schaffer collateral show clear directional preferences, as well as cell body layers (yellow dash line). (20× magnification)

G-factor which appeared in Equation 3, accounts for the different efficiency of transmission and detection between the parallel and perpendicular polarisation pathways. This is instrument specific and can be calculated from solution medium. The G-factor is calculated as the mean of  $I_{\parallel}/I_{\perp}$  from the tail of the trace (i.e. as  $t \rightarrow \infty$  or 12ns in our experimental case). Ideally this should converge to unity in the free medium as the anisotropy half-life is an order of magnitude lower than 12ns (laser repetition interval). This is not always the case, as the setup is adjusted on daily bases according to usage, so all G-factor values are calculated from the free medium region of the image in every set. The average values obtained from all free medium regions amount to  $G = 1.166 \pm 0.001$ .

Photobleaching of the fluorophore should not be a problem for fluorescent lifetime based imaging, as photobleached fluorophore will not have a lifetime. However with time-dependent anisotropy imaging this is not true if, as it is done here, with sequential acquisition. This is simply because the two populations of parallel and perpendicular signals are not monitored simultaneously. Hence photobleaching along the sequential acquisition time

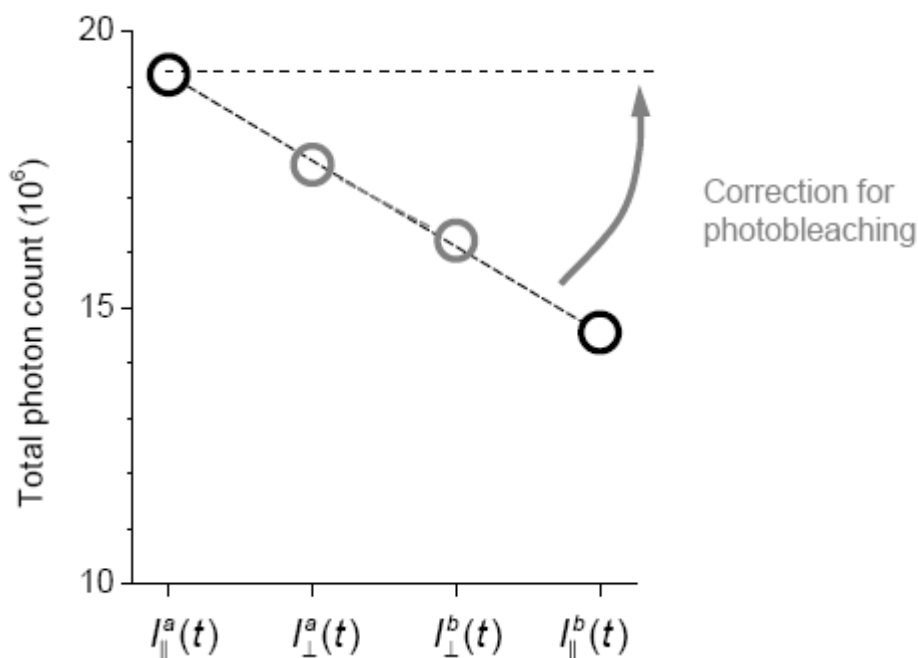


**Figure 15** Photobleaching is roughly linear for sequential acquisition and can be corrected for

Loss of fluorescence due to photobleaching depends on the laser exposure time and can be corrected using a symmetric sequence of acquisitions. Grey circles' ( $I_{\perp}$ ) gradient and Black circles' gradient ( $I_{\parallel}$ ) are approximately the same, suggest the photobleaching process is linear during those time intervals. Grey circles are shifted up for comparison, as total photon count in  $I_{\perp}$  is lower as one expected.

would mean the initial population of every subsequent subset would be lower than it really should be (Figure 15). To counter-act this undesirable effect, the best solution would be implementing a simultaneous acquisition setup, which would give equal photobleaching effect on both parallel and perpendicular detections. However, one can still correct for this with one assumption that the photobleaching effect is linear on the time scale of our data acquisition. To provide simple controls for such correction, we decided to measure  $I_{\parallel}$  and  $I_{\perp}$  in a symmetrical fashion (See Section 2.5.3). This gives that photobleaching at each interval as cube root of the photobleaching over the entire acquisition interval. By assuming linearity (Figure 15) this can be estimate as  $PB_3 = (I_{\parallel}^a - I_{\parallel}^b) / I_{\parallel}^a$ . Then by averaging,  $I_{\parallel}^{ave} = (I_{\parallel}^a + I_{\parallel}^b) / 2$  and  $I_{\perp}^{ave} = (I_{\perp}^a + I_{\perp}^b) / 2$ , one can work out that photobleaching factor between the two means should be  $Z = ((1 - PB_3)^{1/3} + (1 - PB_3)^{2/3}) / (2 - PB_3)$  (See Appendix B for derivations). This can then be applied together with G-factor correction to  $I_{\perp}^{ave}$  as  $I_{\perp}^{corrected} = I_{\perp}^{orig} * G / Z$  before any other curve fittings and calculations. After these corrections, one would expect only noise at the tail (i.e.  $r(t \rightarrow \infty)$ ), when in live slices there are

negligible contribution from the slow components this is indeed the case as illustrated in Figure 16.

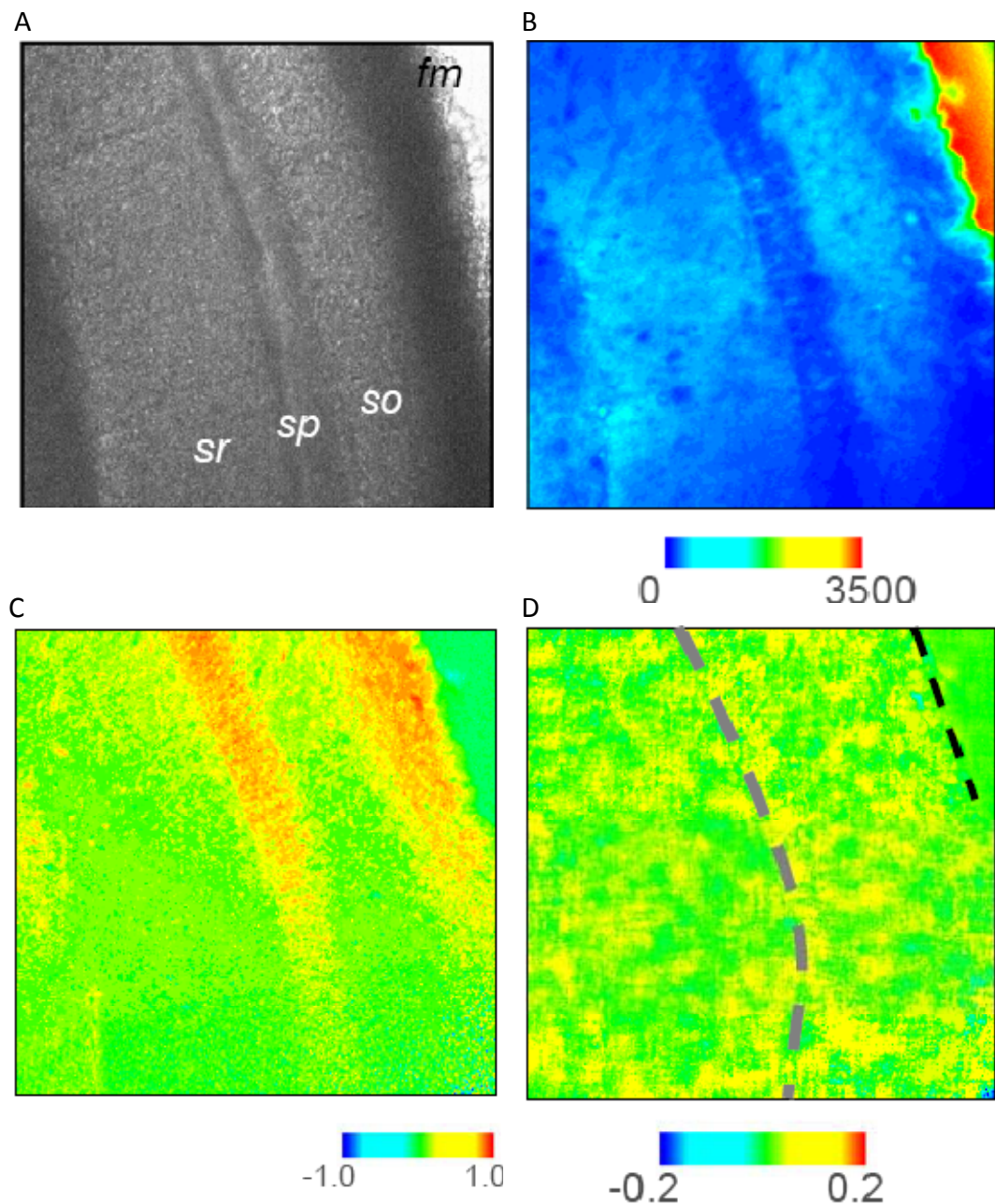


**Figure 16 Correction for Photobleaching and G-factor**

A: A characteristic phase-contrast image of the CA1 area in an acute hippocampal slice (submersion recording chamber); the main hippocampal layers are indicated (20× mag.)

B: Total extracellular fluorescence of AF350 from the hippocampal fragment shown in A; false colour scale bar, photon count

C: The correction factor map of G/Z; G-factor (polarisation error) and Z-factor (photobleaching error) as described in text

D: The rotational anisotropy  $r(t)$  of extracellular AF350 fluorescence measured over the period of expected random polarisation,  $r(t \rightarrow 12\text{ns})$ , after correction using G/Z factor (see C) showing only Gaussian noise inside slice as expected, though higher than that in the free medium

### 2.5.2. Technical Setup

We used the output of a green pump laser (6W Coherent Verdi @ 532nm) coupled to a Ti:Sapphire Mira laser to generate  $\sim 220$ fs (maximum FWHM) pulsed laser light with a repetition rate of 80MHz. Output wavelength is adjusted to 790nm manually by modify resonator length, in order to maximise AF350 excitation. The optical imaging system is based on a Leica TCS SP2 inverted confocal microscope (Figure 17). Several objectives were used without digital zoom, 10 $\times$  (NA = 0.3), 20 $\times$  (NA = 0.5), 40 $\times$  (NA = 0.75), 65 $\times$  (water immersion NA = 1.2) with maximum pin hole opening ( $\sim 400\mu\text{m}$ ). The internal polariser was used as the parallel and perpendicular analyser of anisotropic signal acquisition (Figure 17).

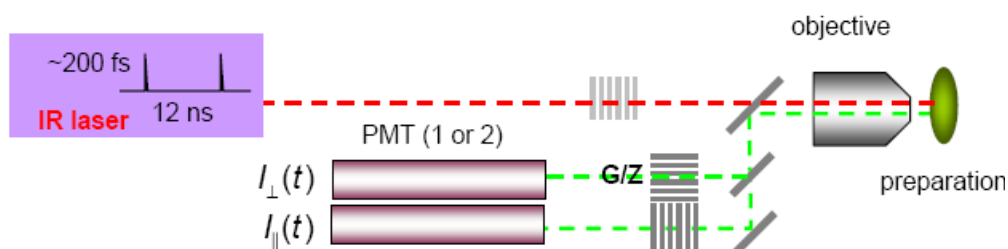


**Figure 17 TRFAIM Optical Setup Schematic**

The experimental TR-FAIM system, normally a single-PMT arrangement was used; grey grid depict light polarisation; see text for detail

Fluorescence signal was acquired at a laser scanning rate of 400Hz and stored as a  $256 \times 256 \times 256$  (x, y, t) tensor representing a stack of 8-bit x-y images using Becker & Hickl imaging modules (TCSPC SPC830). A 700nm short pass filter was placed in front of the detector to block out any escaped light from the laser source.

A Custom-made slice transportation chamber (Figure 18) was used where oxygen was filled and container well sealed before departure. The container is then immediately connected to local oxygen sources once it had arrived at the destination. This is done to minimise damage to the tissue slices. The health of the slice is verified after experimentation, when the sample had to be carried back in the same container. The field potentials showed pair-pulse facilitations in both CA1 and CA3 regions (Figure 1). This is used as

indication of slice viability.

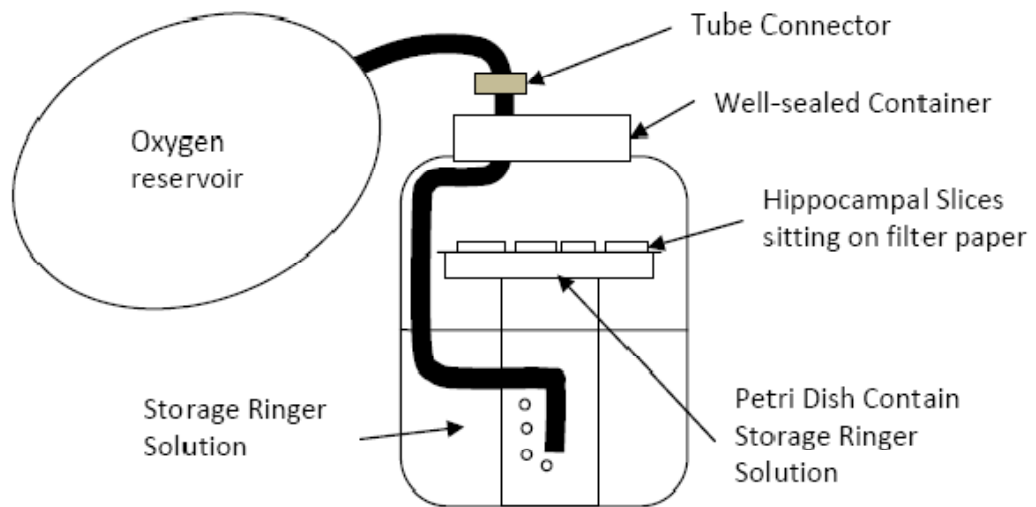


**Figure 18 Slice Transportation Chamber Schematic**

A well sealed container with a gas line connector which could connect to an oxygen reservoir (balloon) or oxygen cylinder was prefilled before transportation.

### 2.5.3. Protocol

Slices were obtained as described in Chapter 2.1, transferred to the modified interface chamber (Figure 18) for 30min to recover and the modified interface chamber was transported to the destination and upon arrival the chamber was immediately reconnected to a oxygen source.

Lasers were tuned to the correct wavelength with  $>1W$  power leaving the laser cavity. A mirror was placed under the objective to obtain the finite impulse function (FIR, instrumental response) so it could later be reconvoluted during fitting procedures.

The G-factor was measured in the ACSF, and set as the instrumental G-factor to be corrected later in analysis (See 2.5.4). After which a slice was placed in a modified perfusion chamber, where solution was oxygenated locally. The slice was held down by a nylon wired mesh, and through the phase contrast microscope the focal plane was moved to the region of interests and focused between 50-100 $\mu m$  deep inside the slice.

Fluorescence lifetime was measured in sequence of four polariser (Polariser selector in Figure 17) positions parallel  $I_{\parallel}^a$  ( $0^\circ$ ) -> perpendicular  $I_{\perp}^a$  ( $90^\circ$ ) -> perpendicular  $I_{\perp}^b$  ( $90^\circ$ ) -> parallel  $I_{\parallel}^b$  ( $0^\circ$ ) with respect to the laser source polarisation.

Average acquisition times were between 30-300s depending on the depth probed, and maximum photon count rate was kept well below 10000counts/s to avoid non-linearity effect in the detection system.

Acquired files were saved in either ASCII or binary format from the SPC software and analysis was later taken with custom-built MATLAB analysis software. For analysis procedure (See 2.5.4) and the code is listed in the Appendix G.

#### 2.5.4. Analysis Method

All data were analysed using custom-built MATLAB programme either as automated batch processing or interactive analysis with GUI. Both contain procedures as outlined in Figure 19.

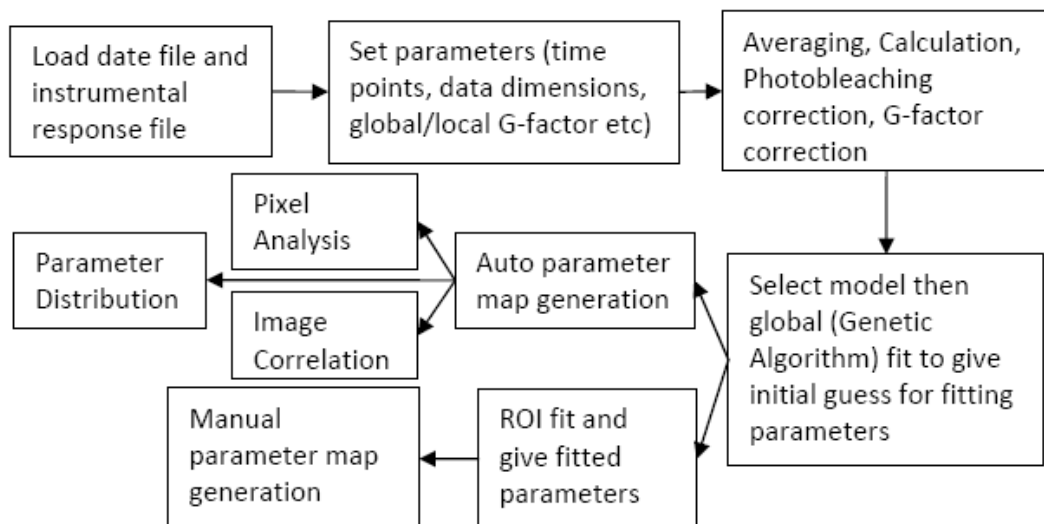


**Figure 19 TRFAIM Analysis Procedure**

Flow chart for TR-FAIM analysis procedure written in MATLAB® 7

Data files and instrumental response file in either ASCII or binary format are read as instructed in Becker & Hickl handbook. Parameters such as size of the image, data point along the time axis and G-factor sections have to be specified manually before any processing and calculation of the data.

Image averages  $I_{\parallel}^{ave}$  and  $I_{\perp}^{ave}$  are calculated and the photobleaching correction factor and G-factor are calculated from  $I_{\parallel}$  and  $I_{\perp}$  data. In order to obtain good signal to noise ratio for curve fitting at individual pixels, nearest neighbour averages have to be obtained. By trial and error, it was established that a nearest neighbour of 15 is sufficiently large in most cases to obtain a good fitting for almost all pixels in the parameter map for fast rotational correlation time ( $\theta_{fast}$ ). This averaging process does not however affect the ROI analysis, in which case average is fitting on the mean of all the pixel data within that ROI.

Exponential decay models of various decay parameters were implemented, in most cases, we found that a single exponential lifetime decay ( $\tau$ ) and a double exponential anisotropy decay ( $\theta_{fast}$  and  $\theta_{slow}$ ) is sufficient to extract all desired parameters. Global fit of the entire image is usually used at the start to obtain good estimates for both lifetime and anisotropy decay constants, so that they could be used as indicators for all subsequent fittings. Global fitting are done with a genetic algorithm (Deb *et al.*, 2002) with 500-1000 generations followed by standard MATLAB simplex function minimisation procedure. The instrumental response is re-convolved into the fitted data during the minimisation procedure, because de-convolution is much harder to do since the Fourier transform of a division is not the same as the division of the Fourier transforms (as operations apply to Equation 3).

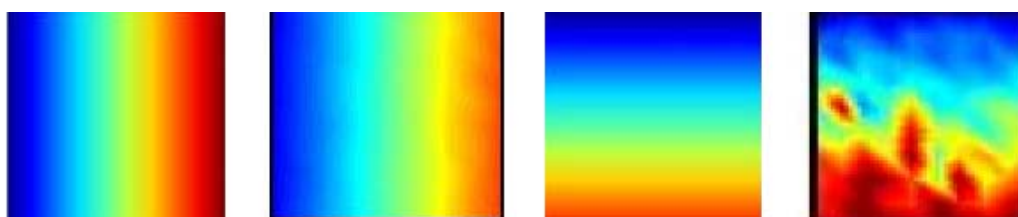


**Figure 20 Analysis programme recovers predefined image template**

Auto analysis programme recovers fluorescent lifetime map,  $\tau$  (left two maps, ideal and retrieved, respectively, gradient goes from left to right valued 2.5-7) and fast anisotropy map,  $\theta_{fast}$  (right two maps, ideal and retrieved respectively, gradient runs from top to bottom valued 0.1-1) from a pre-defined image template with varying lifetime and fast anisotropy decay values and added white noise. (Details see text)

Automated parameter mapping are done by looping through every pixel and fit the desired model as described above. Except few spots with low signal to noise ratio, the procedure generally gives very good fittings (See CHAPTER

5). To further test the automated procedure is capable of reproducing accurate results, a simulated image was presented to the programme and parameters are extracted (Figure 20). The image consists of graduated  $\theta_{\text{fast}}$  (fast anisotropy decay from 0.1 to 1, interval 0.1) and  $\tau$  (fluorescent lifetime decay from 2.5 to 7, interval 0.5) in x and y axis respectively with added white noise of 5% (this is worse than most experimental data, as during the initial decay period, which is critical to the accuracy of the fitting, the noise is much lower and the tail section has much less influence on the fast component of the decay) to each parallel and perpendicular channel. Appropriate G-factor and other fixed parameters are set according to experience from the real data sets. As shown in Figure 20, the error in recovery of  $\tau$  is almost none, the error in  $\theta_{\text{fast}}$  is though higher, but in most cases are around or less than 10%. This error is drastically reduced when the added white noise is reduced, at the limit of no noise, the extraction of  $\theta_{\text{fast}}$  is perfect except where the  $\theta_{\text{fast}}$  and  $\tau$  values are close (e.g. 1 and 2.5).

Knowing that most of the parameter extraction errors are contributed by the noise, one can check the fitting curve residue for each individual pixel, or distribution of parameter within selected ROIs. The distribution of well fitted parameters within a small ROI of the same medium should correspond to a similar parameter value (e.g. the free medium in Figure 25B) and have a narrow Gaussian distribution. Selected ROI with different medium would have much wider Gaussian distribution of parameter values or distributions of multiple peaks or shoulders. Furthermore, image correlation can be done by selecting ranges within the parameter space and the pixels with corresponding parameter values would show up on the image map to show that which regions have similar diffusive properties. The correlation method also helps us to ignore bad fit (e.g. unreasonably fast/slow decay times) by selecting parameter space range to be considered and gives a rough guide to the regions of similarities.

After extensive analysis on image data as described above, most likely similar regions are selected together as ROIs, then either simplex or genetic algorithm or both fitting algorithms would be applied to those regions (without

the previous nearest neighbour averaging procedure). Then the extracted parameters would be used as the value for the whole region, from which a new refined parameter map could be obtained to show in a clearer fashion the heterogeneity in the sample.

## CHAPTER 3. RESULTS: MEASUREMENT OF EXTRACELLULAR DIFFUSIVITY IN THE HIPPOCAMPAL NEUROPIIL – A MACROSCOPIC VIEW

Because monitoring intrinsic glutamate diffusion is not currently possible, we imaged point-source diffusion of a small membrane-impermeable indicator Alexa Fluor 350 (Figure 10E) excited in two-photon mode (See 2.3) in both free medium and in hippocampal CA1 *stratum radiatum* at 21°C and 35-37°C. The dye molecule AF350 (MW 349) is only twice heavier than glutamate molecule (MW 175; Figure 10E), which corresponds to a ~25% difference in their spherical hydration radius. Both species are more than an order of magnitude smaller than any inter-cellular gaps. Furthermore, diffusion of both Alexa Fluor 350 and a much heavier indicator Alexa Fluor 594 (MW 759) is retarded to the same relative degree by dextran solutions that mimic the extracellular medium viscosity (Savtchenko & Rusakov, 2004). Taken those two facts together, these observations indicate that diffusion retardation of Alexa Fluor 350 in the neuropil, relative to its diffusion in a free medium, should be representative of that for glutamate.

### ***Diffusion of AF350 in neuropil (here, absolute D values are related to AF350)***

Experiments (as illustrated in Figure 21A-F) yielded the AF350 diffusion coefficients in the extracellular space ( $D_e$ ) and in a free medium ( $D_f$ ) at 21°C ( $D^{21^\circ\text{C}}$ ) and 35-37°C ( $D^{37^\circ\text{C}}$ ), respectively,  $D_e^{21^\circ\text{C}} = 0.156 \pm 0.006 \mu\text{m}^2\text{ms}^{-1}$  (n = 45 independent trials) and  $D_f^{21^\circ\text{C}} = 0.59 \pm 0.024 \mu\text{m}^2\text{ms}^{-1}$  (n = 20);  $D_e^{37^\circ\text{C}} = 0.23 \pm 0.01 \mu\text{m}^2\text{ms}^{-1}$  (n = 37) and  $D_f^{37^\circ\text{C}} = 0.48 \pm 0.03 \mu\text{m}^2\text{ms}^{-1}$  (n = 22). The average free-to-neuropil diffusion retardation factor, calculated as the mean of the paired  $D_f/D_e$  ratios in individual slice experiments where both  $D_f$  and  $D_e$  were successively measured, was  $R_a^{21^\circ\text{C}} = 3.78 \pm 0.21$  (n = 17 paired trials) and  $R_a^{37^\circ\text{C}} = 2.67 \pm 0.34$  (n = 19; Figure 21G). This corresponds to a tortuosity of  $\lambda_a^{21^\circ\text{C}} = 1.94 \pm 0.05$  and  $\lambda_a^{37^\circ\text{C}} = 1.59 \pm 0.09$ , again, calculated as the average of paired  $\sqrt{(D_f/D_e)}$  values in individual slices. The value at 37°C, but not at 21°C is

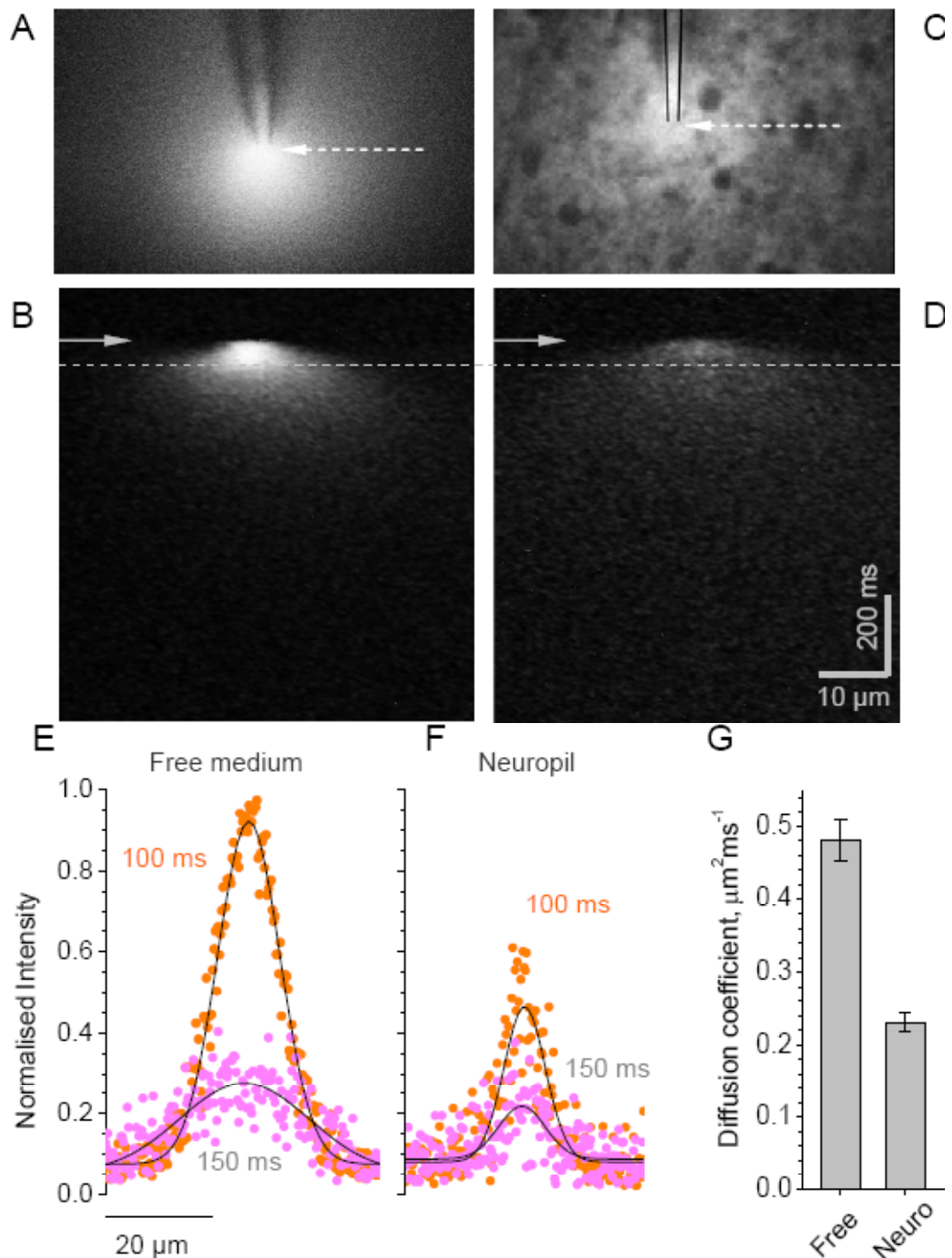


**Figure 21 Measurement of extracellular diffusivity in the CA1 s.r. using point source diffusion**

A-B: Two-photon excitation of AF350 ejected from a micropipette (Figure 3A) in a free bath medium. A, A frame scan of fluorescence averaged over 5s during continuous pressure application; arrow, line scan position. B, A line scan image (single trial, line position shown by dotted arrow in A) depicting evolution of the fluorescence profile following a 10ms pressure pulse (arrow); dotted line indicates a brightness sampling line 100ms post-pulse (see below)

C-D: Experiments similar to those in (A-B), but in s.r. of hippocampal slice. Dark profiles represent intracellular lumen of large dendrites and cell fragments. Notations are the same as in (A-B).

E-F: Fluorescence line-scan profiles sampled at 100ms and 150ms post-pulse in a free bath medium and inside the slice neuropil, as indicated. Orange and magenta dots, experimental profiles; black lines, the corresponding theoretical fit obtained using the instantaneous point source diffusion equation (Equation 1).

G: The average diffusion coefficients for AF350 in a free medium and in the s.r. neuropil, Values see text. Bars, average; error bars, SEM.

in similar range as that in the ionophoresis experiments (Sykova & Vargova, 2007), where  $\lambda_a$  is determined to be around 1.5-1.6 in healthy cortex and hippocampus. This diffusion retardation  $R_a$  incorporates the geometric hindrance factor  $R_t$  (due to extracellular space tortuosity) and the extracellular medium viscosity factor  $R_v$ , so that  $R_a=R_tR_v$  and  $\lambda_a=\lambda_t\lambda_v$  (Rusakov & Kullmann, 1998b). The  $\lambda_a$  values are found to vary depending on physiological conditions (Piet *et al.*, 2004; Homola *et al.*, 2006; Sykova, 2004a). Also considering that 21°C is 15-16°C below physiological temperatures, an increase in medium viscosity ( $\lambda_v$  and  $R_v$ ) hence  $R_a$  and  $\lambda_a$  is expected as it is dependent on temperature. The ionophoresis method cannot distinguish between the two, but we will try to decipher the contribution of those two components later on in CHAPTER 5 with theoretical estimates using Maxwell approximation (Hrabe *et al.*, 2004) and new experimental data from TRFAIM method (Section 2.5).

In accordance with the theory,  $R_a$  has only two contributing factors  $R_t$ ,  $R_v$ , which factor exerts greater influence on the molecule movements? Macroscopic geometrical tortuosity ( $R_t$ ) arises due to the fact that the 3D space is convoluted with twist and turns that are shaped by the opposing cell membranes. The characteristic space between those cell membranes is >20nm, much greater than the diameters of either the indicator we used or glutamate (<1nm). It is therefore evident that the macroscopic geometrical tortuosity factor influences AF350 and glutamate equally. The apparent viscosity factor ( $R_v$ ) has many possible contributors. Extracellular scaffolding matrices, large macromolecules in extracellular medium, membrane viscosity can contribute to the extracellular medium viscosity to different degrees, all of which manifest themselves through particles collisions. Indeed, when we consider microscopic geometric hindrance imposed by large macromolecules (>1nm) as a contributor to the apparent viscosity factor, apart from small size differences, glutamate has a slightly stronger dipole charge (Figure 10E, colour scale represent charge distribution), which would increase any charge related interactions such as electrodiffusion and binding to proteins. However the strength of this disparity between AF350 and glutamate is not obvious. Because of these considerations and for the reasons outlined in the previous paragraph with respects to AF350 and AF594 (Savtchenko & Rusakov, 2004),

we suggest that the retardation factor  $R_a$  for measured AF350 is representative of that for glutamate.

***Estimate macroscopic glutamate diffusivity (here, absolute  $D$  values are related to glutamate)***

The diffusion coefficient of glutamate (based on the only glutamine measurements that have been done) at 25°C in water is  $0.76 \mu\text{m}^2\text{ms}^{-1}$  (Longworth, 1953). The viscosity of a standard physiological solution measured at 22-24°C using a falling ball viscometer is 1.05 mPa·s (Rusakov & Kullmann, 1998b) whereas standard water viscosity in these conditions is ~10% lower, 0.93-0.95 mPa·s (Berstad *et al.*, 1988). Applying this relative change between aqueous solution and physiological solutions to Longworth's measurements, this indicates that the glutamate diffusion coefficient at 22-24°C in the bath medium is  $D_f^{21^\circ\text{C}} \approx 0.68 \mu\text{m}^2\text{ms}^{-1}$ . However, NMR-based measurements of water self-diffusion show a ~26% increase between 25°C and 35°C (Holz *et al.*, 2000). This predicts the glutamate diffusivity value at near-physiological temperature of  $D_f^{37^\circ\text{C}} = 0.68 \times 1.26 = 0.86 \mu\text{m}^2\text{ms}^{-1}$ . Our measurements imply therefore that the average macroscopic extracellular diffusivity of glutamate in the *stratum radiatum* neuropil at near-physiological temperature is  $D_{\text{macro}}^{37^\circ\text{C}} = D_f^{37^\circ\text{C}} / R_a^{37^\circ\text{C}} = 0.32 \mu\text{m}^2\text{ms}^{-1}$ . Similarly at 21°C, the retardation  $R_a^{21^\circ\text{C}}$  is 4.22, this gives glutamate diffusivity  $D_{\text{macro}}^{21^\circ\text{C}} = D_f^{21^\circ\text{C}} / R_a^{21^\circ\text{C}} = 0.18 \mu\text{m}^2\text{ms}^{-1}$ .

These estimates are related to the diffusion of glutamate on a macroscopic scale. We use them in the macroscopic 3D compartmental model as the space-average values of extracellular glutamate diffusivity in CHAPTER 7.

## CHAPTER 4. RESULTS: DIFFUSION

### COEFFICIENT OF GLUTAMATE IN THE SYNAPTIC CLEFT ESTIMATED USING DEXTRAN RETARDATION – A MICROSCOPIC VIEW

Glutamate diffusion inside the synaptic cleft cannot be determined directly. However, it was shown that the relationship between neurotransmitter diffusivity change and ensuing change in AMPARs mediated synaptic current is nonlinear (Nielsen *et al.*, 2004). Therefore a controlled change in the extracellular diffusivity and measure subsequent change in synaptic current at synapses could point to a unique value of the intra-cleft diffusivity (Nielsen *et al.*, 2004) by fitting measured gradient onto a unique point of the nonlinear curve. We set out to apply a similar approach to synapses in area CA1 using biologically inert dextran as a tool of extracellular diffusion retardation suggested in this laboratory (Min *et al.*, 1998; Savtchenko & Rusakov, 2004). We estimated therefore microscopic diffusion inside the cleft by utilising the nonlinear relationship obtained using our 3D Monte-Carlo model introduced in Section 2.4.2 for the changes in postsynaptic AMPAR-mediated responses and those in glutamate diffusivity. Then fit the experimentally measured relative diffusion changes with the introduction of dextran into the synapse and the relative changes in AMPARs mediated synaptic current changes onto a unique point on the nonlinear curve.

#### ***Diffusion retardation of glutamate by dextran in the extracellular space***

Modulation of diffusivity inside the synaptic cleft is required for the non-linear effect on synaptic responses to be used for diffusivity estimate. In order to achieve this, we use 40kDa dextran molecules (5% w/w solution, negligible effect on osmolarity), as described in Section 2.3 (Savtchenko & Rusakov, 2004). First, to establish how much dextran retards extracellular diffusivity, we used two-photon excitation scanning of AF350 diffusion profile

inside slices performed before and after perfusion of 5% 40kDa dextran in ACSF mixture (both at 21°C and at near-physiological temperature 35-37°C).

A decrease in AF350 diffusivity inside the slice due to dextran should reflect a similar degree of retardation to that of glutamate. The argument is similar to the one presented in CHAPTER 3. The retardation factor  $R^{21^\circ\text{C}} = (D_{\text{ACSF}} - D_{\text{Dextran}})/D_{\text{ACSF}} = (0.156-0.119)/0.156 = 24\%$  and similarly  $R^{37^\circ\text{C}} = (0.23-0.17)/0.23 = 26\%$  (Figure 22 shows the respective D values), which gives the relative change in diffusivity  $\Delta D/D$  at  $25 \pm 1\%$ .

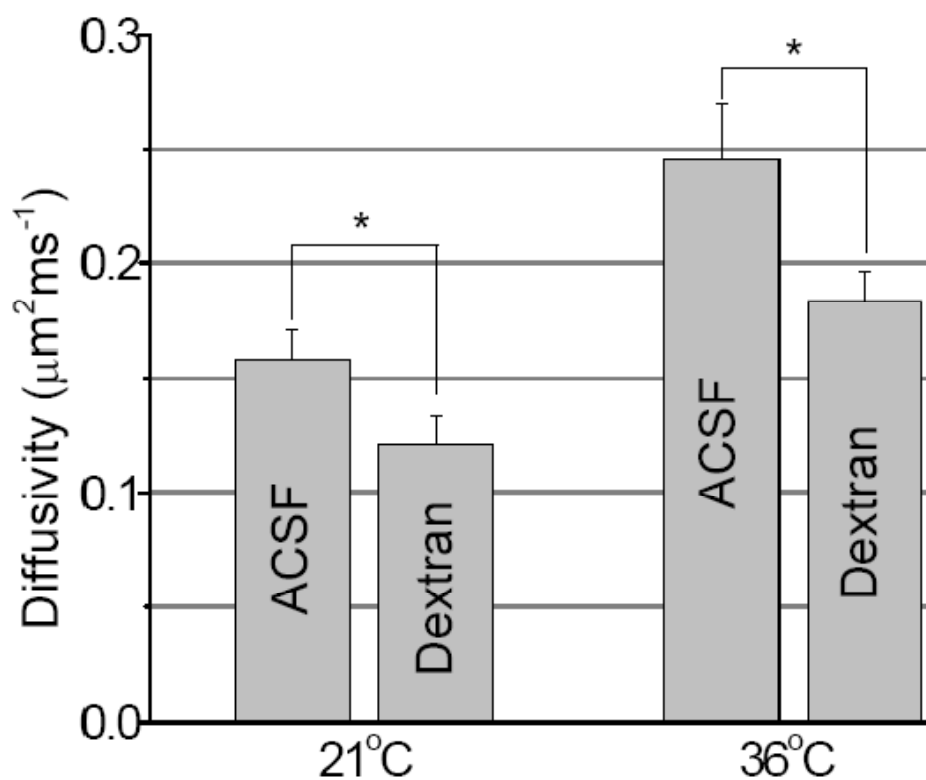


**Figure 22 Diffusion Retardation of extracellular AF350 by Dextran in hippocampal neuropil**

Statistical summary of effect of dextran perfusion on diffusion coefficient (ordinate) of AF350 inside CA1 s.r. neuropil at 21°C (n = 49, n = 32 respectively) and 36°C (n = 35, n = 35 respectively); \*,  $p(D_{\text{ACSF}} > D_{\text{Dextran}}) < 0.02$  (Actual values,  $p = 0.019$ ,  $p = 0.014$  at 21°C and 36°C respectively)

### ***Increase of synaptic AMPARs response due to Dextran in extracellular space***

As reported earlier, EPSCs in CA1 pyramidal cells (whole-cell mode) and field EPSPs both increase by  $16 \pm 8\%$  following perfusion of 5% 40kDa dextran

(Min *et al.*, 1998). However, the accurate value of this change may be sensitive to voltage-clamp errors, which increase with greater synaptic currents. We therefore carried out similar experiments in which a minimal stimulation protocol was used to record single-release responses. We found that dextran increased EPSCs in such experiments by  $21\pm 10\%$  (Figure 23; these electrophysiological experiments were carried out in collaboration with Annalisa Scimemi). This value, including its error margin, was therefore used in our estimates of intra-cleft diffusivity.

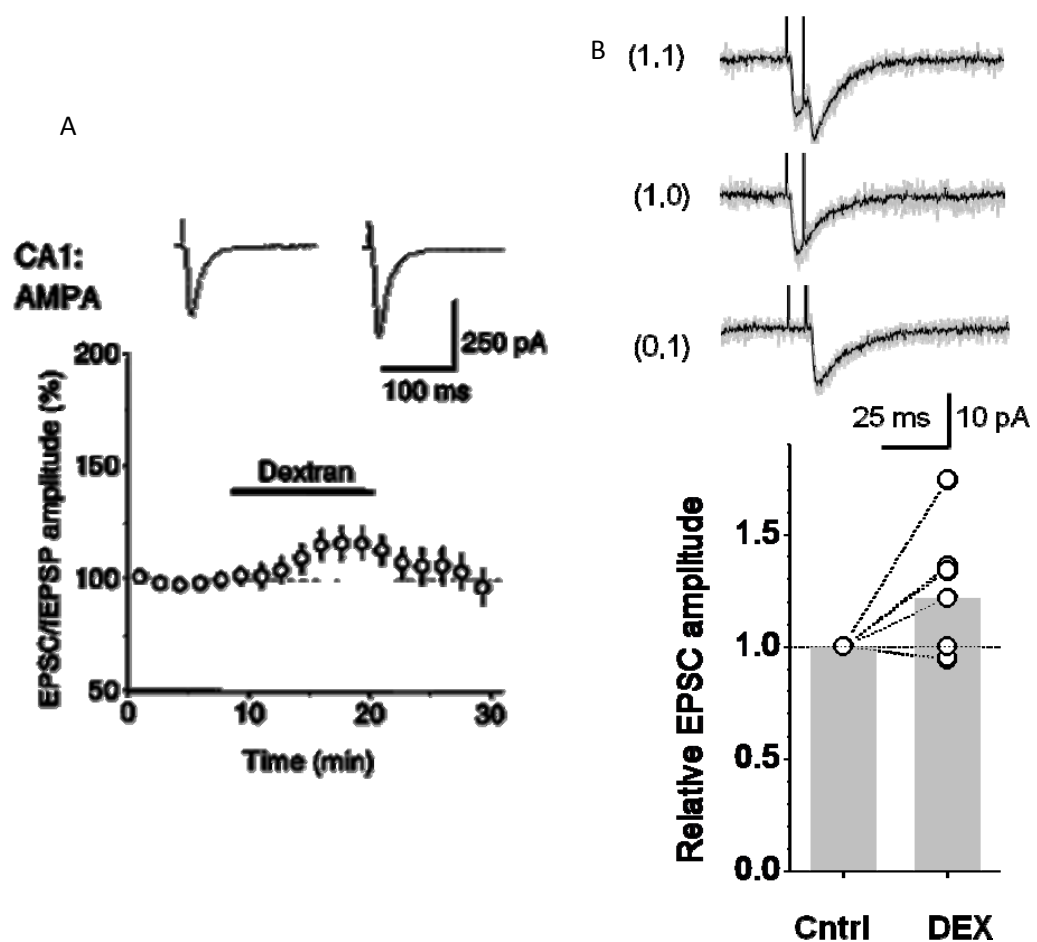


**Figure 23 Diffusion Retardation by Dextran Affects Postsynaptic Responses**

A: Summary of effect of dextran perfusion on AMPAR-mediated Schaffer collateral signals recorded in CA1 pyramidal cells, where whole cell EPSCs (inset, example,  $n = 11$ ) or fEPSPs ( $n = 12$ ) amplitude increases by  $16\pm 8\%$  (Min *et al.*, 1998)

B: Minimal stimulation protocol resulted EPSCs in CA1 pyramidal cells show an increase in amplitude  $21\pm 10\%$  ( $n = 7$ )

### ***Estimating intracleft diffusivity from its non-linear relationship to AMPAR-mediated EPSCs***

With measured fractional increase/decrease values for the EPSC amplitude ( $I$ ) and for the diffusion coefficient ( $D$ ) obtained in similar dextran experiments, we could fit them onto the predictions of 3D Monte-Carlo simulations regarding the intra-cleft diffusion coefficient (Figure 24), and as described earlier (Nielsen *et al.*, 2004). We therefore fitted a rectangle that represents the corresponding proportion in a log-log plot as shown in Figure 24. Two rectangles were constructed to show the mean and upper estimates according to the error in  $\Delta I/I$ . Both having a width representing 25% (as the error in  $\Delta D/D$  is negligible) decrease in diffusivity; and blue rectangle (mean value of  $\Delta I/I$ ) has a height represent 21% increase and red rectangle (higher end of estimation) has a height represent 31% increase in AMPARs-mediated postsynaptic response and width represent  $\Delta D/D = 25\%$  decrease in glutamate diffusivity

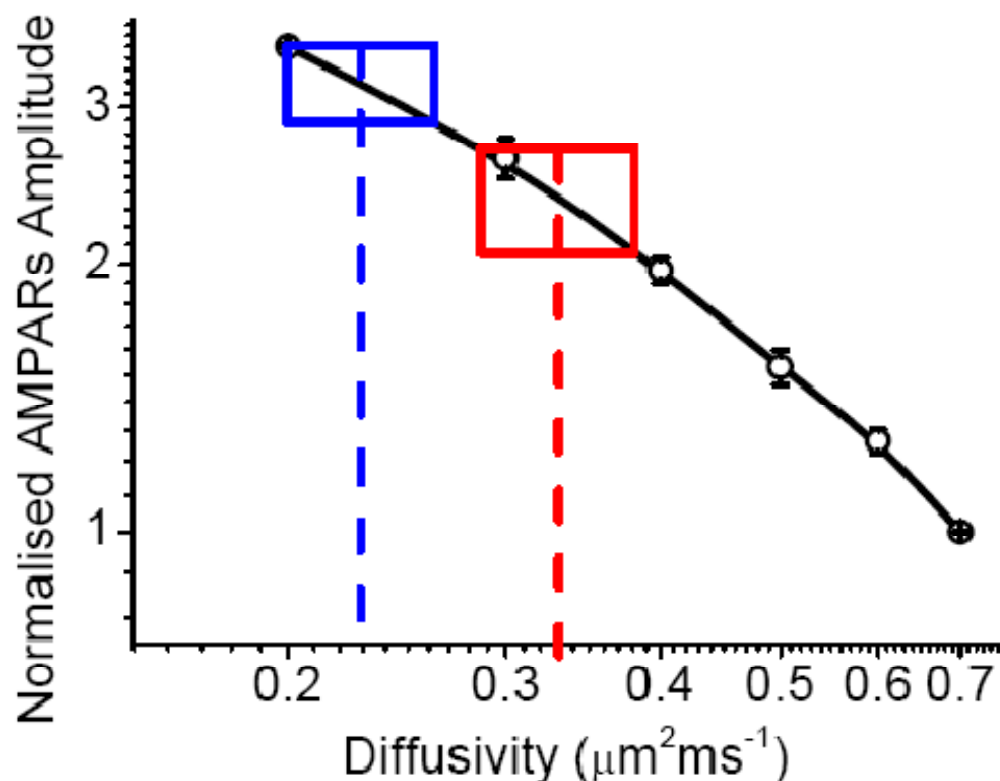


**Figure 24** Estimating the intrasynaptic diffusivity of glutamate

Log-log plot of the nonlinear relationship as shown in Figure 27C is extracted for transporter density equivalent to  $\sim 0.2\mu\text{M}$  (black circles); Estimation of intracleft diffusivity is estimated by using rectangles matching relative changes in both diffusivity (abscissa) and AMPAR-mediated EPSCs (ordinate). Average values (blue square), height represent  $\Delta I/I = 21\%$  increase in AMPARs-mediated postsynaptic response and width represent  $\Delta D/D = 25\%$  decrease in glutamate diffusivity; Higher end of estimation (red square), height represent  $\Delta I/I = 31\%$  increase in AMPARs-mediated postsynaptic response and width represent  $\Delta D/D = 25\%$  decrease in glutamate diffusivity

corresponds to an increase of 31% (upper error margin of  $\Delta I/I$ ). Blue rectangle gives an estimated glutamate diffusivity inside the synaptic cleft as  $D_{cleft} = 0.23 \mu\text{m}^2\text{ms}^{-1}$  and red rectangle estimates  $D_{cleft}$  to be  $\sim 0.33 \mu\text{m}^2\text{ms}^{-1}$ . Previous electrophysiological experiments in cerebella synapses propose a strikingly similar diffusivity value inside the synaptic cleft,  $\sim 0.33 \pm 0.13 \mu\text{m}^2\text{ms}^{-1}$  (Nielsen *et al.*, 2004).

Although the method provided a quantitative estimate for the  $D_{cleft}$ , it is highly sensitive to an experimental error in  $\Delta I/I$  value and, more importantly, to the underlying assumptions in the simulation paradigm (See 2.4.1). With a full 3D Monte-Carlo simulation, we conclude that the average  $D_{cleft} = 0.23 \pm 0.1 \mu\text{m}^2\text{ms}^{-1}$  for the diffusivity of glutamate in CA1 hippocampal pyramidal cell synapses. This value is much lower than in a free medium and even lower than macroscopic diffusivity  $D_{macro}$  estimated in CHAPTER 3. This seemingly contradictory result is however expected. Firstly, the synaptic cleft is densely packed with macromolecular obstacles imposing steric hindrance to the diffusing neurotransmitter molecules, which is consistent with electron microscopy evidence. Secondly, synaptic clefts occupy only 1-2% of the extracellular space in hippocampal area CA1 (Rusakov *et al.*, 1998) and therefore the macroscopic value  $D_{macro}$  represents the average diffusivity in the space outside synaptic clefts with geometric tortuosity effect.

We will use the estimated  $D_{cleft}$  value to examine the effects of diffusion on intrasynaptic responses using 3D Monte-Carlo model in CHAPTER 6.

## CHAPTER 5. RESULTS: INSTANTANEOUS DIFFUSION OF SMALL MOLECULES IN THE BRAIN EXTRACELLULAR SPACE MEASURED USING TRFAIM – A NANOSCOPIC VIEW

The traditional approaches to extracellular diffusivity (Section 1.5) including two-photon excitation imaging of a point-source (Figure 21) provide the volume-average estimates on the scale of 10-100  $\mu\text{m}$ . A different approach is required to estimate the instantaneous (nanometre-scale) diffusivity within average extracellular space, before molecules experience macroscopic obstacles to diffusion. Therefore, we looked into time-resolved fluorescent anisotropy imaging microscopy (TRFAIM, see Section 2.5 for methodological details).

The TRFAIM method has been around since the 70s, mainly based on frequency domain method, which measures differences in a phase shift of the emitted photon from frequency modulated excitation source as the indicator of fluorescent lifetime (Lakowicz, 2006). Only recently, with the development of better photon counting detectors and faster computers, one can start to use time-domain method, which measures the actual timing (at sub-nanosecond resolution) of the photon emitted from the source. This approach is now more sensitive than the frequency domain method. However, to apply the method in slice imaging, there are difficulties and one has to investigate the underlying assumptions carefully before proceeding (See section 2.5).

This method probes diffusion with  $\sim 1\text{nm}$  spatial resolution and  $< 1\text{ns}$  temporal resolution by assessing how the molecule interact with its immediate environment. This is typically constrained by micro-viscosity of the medium. We use the word 'micro-viscosity' in its loose sense, as conventional viscosity definition and measurement is not likely to apply in such situations when dimensions are getting closer to the Reynolds number of the molecules. However as we have shown in Section 2.5.1 (Figure 11A-C), in the first

approximation there is a linear relationship between rotational diffusivity ( $D_R$ ) / rotational correlation time ( $\theta$ ) and translational diffusivity ( $D_T$ ). Therefore, measuring rotational correlation time with TRFAIM should provide a direct probe for the local instantaneous mobility of molecules before any geometric hindrance takes place.

### ***Retardation of extracellular diffusivity in the organised brain tissue***

Thus the rotational correlation time ( $\theta$ ) provides a map of the instantaneous, rapid extracellular diffusivity of AF350 in hippocampal CA1 regions (Figure 25A-B). The results summarised for  $n = 11$  slices suggest that instantaneous diffusion of small soluble molecules in the extracellular milieu is retarded by up to  $\sim 30\%$  compared to a free medium ACSF, and that the layer of pyramidal cell bodies shows higher retardation values than that in the synaptic neuropil in *stratum radiatum* (Figure 25C).

The mean increase of rotational correlation time in slices corresponds to about 23% decrease in diffusivity in the extracellular space compare to that in ACSF (Figure 25C). Because synaptic clefts only occupy 1-2% of the extracellular space (Rusakov *et al*, 1998), the retardation we measured here is the average apparent viscosity retardation factor  $R_v$  (defined as  $R_a = R_t R_v$ ), ignoring extra slow down in the synaptic cleft. The measurements give  $R_v^{21^\circ\text{C}} = 1.3$  ( $\lambda_v = 1.14$ ), and indicates that  $D_{micro}^{21^\circ\text{C}} = D_f^{21^\circ\text{C}} / R_v^{21^\circ\text{C}} = 0.68 / 1.3 = 0.52 \mu\text{m}^2\text{ms}^{-1}$ . Since we also estimated  $D_{macro}^{21^\circ\text{C}}$  to be  $0.18 \mu\text{m}^2\text{ms}^{-1}$ , this predicts that  $R_t^{21^\circ\text{C}} = 2.89$  and  $\lambda_t^{21^\circ\text{C}} = 1.7$ . This is higher than the theoretical estimate (Hrabe *et al*, 2004) of 1.4-1.5 from Monte-Carlo simulations of random orientated space-filling convex cells, suggesting possible additional retardation mechanisms in real tissue, possibly space 'dead-ends' (Hrabetova *et al*, 2003). Without no current measurements at  $37^\circ\text{C}$ , we assume that  $\lambda_t$  holds the theoretical value of 1.4-1.5, then  $R_v^{37^\circ\text{C}} = R_a^{37^\circ\text{C}} / R_t^{37^\circ\text{C}} = 2.67 / 2.1 = 1.27$ , therefore  $\lambda_v^{37^\circ\text{C}} = 1.13$ . This still indicates a 20% decrease in diffusivity of glutamate, which gives  $D_{micro}^{37^\circ\text{C}} = 0.67 \mu\text{m}^2\text{ms}^{-1}$ .

The present results alleviate an important uncertainty of microscopic diffusivity of small molecules in the extent of extrasynaptic actions of

neurotransmitter such as glutamate, which depend strongly on local extracellular diffusivity (Rusakov & Kullmann 1998a; Barbour, 2001). Therefore we shall explore diffusivity values in the extrasynaptic milieu in our 3D Monte-Carlo models using the estimate calculated here to measure the possible effects of diffusion changes on extrasynaptic responses in CHAPTER 6.

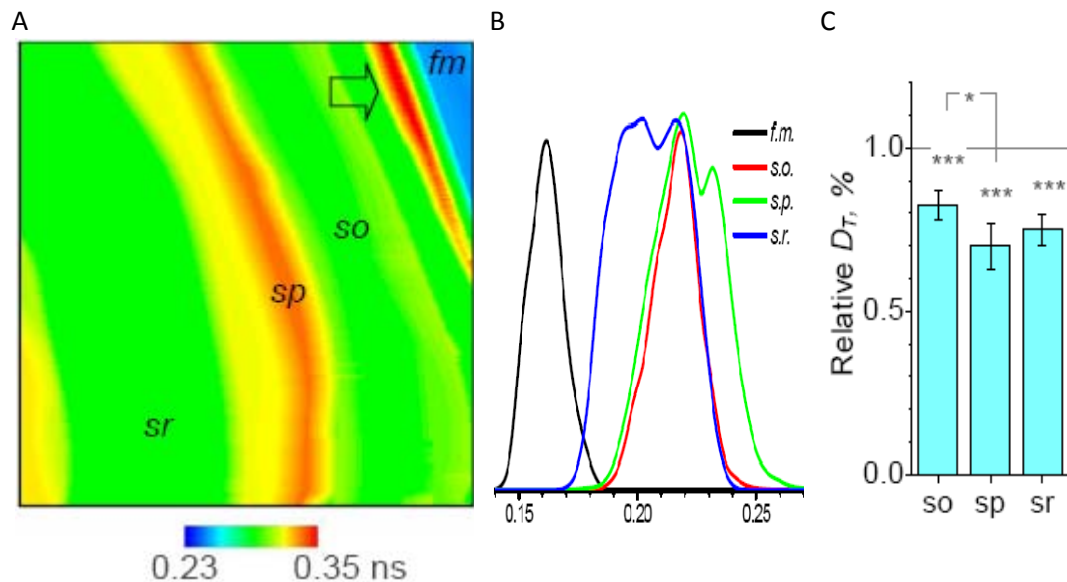


**Figure 25 A Map of Instantaneous Extracellular Diffusivity in Area CA1 of the Hippocampus**

A: A characteristic map of  $\theta$  (inversely proportional to  $D_T$ ) for extracellular AF350 in the acute hippocampal slice fragment depicted in Figure 16A. Block arrow, damaged/dead tissue fragment; tissue layers are indicated as in Figure 16A. (Manually selected ROI analysis employed)

B: Fast fluorescence rotational correlation time ( $\theta$ , abscissa, absolute values) distribution within each region of interests as indicated in A using auto parameter map generation in the same sample as A. Ordinate normalised to maximums of distribution in each ROIs.

C: Statistical summary of  $D_T$  values (relative to free medium, dotted line) measured in  $n=11$  slices and averaged across the respective hippocampal areas, as illustrated in Figure 16A. \*\*\*,  $p < 0.005$ ; \*,  $p < 0.02$ .

## CHAPTER 6. RESULTS: DIFFUSION OF GLUTAMATE IN THE SYNAPTIC CLEFT AND ITS INFLUENCE ON POSTSYNAPTIC RESPONSES – A MICROSCOPIC VIEW

Activation of fast ionotropic receptors such as NMDARs and AMPARs in the vicinity of the synaptic cleft determines the shape of fast post-synaptic responses. Any environmental parameters such as reaction site density, medium viscosity in the vicinity will influence the diffusion of glutamate and consequently the post-synaptic response profile. Post-synaptic response profile could also depend on the source of the glutamate - elements such as number of glutamate molecules released from the vesicle, the mode of release (single- or multi- vesicular), or the position of the release site with respect to the active zone. They can also depend on the channel density and kinetics. Clearly glutamate diffusion per se in the extracellular medium should be critical to the diffusion-reaction process.

A less perspicuous factor is possibly the distribution of extrasynaptic transporters such as EAAT1/EAAT2 that acts as buffer and sink for diffusing glutamate molecules (Diamond & Jahr, 1997; Tzingounis & Wadiche, 2007). Glial membranes enriched in transporters only represent ~13% of cell membranes in area CA1 (Lehr & Rusakov, 2002) and on average surround only a third of the synaptic circumferences (Ventura & Harris, 1999). In order to establish whether transporter distribution has any significant effect on fast synaptic transmission, we will examine in detail with the help of 2D and 3D Monte Carlo model simulations. Also the role of glial transporter EAAT1/2 (Lehre *et al.*, 1995; Chaudhry *et al.*, 1995) and neuronal transporter EAAT3 (Rothstein, 1994) during brain development poses interesting questions as the role they play in synaptic transmission (Furuta *et al.*, 1997). We shall also examine the effect of both extrasynaptic and intrasynaptic transporters on intra and extra synaptic fast ionotropic receptors.

### ***Influence of extrasynaptic EAAT1/2 transporter distribution on intrasynaptic receptor activations***

Do glutamate transporters outside the synaptic cleft affect receptor activation inside the cleft? The 2D MC model has given some tentative ideas on the effects of extrasynaptic transporters' position, shape and density.

Simulations as illustrated in Figure 36A (Appendix A), shows that the proximity of the transporter patch hardly made any difference to the postsynaptic responses, be it AMPAR mediated or NMDAR mediated responses (Figure 26A). Simulation as illustrated in Figure 36A,B tells us that the coverage of the perisynaptic area by the transporter has no significance, the percentage differences are less than trial-to-trial variations (Figure 26B).

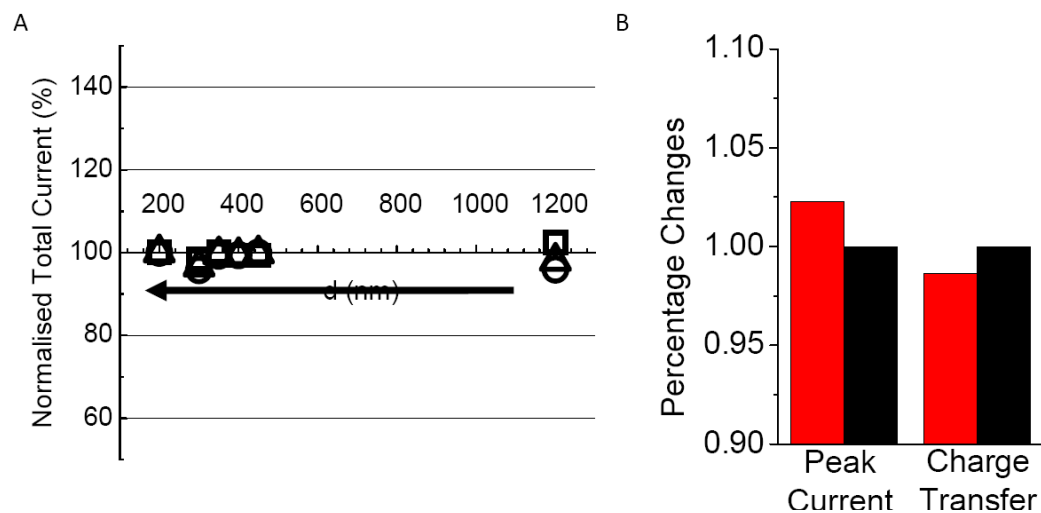


**Figure 26 Effects of Transporter Distance and Coverage Symmetry (2D MC Model) on Fast Synaptic Responses**

A: As transporter patch approaching the active zone (indicated by arrow, scenario illustrated in Figure 36A), the receptor responses did not change for neither AMPARs-mediated (Square) nor NMDARs-mediated (Circle) responses. Total current, triangle.

B: The shape of the transporter patch, either semi-circular (Figure 36A, red bar) or circular (Figure 36B, black bar, normalised to unity) with the same transporter density, will not affect the postsynaptic responses whatsoever in terms of either peak current (left) or total charge transfer (right).

Simulations as illustrated in Figure 36B,D show that with a small concentric ring, the effects of transporter density on synaptic transmission is minimal, either in term of peak response or charge transfer (Figure 27B) or decay time. However with a larger concentric ring of the same density, the

influence on the synaptic transmission becomes more prominent, especially when the glutamate diffusivity is higher (Figure 27A). Upon closer comparison, it is clear that at 0.5mM, the smaller ring has only 407 transporters, but the larger ring has 2510 transporters, a number that is comparable to the number of glutamate released into the environment. It is therefore clear that the patch of transporters have to have at least the capacity to compete with the number of glutamate released. In the case of small concentric ring almost 100% of the transporters are occupied within few milliseconds (compare to larger ring shortly after release; Figure 35). Even with the larger ring, at estimated glutamate diffusivity ( $\sim 0.4\mu\text{m}^2\text{ms}^{-1}$  as average between intra- and extra-synaptic diffusivity) the difference in postsynaptic responses between 0 and 0.5mM is only about 15% (Figure 27A).

These results suggest that the activation of the synaptic receptors is limited mainly by diffusivity, simply because once the overwhelming number of glutamate molecules are released into the cleft, there is no other binding proteins there to compete with the receptors. By the time the glutamate diffusive wave reached transporters, most of the receptors are bounded with one or two glutamates already.

Results from the 3D model will focus on AMPARs only as restriction on the simulation time, as well as AMPARs mediates the bulk of the synaptic response within 5 ms post-release. Because such influences might in principle depend on the intra-cleft diffusion coefficient of glutamate (Nielsen *et al.*, 2004), we explored this parameter around its predicted average value of  $\sim 0.40\mu\text{m}^2\text{ms}^{-1}$ . The results indicate that extrasynaptic transporters have little influence on AMPAR responses: varying the transporter numbers from none to 1500 results in only a <10% variation in receptor activation, irrespective of local glutamate diffusivity (Figure 27C-D).

In most physiological situations, cells fire repetitively and one has to ask whether transporters might have an effect in such cases when they could be saturated. So we simulated an evoked five pulse train at 200hz in the presence or absence of 3000 EAAT1 transporters. It is clear that even at this high frequency, transporters are likely to be swamped by glutamate. There are little

differences to the postsynaptic response (Figure 28A). During such repetitive firing, AMPARs are being pushed into desensitised states (Figure 28B), which is consistent with the experimental observations that short term

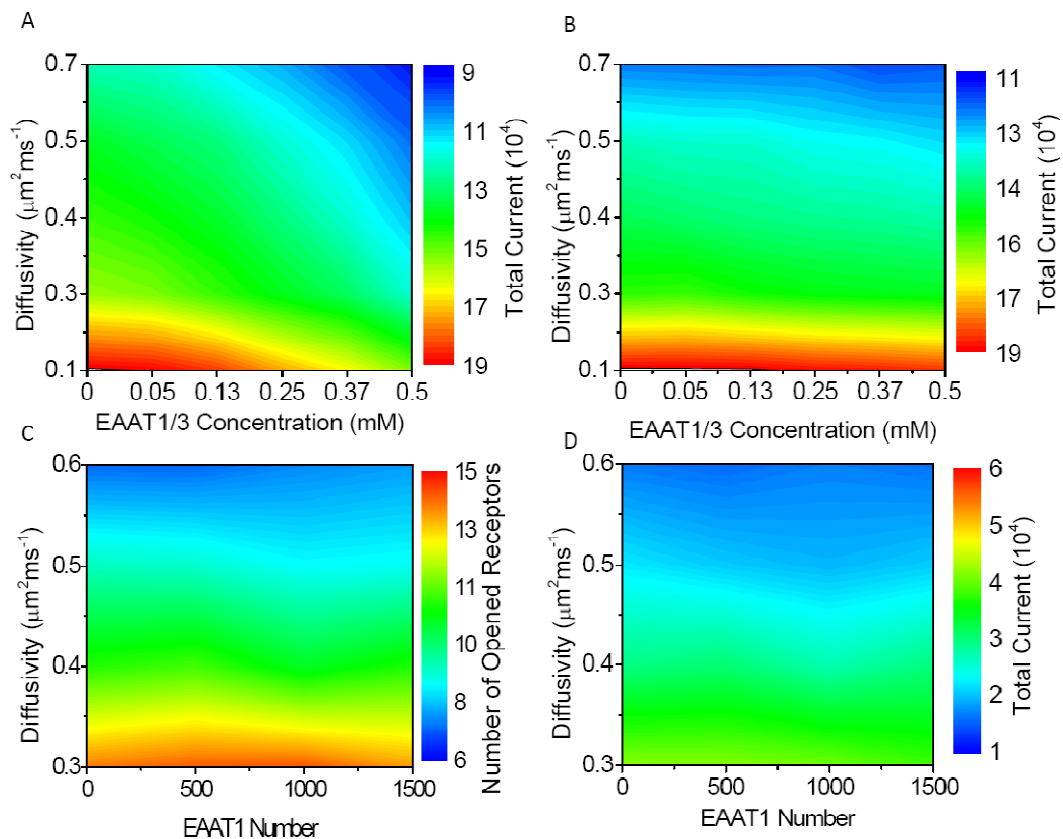


**Figure 27 Effect of Transporter Density (MC Models)**

A-B : In 2D MC model, a large concentric ring (A, as illustrated in Figure 36D) with transporter density varying between 0-0.5mM (abscissa) reduces the postsynaptic responses (false colour scale, the total charge transfer) at high density values and high diffusion coefficient (ordinate) of glutamate, however this does not appear to be the case with a small concentric ring (B, as illustrated in Figure 36B) with the exact same density of transporters.

C: In 3D MC model, the number of perisynaptic glutamate transporters (abscissa, linear scale, 0-1500 in number; see Figure 7D for transporter location; EAAT1 kinetics is adopted) has little effect on the peak amplitude of AMPAR-mediated EPSCs (false colour scale, the peak number of open receptors) over a plausible range of glutamate diffusion coefficient inside the cleft (ordinate)

D: The total charge transfer of AMPARs-mediated EPSCs under the exact same condition as C, showing little differences, and as traces suggests the variability in the shape of EPSCs is no larger than that one would get from fixed transporter density

depression of AMPARs at particular synapses due to desensitised state could be used as a protective mechanism to repetitive exposure to synaptically released glutamate (Jones & Westbrook, 1996; DiGregorio *et al.*, 2007).

This reinforced the idea that only local competition with the receptors could possibly influence the postsynaptic responses.

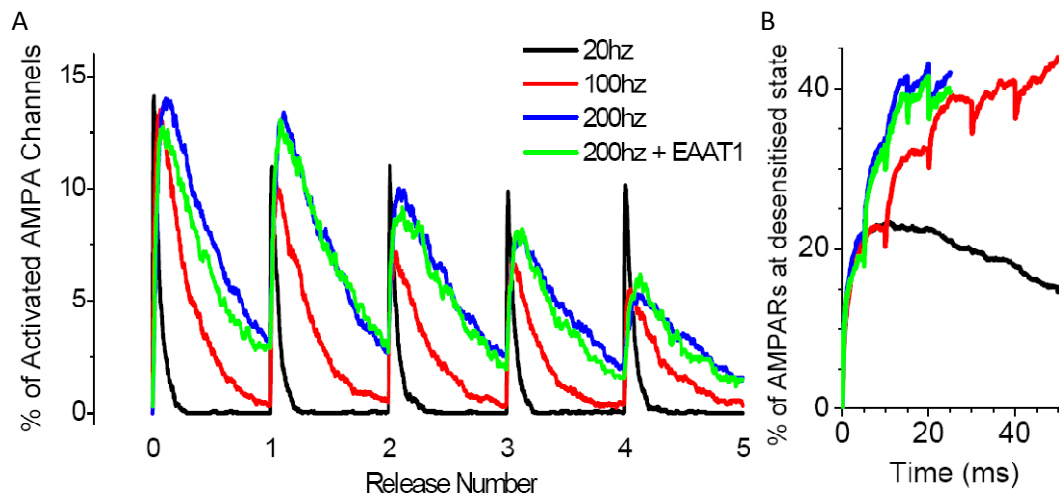


**Figure 28 Transporter Effect on Repetitive Stimulation**

A: Time course of AMPAR activation (number of receptors out of 80) during repetitive releases of glutamate at 20, 100 and 200Hz, as indicated by colours; time scales are adjusted to synchronise releases. Transporters added at 200Hz show little effect on AMPAR activation (the effect of transporter was negligible at 20 and 100Hz; data not shown).

B: Time course of AMPAR desensitisation (GluRD state, Figure 6A) in simulation experiments described in (A). Other notations are as in (A)

### ***Influence of intrasynaptic EAAT3 transporter distribution on intrasynaptic receptor activations***

Although the transporter identity and the extent of intra-synaptic (as opposed to extra-synaptic) glutamate uptake are debated, the main candidate at hippocampal synapses is the neuronal transporter EAAT3 (Diamond 2001; Danbolt, 2001; Furuta *et al.*, 1997; He *et al.*, 2000). Simulations predicted that, in striking contrast with extra-synaptic transporters, only few dozen of intra-synaptic transporter molecules could reduce significantly activation of local AMPARs (Figure 29). This result also proposes that, if glutamate uptake occurs inside the synaptic cleft, its blockade should facilitate AMPAR-mediated responses.

To test whether such facilitation indeed occurs, AMPAR-mediated EPSCs was recorded in CA1 pyramidal cells either during miniature synaptic events (in 1  $\mu$ M TTX) or in response to minimal stimulation which activates

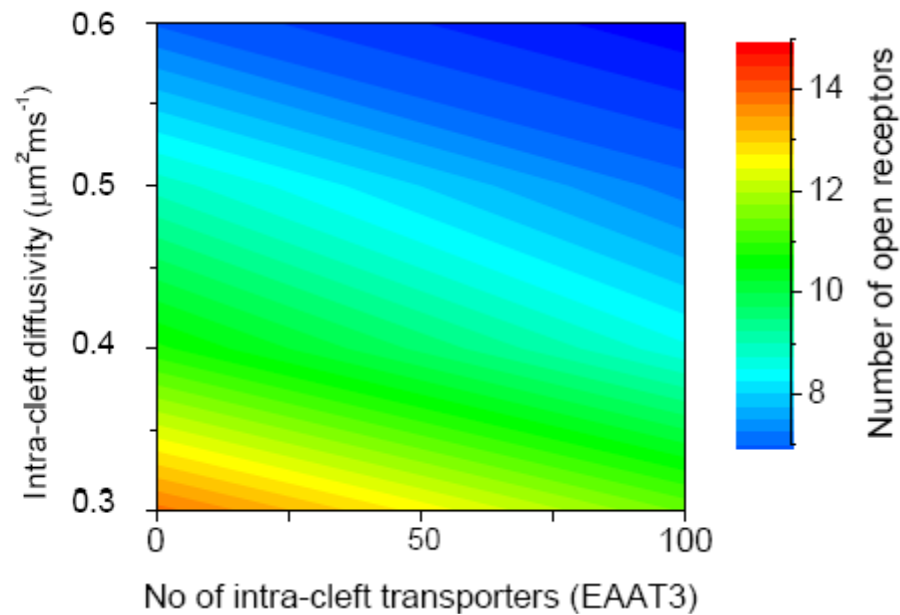


**Figure 29** Intrasynaptic Transporter Effect on AMPARs responses

Intra-synaptic glutamate transporters (abscissa; EAAT3 kinetics is adopted), if present, should attenuate AMPAR-dependent EPSCs (false colour scale, number of opened receptors) over a range of glutamate diffusion coefficient inside the cleft (ordinate)

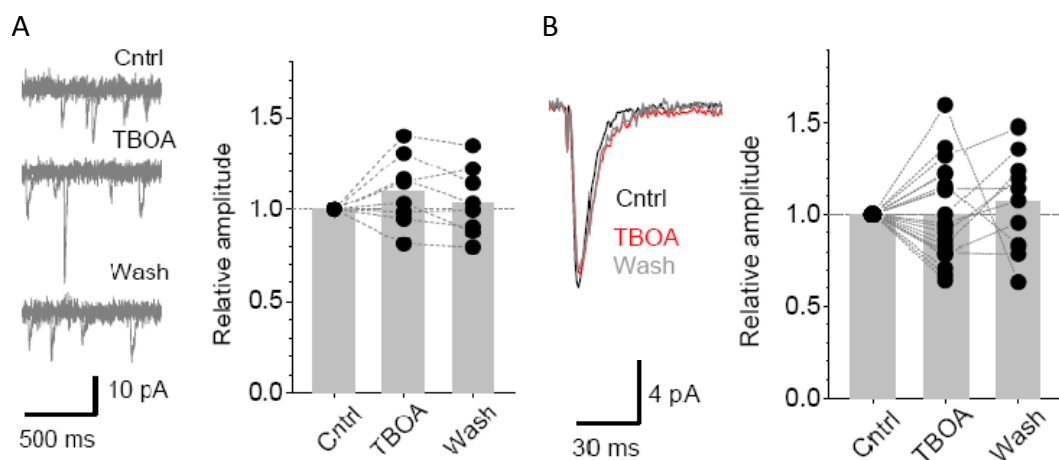


**Figure 30** TBOA Experiments

A: Blockade of glutamate uptake with 50 $\mu$ M TBOA has no detectable effect on miniature AMPAR-dependent responses in CA1 pyramidal cells. Traces, representative examples (three consecutive traces overlapped in each panel; Cntrl, control; TBOA, application of TBOA; Wash, washout). Plot, summary; dots, individual cells; grey bars, average values; dotted lines connect data points obtained in the same cell, Average amplitude changes in TBOA and after washout relative to control are, respectively,  $1.09 \pm 0.06$  and  $1.04 \pm 0.06$  ( $n = 9$ )

B: Blockade of glutamate uptake has no effect on minimal stimulation responses (AMPA-mediated) in CA1 pyramidal cells. Traces, representative examples in control (black), during TBOA application (red) and during washout (gray; average of 20 traces each). Plot, summary; other notations are the same as in C. Average amplitude changes in TBOA and after washout relative to control are, respectively,  $1.00 \pm 0.06$  and  $1.07 \pm 0.089$  ( $n = 21$  and  $n = 11$ )

only one or very few synapses on the recorded cell (Dobrunz & Stevens, 1997). In both cases, the low density of active synapses should exclude any inter-synaptic influence of escaping glutamate, with or without intact glutamate uptake (Arnth-Jensen *et al.*, 2002; Scimemi *et al.*, 2004), reflecting conditions of the single-synapse model. Blocking glutamate uptake with 50  $\mu\text{M}$  TBOA had no detectable effect in either case (Figure 30, A and B; in control experiments, TBOA completely blocked glutamate uptake currents recorded in local astrocytes). Because our model predicts that only 20-25 transporter molecules inside the cleft should reduce AMPAR responses appreciably (by 15-20% See Figure 29), the electrophysiological results argue for smaller numbers of intracleft transporters.

### ***Influence of extrasynaptic EAAT1/2 transporter distribution on extrasynaptic receptors activation in the synaptic vicinity***

Another important physiological case is the coincidence of glutamate receptors and transporters in the extrasynaptic domain. Therefore we tested how extrasynaptic transporters regulate activation of extrasynaptic receptors. This is particularly important to spill-over effects, where escaped glutamate targets high-affinity NMDARs (Tovar & Westbrook, 1999; Prybylowski *et al.*, 2002).

How strongly does the uneven occurrence of transporters affect glutamate receptor activation at different locations outside the synaptic cleft? To determine whether the local non-homogeneities in transporter distribution play a role in local NMDAR activation, we first placed a small cluster of 20 NMDARs at different distances from the release site (synaptic cleft centre) using the Monte Carlo model environment (Figure 8C), including extrasynaptic areas either enriched or devoid of glutamate transporters (Figure 31B; in these simulations, we assumed that the neuronal membranes were sufficiently depolarized to relieve the  $\text{Mg}^{2+}$  block of the NMDARs in question). Because of the unreasonably long time (weeks) required for the Monte Carlo model to simulate microscopic events for 200 ms post-release in each set of conditions, we documented the NMDAR charge transfer between 0-20 ms post-release. This parameter should faithfully represent the degree of receptor activation

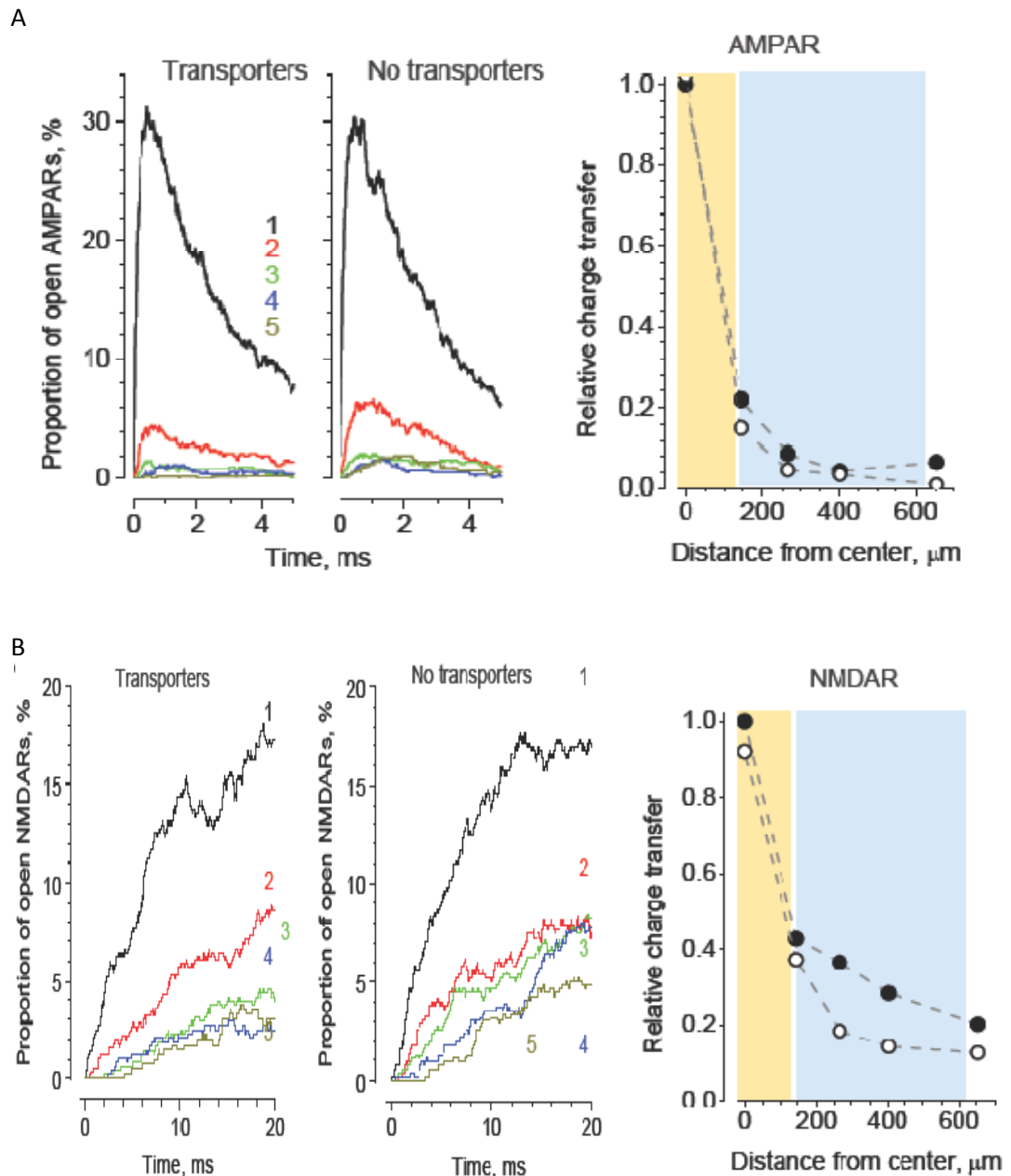


**Figure 31 Extrasynaptic Receptors**

A: Time course of AMPAR opening at the test locations as indicated in Figure 8C, with and without glutamate transporter (28 run average); Right-most panel shows average charge transfer carried by activated AMPARs at different curvilinear distances from the cleft centre (values relative to the charge transfer by AMPARs located in the synaptic cleft centre with no transporters). Hollow and black circles, data with and without transporters, respectively; yellow and blue shading, synaptic cleft dimensions and the spatial extent of extrasynaptic transporters (when they are present), respectively.

B: Time course of NMDAR opening at the same test locations as in A; Right-most panel shows charge transfer carried by activated NMDARs between 0-20ms post-release. Notations are same as in A

because the amount of glutamate remaining in the system by that time point is negligible. The results indicate that activation of intra-synaptic NMDARs is largely insensitive to the transporter actions whereas activation of extra-synaptic NMDARs is clearly suppressed when these receptors occur in the vicinity of transporters (Figure 31B). In the latter case, the NMDAR activation level at distances of up to 600 nm from the release site remained above 10% of that inside the cleft (Figure 31B). This is somewhat higher than earlier theoretical estimates, in which glutamate uptake was distributed evenly throughout the space (Scimemi *et al*, 2004; Lehre & Rusakov, 2002; Franks *et al*, 2002). By comparison, activation of the low-affinity AMPARs activated in similar conditions declines steeply with distance from the release site, with or without transporter action (Figure 31A), consistent with previous reports (Wahl *et al.*, 1996; Lehre & Rusakov 2002; Raghavachari & Lisman, 2004).

### **Summary**

We have shown that glial transporter density and position with respect to the intrasynaptic release site have minimal effects on intrasynaptic receptor activations due to high number of receptors. However, they do have significant modulation effect on high affinity extrasynaptic receptors that cohabit in the same extracellular domains through local competition for glutamate. Similar modulation effect can occur with intrasynaptic neuronal transporters, but the lack of experimental evidence showing any modulation effect when neuronal transporters are blocked suggests very few functional neuronal transporters exist in the synaptic active zone. All evidence suggests that at low glutamate concentrations, transporters provide shielding for local high affinity receptors, like the extrasynaptic NMDARs. With increasing glutamate concentration, such as in the synaptic active zone, transporters need to be more localised to the receptors (for example neuronal transporters) to provide shielding purposes for either low affinity AMPARs or high affinity NMDARs. There is of course a level of glutamate beyond which, transporters are saturated and can no longer offer any protection for the receptors. In the next chapter we shall look at what happens when astrocytes fail (i.e. majority of transporters are not functioning).

## CHAPTER 7. RESULTS: EXTRACELLULAR LANDSCAPE OF GLUTAMATE IN THE NEUROPIIL – A MACROSCOPIC VIEW

### *Steady-state equilibrium of glutamate release and uptake: high safety factor*

In the hippocampal neuropil, glial glutamate transporters are thought to provide >90% of glutamate uptake (Danbolt, 2001). Given their average extracellular concentration  $T = 0.2$  mM (Lehre & Danbolt, 1998) and the upper limit cycling rate  $k_c \sim 0.05$  ms<sup>-1</sup> (Bergles & Jahr, 1998; Wadiche & Kavanaugh, 1998), they should sustain steady-state glutamate uptake at a rate of up to  $k_c T = 10$  μM·ms<sup>-1</sup>. How does this compare with glutamate releases in the course of synaptic activity? In area CA1, excitatory synapses occur at a density of  $N_V \approx 2$  μm<sup>-3</sup> (Geinisman *et al.*, 1992; Rusakov *et al.*, 1998). Classically, an action potential arriving at one of such synapses releases one (occasionally more (Oertner *et al.*, 2002)) synaptic vesicle with the probability  $P_r = 0.2-0.5$ . Each vesicle release corresponds to  $n_g = 2000-3000$  glutamate molecules (Harris & Sultan, 1995; Zampighi & Fisher, 1997; Takamori *et al.*, 2006) (although see (Schikorski and Stevens, 1997)). The extracellular space fraction  $\alpha$  in the CA1 area is 0.15-0.20 (McBain *et al.*, 1990; Perez-Pinon *et al.*, 1995) and the axonal firing rate  $f$  is very unlikely to exceed 100 Hz. These data suggest that the upper limit glutamate release rate, with all axons firing continuously, is  $n \cdot f \cdot P_r \cdot N_V \cdot \alpha^{-1} \cdot N_A^{-1} \approx 2-5$  μM·ms<sup>-1</sup> (here  $N_A$  is the Avogadro's number). However, the assumption that all synapses discharge glutamate at this rate is not plausible. In fact, experiments in acute slices suggest that simultaneous discharges from only 3-5% of local excitatory synapses are sufficient for a CA1 principal neuron to fire (Arnth-Jensen *et al.*, 2002; Scimemi *et al.*, 2004). Adopting a conservative estimate of 10%, synchronous synaptic firing thus corresponds to an average (time-integrated) glutamate release at a rate of 0.2-0.5 μM·ms<sup>-1</sup>. This suggests that synaptic activity occurs in this area with the glutamate uptake safety factor of 20-50, which is consistent with experimental

observations (Herman & Jahr, 2007; Diamond & Jahr, 2000). Could, nonetheless, such synaptic activity generate long-term, long-range gradients of extracellular glutamate?

### ***Ambient glutamate concentration and uptake failure***

Simulation snapshots in Figure 32 depict extracellular glutamate profiles produced at four different levels of glial glutamate transporters representing 100%, 10%, 5% and 1% of the baseline GLAST/GLT1 (Glutamate Aspartate Transporter/Glutamate Transporter) expression measured in the CA1 neuropil (Lehre & Danbolt, 1998). The results indicate that glutamate is unlikely to escape beyond 1-2  $\mu\text{m}$  outside the active synaptic pools, unless the transporter concentration is drastically reduced. Conversely, sustained synaptic firing inside the active pool could elevate the local background glutamate concentration by a small but significant amount, up to 1-3  $\mu\text{M}$

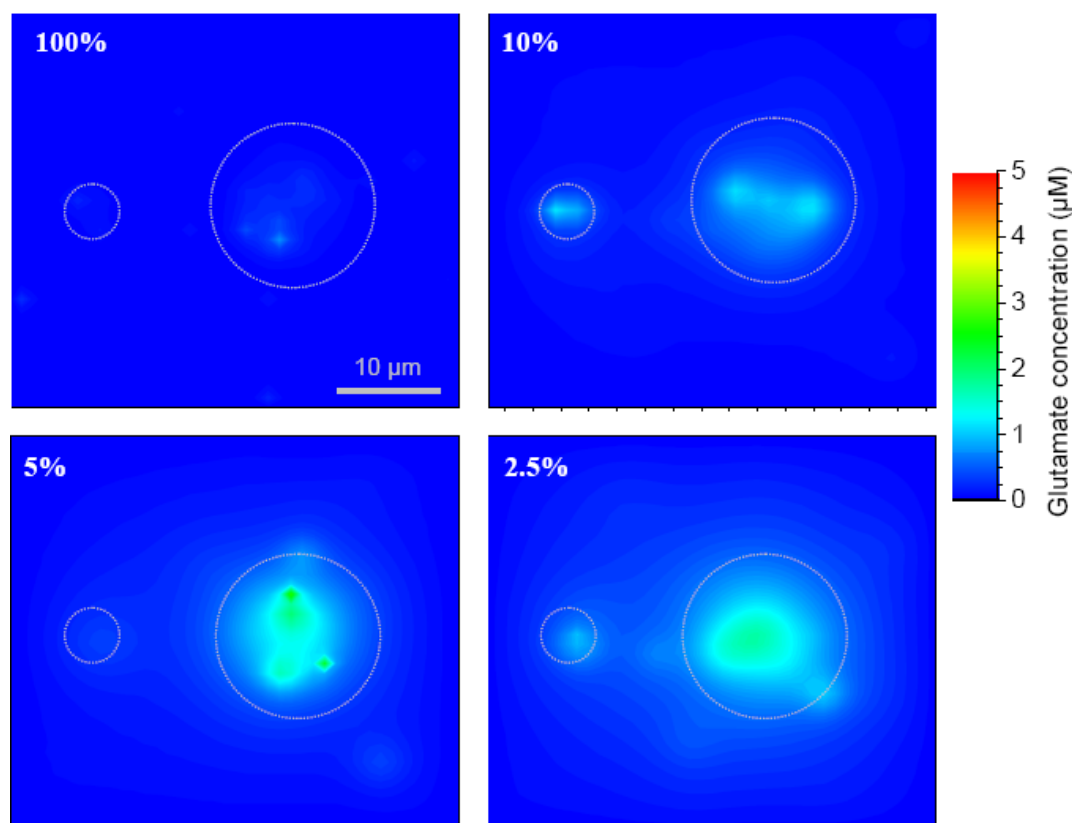


**Figure 32 Macroscopic Glutamate Density Affects Glutamate Concentration Gradient**

Snapshots of the extracellular glutamate concentration landscape in a neuropil cross-section through the centre of the two active synaptic pools (Figure 9B) in different conditions of uptake (indicated by the percentage of the functional glutamate transporters; baseline is 0.2mM). False colour scale, concentrations.

(averaged over individual 250 nm space partitions including those containing no glutamate release sites). The latter is consistent with detectable activation of extra-synaptic NMDA receptors ( $K_d = 1\text{-}2 \mu\text{M}$ ) in CA1 pyramidal cells following synchronous excitation of multiple Shaffer collaterals (Asztely *et al.*, 1997; Arnth-Jensen *et al.*, 2002; Scimemi *et al.*, 2004).

### ***Transporter patterns and glutamate gradient***

Conversely, we sought to test whether the uneven distribution of transporters could generate long-term gradients of ambient glutamate. We therefore divided the simulation arena into four volumes expressing different levels of transporters, from 1% to 100% of the baseline 0.2 mM. (Figure 33) We combined uneven transporter distribution with uniform glutamate releases confined to the active pools (Figure 33), and low background leakage (See 2.4.2). The simulation outcome shows that the transporter density heterogeneity results in concentration 'steps' (1-2  $\mu\text{m}$  wide transition boundaries) at an interface between any two different transporter levels. This illustrates how the patterned distribution of transporters could effectively 'direct' glutamate escape towards areas with a lower transporter level.

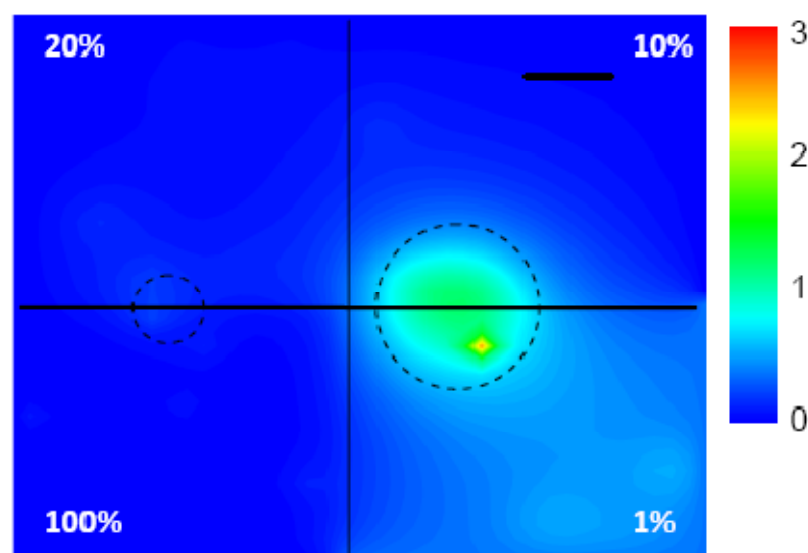


**Figure 33 Macroscopic Transporter Density Shapes Glutamate Concentration Gradient**

Snapshots of the extracellular glutamate concentration landscape in a neuropil cross-section through the centre of the two active synaptic pools (Figure 9B) in quadrants with different functional transporter density (as indicated by the percentages; baseline is 0.2mM). False colour scale, concentrations.

## CHAPTER 8. DISCUSSION

In this thesis we have introduced in detail the imaging and computational methods. We've shown the results obtained from imaging experiments and biophysical modelling to measure the glutamate diffusivity at all spatial scales in brain hippocampal slices and the effects of glutamate diffusivity and glutamatergic transporter properties on intra- and extra-synaptic transmissions and long range glutamate diffusion profile in large tissue volumes. To summarise, the main findings of this thesis are:

1. Diffusion coefficient of glutamate at different environments from ACSF solutions to the intermembrane extracellular milieu to the synaptic cleft to the convoluted extracellular tissue volumes are all measured accurately. The corresponding retardation factors contributing to medium viscosity and geometric tortuosity of the tissue are derived from experimental data for the first time.

2. Extrasynaptic glutamatergic transporters have no effect on postsynaptic responses initiated from release of the same synapse. However, they can significantly decrease activation of high affinity extrasynaptic receptors from the same release by providing a source of local competition for glutamate.

3. Few dozens of intrasynaptic glutamatergic transporters could potentially alter synaptic transmission, but evidence of insensitivity from glutamate transporter blockade experiments suggests that the number of functioning intrasynaptic transporters is minimal.

4. Long range ambient glutamate concentration profile in the extracellular space is controlled by astrocytic transporters. Even with sustained activations, volumes covered with healthy astrocyte will not exert any significant increase in glutamate concentration into neighbouring volumes. When astrocytic transporter fails, though glutamate concentration in that domain will reach toxic level, neighbouring domains with healthy transporter density will not have their glutamate levels elevated significantly.

In the following sections, these results will be discussed in a broader context and an outlook towards possible future experiments.

### ***Space-average glutamate diffusivity in the brain extracellular space***

Even though it is evident that diffusion coefficient of glutamate is critical to synaptic transmissions, and many experimental attempts have been made to establish diffusivity of glutamate on both microscopic (Nielsen *et al.*, 2004) and macroscopic levels (Summary by Nicholson, 2001), there are however few critical parameters missing from our repertoire. It has been shown that the brain extracellular space is a tortuous medium, where tortuosity is defined as  $\lambda = \sqrt{(D/ADC)}$ . However, there are two distinctive components to  $\lambda$ , namely the geometrical tortuosity and medium viscosity. Theoretical attempts have been made to establish the contribution of the two components (Rusakov & Kullmann, 1998b; Hrabe *et al.*, 2004), but for the first time we are able to separate the viscosity components of diffusion retardation from the tortuosity  $\lambda$  experimentally.

Table 2 summarised all the diffusivity measurements and respective retardation factors. In CHAPTER 3 we estimated the diffusivity of glutamate in ACSF solution ( $D$ ) from the diffusivity of AF350 in the same medium. After take the advantage of TRFAIM and the linearity between rotational and translational diffusivity of small spherical molecules, we established that the medium viscosity  $\lambda_v$  accounts for a smaller proportion than geometric tortuosity  $\lambda_t$ . Since that synaptic active zones represent only a small proportion (1-2%) of the extracellular space in area CA1 (Rusakov, 1998), the  $\lambda_v$  here only represent average diffusion retardation due to medium viscosity in the interstitial space unhindered by cellular obstacles and devoid of synaptic active zones. This gives us the  $D_{micro}$ , which we used in 3D Monte-Carlo model for glutamate diffusivity outside the synaptic cleft. To access glutamate diffusivity inside the cleft, we used the two-photon point source diffusion retardation with dextran solution combined with electrophysiology recording under the same condition. This yielded  $D_{cleft}$  to be  $0.23 \mu\text{m}^2\text{ms}^{-1}$ , which is

T =	D	$\lambda_v$	$D_{\text{micro}}$	$\lambda_c$	$D_{\text{cleft}}$	$\lambda_t$	$D_{\text{macro}}$	$\lambda_a$
21°C	0.68	1.14	0.52	1.26***	n/a	1.7	0.18	1.94
37°C	0.86	1.13	0.67	1.4-1.7**	0.23	1.45*	0.32	1.59

**Table 2 Summary of Glutamate Diffusivity at Different Scales**

Unit  $\mu\text{m}^2\text{ms}^{-1}$ ; T = Temperature; D = Diffusivity in ACSF solution;  $D_{\text{micro}}$  = Microscopic diffusivity inside extracellular space;  $D_{\text{cleft}}$  = Microscopic diffusivity inside the synaptic cleft;  $D_{\text{macro}}$  = Macroscopic diffusivity (ADC equivalent);  $\lambda_v$  = Viscosity factor;  $\lambda_t$  = Geometric tortuosity factor;  $\lambda_a = \lambda_v \times \lambda_t$  (The  $\lambda$  in conventional definition);  $\lambda_c$  = apparent cleft retardation factor; \* theoretical estimate; \*\*estimated assuming  $D_{\text{cleft}} = 0.23-0.33$ ; \*\*\*estimated assuming  $D_{\text{cleft}} = 0.33$

smaller than the previous estimate of  $\sim 0.33 \mu\text{m}^2/\text{ms}$  (Nielsen *et al.*, 2004) inside cerebellum, although 0.33 is within the upper range of our estimates. Considering the error margin in both assessments, it is consistent with each other. Taking the estimated value of 0.23-0.33, one can estimate the retardation inside the synaptic cleft,  $\lambda_c = D_{\text{micro}} / D_{\text{cleft}}$ , which is 1.3-1.7. This retardation factor is much higher than the medium viscosity factor ( $\lambda_v$ ), suggests intra-synaptic diffusion is likely to be hindered by numerous macromolecular obstacles (protein scaffolding, carbohydrates' chains, receptor domains, etc.) filling the synaptic cleft (Tanaka *et al.*, 2000; Zuber *et al.*, 2005), which is evident from the EM evidence. Geometrical tortuosity has been studied theoretically (Rusakov & Kullmann, 1998b; Hrabe *et al.*, 2004), estimation has been give between 1.2-1.6 based on the assumption that extracellular space is isotropic and cell orientation is random. However our estimation based on  $\lambda_v$  and  $\lambda_a$  measurements suggests that, geometric tortuosity  $\lambda_t$  at 21°C is 1.7, which is higher than the maximum theoretical prediction. This could due to possible macro-domain dead space (Hrabetova *et al.*, 2003; Hrabetova, 2005), which increase apparent geometric tortuosity and overall  $\lambda_a$ . This is indeed the case at 21°C,  $\lambda_a$  is marginally higher than previously measured values of 1.5-1.7, and at 37°C our estimate of 1.59 is in complete agreement with previous results. It is also observed that in ischemia models,  $\lambda_a$  can rise to as high as 2.0 with drastically reduced volume fractions (Sykova, 2005). Reduction in volume fractions could also be a contributing source to high  $\lambda_a$  at 21°C, as to which components, viscosity, tortuosity or slice health it is hard to speculate, as we did not measure viscosity components at 37°C. This is not technically challenging, though not without minor hurdles such as refractive index changes. We currently are planning on map out all

regions of hippocampal slices under both room temperature and physiological temperature and at various pathological states.

In light of all measurements and estimations, the conventional tortuosity definition based on  $\sqrt{(D/ADC)}$  could be termed  $\lambda_a$ , as the ECS is tortuous ( $\lambda_t$ ) as well as viscous ( $\lambda_v$ ). To illustrate the diffusivity across different spatial scales, a modified image (from Nicholson *et al.*, 2001) (Figure 34) is shown below.

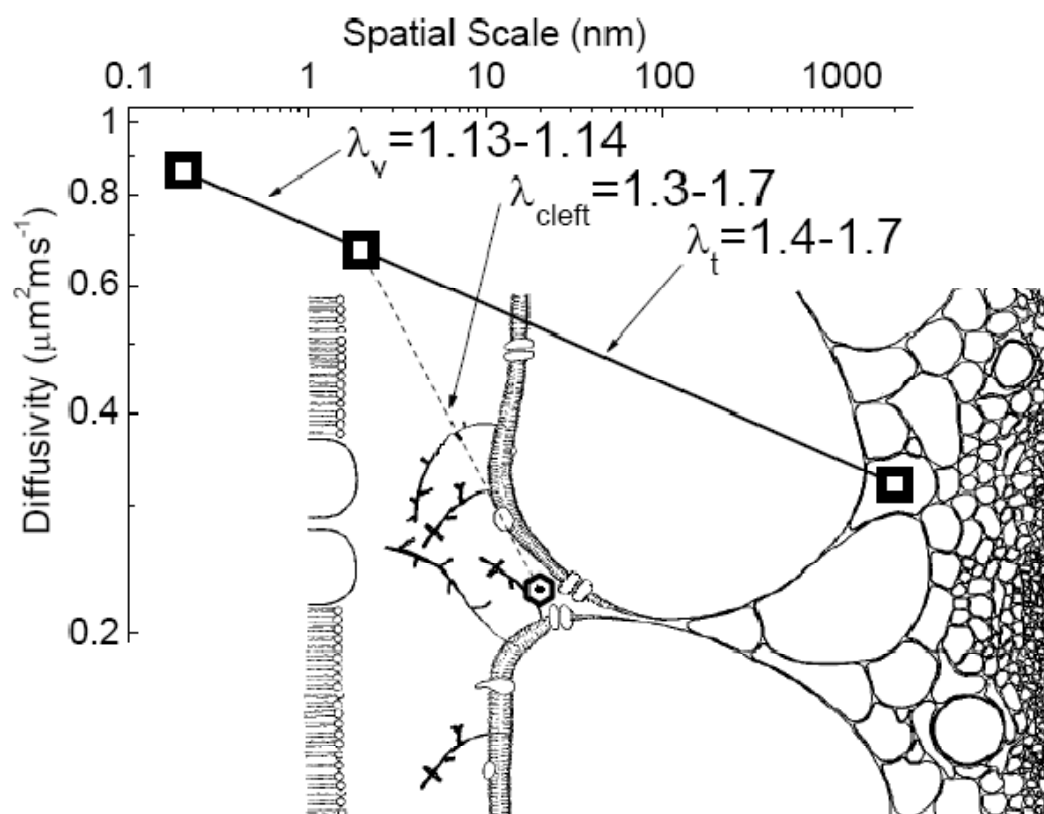


**Figure 34 Scales of Diffusion of Glutamate (modified from Nicholson *et al.*, 2001)**

Glutamate diffusion coefficients (ordinate, log scale) at different spatial scales (abscissa, log scale); Image illustration show brain extracellular space in logarithmic scale; Black squares are  $D_{ACSF}$ ,  $D_{micro}$ ,  $D_{macro}$ , respectively; Black dotted hexagon is  $D_{cleft}$ ;  $\lambda$  values are as indicated with arrows.

### ***Immediate physiological implications of diffusion retardation on nanoscopic levels***

The most apparent effect of the increase in medium viscosity is the decrease in medium conductivity (Walden's rule), although the relationship is not necessarily always linear when one considers larger sized non-electrolyte

(Dagdug *et al.*, 2003). The equivalent electrical resistance of ACSF measured in a free medium at 35°C is ~59 Ohm·cm (Savtchenko & Rusakov, 2007). The present data suggest that this value in the brain extracellular space should be 70-75 Ohm·cm, which is an important determinant of electric fields during excitatory activity (Sylantsev *et al.*, 2008).

A more disguised effect of the increased medium viscosity is the effect on protein movements and interactions in the medium. Instantaneous extracellular diffusivity could affect rapid movements of protein domains during receptor activation and/or ion channel opening (Noskov *et al.*, 2004); in the squid giant axon, a 30-40% increase in the medium micro-viscosity slows down the gating time of sodium channels by more than two-fold (Kukita, 2000). Binding and unbinding of proteins could also be hindered in ion channel and agonist interactions (Blaustein & Finkelstein, 1990).

It is also clear that viscosity changes may have quantitative effects on channel conductance and kinetics. This has been explored with heavy water substitution in squid giant axons (Conti & Palmieri, 1968) and crayfish giant axon (Rayner *et al.*, 1992). In order to get a more precise handle on the exact measures on the effects of micro-viscosity in slices, similar experiments will have to be carried out *in vivo* or *ex vivo*, which has not yet been done to the best of my knowledge. Best generic method of retardation of solution in this case is heavy water substitution of normal water as solvent. At 21°C the viscosity of heavy water is approximately 25% higher than that of water. This is ideal for possible experimentation, as the viscosity change is almost the same as we measured in slices. But there are serious biomolecular problems with such substitution. With increase hydrogen bonding strength in heavy water molecules, many cellular processes will be altered or cease to happen all together. In live animals, such as mice and rat, a 50% substitution of body water will kill the animals. With no immediate possibility of experimental procedures to verify our postulates with regards to effects of viscosity changes, we turned to biophysical models. Preliminary simulation in 3D Monte-Carlo model (results not shown here) and NEURON models (personal communications with Leonid Savtchenko) shows that changes in medium

viscosity has profound effect on resting membrane potential distribution in cells; and changes in the glutamate diffusivity in the extracellular milieu, as oppose to the assumption that it is the same as in the free medium (Barbour & Hauser, 1997), could nearly double the binding probabilities of high-affinity extrasynaptic receptors such as NMDARs and mGluRs whether extrasynaptic transporters are present or not (data not shown here).

Such phenomena impinge on basic mechanisms that shape the action potential waveform, also suggesting that the effects of increased microviscosity should be taken into account when extrapolating receptor/channel activation kinetics assessed *in vitro* onto the conditions *in vivo*. Although the exact mechanisms that contribute to instantaneous diffusion retardation in the extracellular space are difficult to identify, they are likely to involve flexible fragments of numerous freely moving and/or partly restricted macromolecules.

If this is the likely cause of the apparent viscosity change in extracellular space, intracellularly with much crowded environment than extracellular milieu, one would expect a higher increase in viscosity. This would put questions on many models of intracellular channels, gap junctions and protein reactions, where their conductance, gating or reaction kinetics would be affected in similar ways as described earlier within the extracellular space. With the TRFAIM method developed here, it should be a simple transfer from extracellular measurements to intracellular measurements. We propose future projects where we can simultaneously measure extra- and intra-cellular viscosity based on rotational diffusivity principles described in this thesis. This could potentially allow us to examine diffusion changes during physiological stimulations and pathological conditions such as epilepsy. Also restricted diffusion processes in intracellular spaces such as spine neck, where ion diffusion maybe critical to buffering processes hence long term signal transduction, could be measured down to the spatial scale smaller than the actual spine structures. This could not be done easily with the current two photon FRAP method, where the photobleaching spot is larger than the actual spine neck.

Conceivably the TRFAIM method could also be implemented into fibre optical mode with multimode optical fibres and wide field imaging at the fibre tip for use in clinical situations to measure diffusivity in situ. Current fibre optical technology already allows diffusive optical imaging for detecting tumours cells in brain using differences in light scattering properties of cells.

### ***Role of transporters at the vicinity of a single synapse***

On the microscopic scale of a single synapse and its immediate vicinity, our detailed Monte Carlo simulation of the three-dimensional synaptic environment (CHAPTER 6) suggest that the number or distribution of extra-synaptic glutamate transporters on glial membranes has little effect on rapid activation of intra-synaptic receptors by glutamate released at the immediate synapse (Figure 26, Figure 27, Figure 28). This may be counterintuitive to some common transporter blocking experiments showing increase in synaptic responses (Mennerick & Zorumski, 1995), however other have shown that such blocking has no or little effect on EPSCs (Digregorio *et al.*, 2002). In the case of high frequency repetitive stimulation (Figure 28) even at 200Hz, the presence of glial transporters seems to make little difference to EPSCs. It has to be stressed that, we are only testing effect of transporters on an isolated synapse where there is no spill-over at all, which is different to TBOA experiments. In the TBOA experiments, all transporters are blocked, so there are significant spill-over from all neighbouring synapses. As shown in Figure 32 and Figure 33, if large volume of transporter are blocked and a pool of synapses are firing even at low frequency, the glutamate quickly spill-over to neighbouring synapses. This will certainly increase fast synaptic responses if there are high affinity NMDARs present (Figure 31).

However, while extrasynaptic transporters have little control over intra-synaptic events, when transporters are in the close proximity of receptors (inside or outside the synapse), they compete successfully for glutamate molecules leading to much more potent reduction in local receptor activation, whether it is the only a few dozen of transporter expressed inside

the synaptic cleft attenuating the activation of synaptic AMPARs (Figure 29) or suppression of extrasynaptic NMDARs activation by the extrasynaptic transporters (Figure 31). Transporters occurring within the cleft (i.e., those of neuronal type) could influence immediate synaptic responses as shown previously (Bergles & Jahr, 1999; Auger & Atwell, 2000; Diamond, 2001). However, as experiments showed, neither miniature nor minimal-stimulation induced (unitary) AMPAR-mediated EPSCs in CA1 pyramidal cells are affected by glutamate transporter blockade (Figure 30). This result, consistent with the finding that AMPAR synaptic signalling is insensitive to glutamate transporter blockade at synapses in barrel cortex and neocortex (Campbell & Hablitz, 2004; Bannister *et al.*, 2005), suggests that the number of glutamate transporters expressed within synaptic clefts may be insignificant or at least majority are being heavily downregulated by intracellular proteins such as GTRAP3-18 (Lin *et al.*, 2001). Since having transporters localised near high affinity receptors could reduce receptors' binding probabilities (Figure 31) hence opening probabilities, it maybe plausible that high affinity mGluRs which already have heavy protein interactions intracellularly and co-occupy similar perisynaptic regions as neuronal transporters could have protein pathways that interact with presynaptic neuronal transporters to regulate their roles in shielding high affinity receptors from spill-overs (Brasnjo & Otis, 2001).

Outside the cleft, activation of extrasynaptic NMDARs is substantially reduced if they share their spatial domain with glial glutamate transporters but could be significantly activated if no transporters are expressed nearby (Figure 31B). It should be noted that this observed effect could apply to any high affinity receptors apart from NMDARs (such as mGluRs), whereas the effect disappears for low affinity receptors such as AMPARs. This reinforces the idea that the role played by the extrasynaptic transporters on a fast temporal scale is to shield, not only the high affinity intrasynaptic receptors from spill-overs but also extrasynaptic high affinity receptors from glutamate waves. The present simulations also predict a somewhat higher level of activation for the high affinity NMDARs occurring in the transporter vicinity than simulation results reported previously in comparable conditions (Lehre & Rusakov 2002; Franks *et al.*, 2002; Rusakov & Kullmann, 1998a). One possible explanation is

that NMDARs in the present model are separated from nearby transporters by at least a 20 nm inter-cellular gap, to reflect the apposing neuronal and glial membranes. Therefore, receptors and transporters do not share the same volume compartment or the same membrane domain in our experiments, which is the case in most previous models. It also brought to our attention that only a full 3D (either Monte-Carlo or compartmental) model will produce correct results. By reducing the diffusible space from 3D to 2D when intermembrane gap is ignored or effectively reduced near to zero, has resulted in increasing the binding probability and hence exaggerated the dependency on extrasynaptic transporters. This suggests that the extracellular space fraction also plays a role in the effectiveness of transporters. With increasing extracellular space fractions, brings higher opening probability of high affinity receptors both intrasynaptic and extrasynaptic. This suggests that in younger animals, which generally have higher extracellular space fractions, together with immature synapses that have low transporter density near the synapse, are more susceptible to spill-over effects, hence more prone to epileptic seizures. Furthermore, glutamate transporters in the present approach are accumulated within a restricted area (representing a fragment of the glial membrane), in accordance with experimental observations, rather than distributed homogeneously at a lower density as implemented in previous models. This facilitates the chances for diffusing glutamate molecules to encounter an NMDAR before being bound to a transporter molecule. Our observations suggest that juxtaposition of receptors and transporters has a complex effect on receptor activation, which could be masked in assessments that utilize volume-average quantities.

These results provide mechanistic insights into the experimental observations indicating that glial transporters affect activation of predominantly high affinity extra-synaptic receptors (Brasnjo & Otis, 2001; Arnth-Jensen *et al.*, 2002), and also provide a quantitative reference for evaluating the extent of extra- and/or inter-synaptic signalling in the hippocampus, an issue remaining a subject of debates (Scimemi *et al.*, 2004; Franks *et al.*, 2002).

### ***Transporters' role in ambient glutamate concentration control***

On the macroscopic scale, we evaluated factors shaping the profile of ambient extracellular glutamate concentration. We focused on the synaptic neuropil of the CA1 area in the hippocampus, a subject of intense physiological studies. Simple kinetic calculations based on the available experimental data suggest that excitatory glutamatergic synapses in this area operate with a high safety factor (20-50) in terms of glutamate removal.

We found that the spatial 'landscape' of extracellular glutamate is determined overwhelmingly by the distribution of available transporters. Whilst the sustained synaptic activity is likely to produce local (1-2  $\mu\text{m}$  range), relatively small (1-2  $\mu\text{M}$ ) increases in the background glutamate concentration, the long-range concentration gradients are likely to rely on variation in the density of functional transporters (Figure 32, Figure 33). Again, these results provide a biophysical basis for the observation that activation of extra-synaptic glutamate receptors could be dramatically reduced in areas where the density of transporters is high (Wadiche & Jahr, 2005). Similarly, cell-specific differences in the ambient receptor activation (Semyanov *et al.*, 2004; Cavalier *et al.*, 2005) are likely to reflect the underlying differences in the local transporter densities. The finding that relates the withdrawal of transporter-enriched glial processes to a dramatic increase in long-range actions of synaptically released glutamate in the hypothalamic supraoptic nucleus provides a striking demonstration of this principle (Oliet *et al.*, 2001).

Intriguingly, individual astrocyte that are responsible for the bulk of glutamate uptake in the hippocampus (Danbolt, 2001), occupy separate neuropil domains that extend over  $\sim 9 \times 10^4 \mu\text{m}^3$  while overlapping by 3-5% only with neighbouring astrocytes in mouse models (Ogata & Kosaka, 2002). This suggests that dysfunction of a single astrocyte could impair glutamate removal within a pool of  $\sim 1.8 \times 10^5$  synapses. Figure 33 provides a quantitative illustration to this situation: a dramatic increase in the ambient glutamate level occurs within the domain of the dysfunctional astrocyte where only 1% of transporters are present. Because an individual CA1 pyramidal cell hosts  $5-10 \times 10^3$  synapses (Trommald *et al.*, 1995), such impairment may affect synaptic

inputs to hundreds of principal cells. This relationship underlies the importance of individual glial cells in maintaining synapse-specific excitatory signalling in the hippocampus. Furthermore, astrocytes are extensively coupled via highly conductive gap junctions which allow  $\text{Ca}^{2+}$  and  $\text{IP}_3$  to pass freely. The collapse of a single astrocyte could easily cause secondary failures in neighbouring astrocytes (Cotrina *et al.*, 1998). With spreading of astrocyte failures would mean increase in ambient glutamate levels in a spreading wave fashion. Combination of this effect and with higher macroscopic extracellular diffusivity due to geometrically less tortuous extracellular space in younger animals, the spread of glutamate to neurotoxic levels will be significantly faster in younger animals. Together with higher extracellular space fraction in younger animals, hence high susceptibility to high affinity receptor activations. One can easily see the high probability of younger animals having epileptic seizures.

# Bibliography

- Anderson, S. R. "TIME-RESOLVED FLUORESCENCE SPECTROSCOPY - APPLICATIONS TO CALMODULIN." *The Journal of Biological Chemistry* 266 (1991): 11405-11408.
- Arnth-Jensen, Nina, Denis Jabaudon, and Massimo Scanziani. "Cooperation between independent hippocampal synapses is controlled by glutamate uptake." *Nat Neurosci* 5 (2002): 325-331.
- Asztely, F., G. Erdemli, and D. M. Kullmann. "Extrasynaptic glutamate spillover in the hippocampus: dependence on temperature and the role of active glutamate uptake." *Neuron* 18 (1997): 281-293.
- Auger, Celine, and David Attwell. "Fast Removal of Synaptic Glutamate by Postsynaptic Transporters." *Neuron* 28 (2000): 547-558.
- Bahh, B. El, V. Lespinet, D. Lurton, M. Coussemacq, G. Le Gal, and A. Rougier. "Correlations between granule cell dispersion, mossy fiber sprouting, and hippocampal cell loss in temporal lobe epilepsy." *Epilepsia* 40 (1999): 1393-1401.
- Banke, T. G., D. Bowie, H. Lee, R. L. Huganir, A. Schousboe, and S. F. Traynelis. "Control of GluR1 AMPA receptor function by cAMP-dependent protein kinase." *J Neurosci* 20 (2000): 89-102.
- Bannister, Neil J, et al. "Developmental changes in AMPA and kainate receptor-mediated quantal transmission at thalamocortical synapses in the barrel cortex." *J Neurosci* 25 (2005): 5259-5271.
- Barbour, B. "An Evaluation of Synapse Independence." *The Journal of Neuroscience* 20 (2001): 7969-7984.
- Barbour, B., and Michael Hausser. "Intersynaptic diffusion of neurotransmitter." *Trends Neurosci* 20 (1997): 377-384.
- Bayer, T. A., O. D. Wiestler, and H. K. Wolf. "Hippocampal loss of N-methyl-D-aspartate receptor subunit 1 mRNA in chronic temporal lobe epilepsy." *Acta Neuropathol* 89 (1995): 446-450.
- Bergles, D. E., and C. E. Jahr. "Glial contribution to glutamate uptake at Schaffer collateral-commissural synapses in the hippocampus." *J Neurosci* 18 (1998): 7709-16.
- Bhalla, Upinder S. "Signaling in small subcellular volumes. II. Stochastic and diffusion effects on synaptic network properties." *Biophys J* 87 (2004): 745-753.
- Bihl, Rachid Id, John G R, and Martin Vreugdenhil. "The role of extracellular potassium in the epileptogenic transformation of recurrent GABAergic inhibition." *Epilepsia* 46 Suppl 5 (2005): 64-71.
- Blaustein, R. O., and A. Finkelstein. "Diffusion limitation in the block by symmetric tetraalkylammonium ions of anthrax toxin channels in planar phospholipid bilayer membranes." *J Gen Physiol* 96 (1990): 943-957.
- Bouvier, M., M. Szatkowski, A. Amato, and D. Attwell. "The glial cell glutamate uptake carrier countertransports pH-changing anions." *Nature* 360 (1992): 471-474.
- Bozzali, Marco, and Andrea Cherubini. "Diffusion tensor MRI to investigate dementias: a brief review." *Magn Reson Imaging* 25 (2007): 969-977.
- Braeckmans, K., K. Remaut, R. E. Vandenbroucke, B. Lucas, S. C. De, and J. Demeester. "Line FRAP with the confocal laser scanning microscope for diffusion measurements in small regions of 3-D samples." *Biophys J* 92 (2007): 2172-83.
- Brasnjo, G., and T. S. Otis. "Neuronal glutamate transporters control activation of postsynaptic metabotropic glutamate receptors and influence cerebellar long-term depression." *Neuron* 31 (2001): 607-16.
- Cajal, Santiago Ramon. "The structure and connexions of neurons." 1906.

- Campbell, S. L., and J. J. Hablitz. "Glutamate transporters regulate excitability in local networks in rat neocortex." *Neuroscience* 127 (2004): 625-635.
- Carroll, R. C., E. C. Beattie, M. von Zastrow, and R. C. Malenka. "Role of AMPA receptor endocytosis in synaptic plasticity." *Nat Rev Neurosci* 2 (2001): 315-324.
- Cavelier, Pauline, Martine Hamann, David Rossi, Peter Mobbs, and David Attwell. "Tonic excitation and inhibition of neurons: ambient transmitter sources and computational consequences." *Prog Biophys Mol Biol* 87 (2005): 3-16.
- Chaudhry, F. A., K. P. Lehre, M. van Lookeren, O. P. Ottersen, N. C. Danbolt, and J. Storm-Mathisen. "Glutamate transporters in glial plasma membranes: highly differentiated localizations revealed by quantitative ultrastructural immunocytochemistry." *Neuron* 15 (1995): 711-720.
- Chen, K. C., and C. Nicholson. "Changes in brain cell shape create residual extracellular space volume and explain tortuosity behavior during osmotic challenge." *Proc Natl Acad Sci U S A* 97 (2000): 8306-11.
- Chen, Tong-Sheng, Shao-Qun Zeng, Wei Zhou, and Qing-Ming Luo. "A Quantitative Theory Model of a Photobleaching Mechanism." *Chin. Phys. Lett.* 20 (2003): 1940-1943.
- Choquet, Daniel, and Antoine Triller. "The role of receptor diffusion in the organization of the postsynaptic membrane." *Nature Reviews* 4 (2003): 252-265.
- Clements, J. D. "Transmitter timecourse in the synaptic cleft its role in central synaptic function." *Trends Neurosci* 19 (1996): 163-71.
- Cohen, L. B., B. Hille, and R. D. Keynes. "Changes in axon birefringence during the action potential." *J Physiol* 211 (1970): 495-515.
- Cohen, L. B., R. D. Keynes, and B. Hille. "Light scattering and birefringence changes during nerve activity." *Nature* 218 (1968): 438-441.
- Conti, F., and G. Palmieri. "Nerve fiber behaviour in heavy water under voltage-clamp." *Biophysik* 5 (1968): 71-77.
- Dagdug, L., Berezhkovskii, A., S.M. Bezrukov, and G.H. Weiss. "Diffusion-controlled reactions with a binding site hidden in a channel." *Journal of Chemical Physics* 118 (2003): 2367-2373.
- Dale, Sir Henry. "Some recent extensions of the chemical transmission of the effects of nerve impulses." 1935.
- Danbolt, N. C. "Glutamate uptake." *Prog Neurobiol* 65 (2001): 1-105.
- Davis, S. K., and C. J. Bardeen. "Using two-photon standing waves and patterned photobleaching to measure diffusion from nanometers to microns in biological systems." *REVIEW OF SCIENTIFIC INSTRUMENTS* 73 (2002): 2128-2135.
- DE, E. D., and H. S. BENNETT. "Some features of the submicroscopic morphology of synapses in frog and earthworm." *J Biophys Biochem Cytol* 1 (1955): 47-58.
- Deb, Kalyanmoy, Amrit Pratap, Sameer Agarwal, and T. Meyarivan. "A Fast and Elitist Multiobjective Genetic Algorithm NSGA-II." *IEEE TRANSACTIONS ON EVOLUTIONARY COMPUTATION* 6 (2002): 182-197.
- Demarque, Michael, et al. "Glutamate transporters prevent the generation of seizures in the developing rat neocortex." *J Neurosci* 24 (2004): 3289-3294.
- Derkach, V., A. Barria, and T. R. Soderling. "Ca<sup>2+</sup>/calmodulin-kinase II enhances channel conductance of alpha-amino-3-hydroxy-5-methyl-4-isoxazolepropionate type glutamate receptors." *Proc Natl Acad Sci U S A* 96 (1999): 3269-3274.
- Diamond, J. S., and C. E. Jahr. "Transporters buffer synaptically released glutamate on a submillisecond time scale." *J Neurosci* 17 (1997): 4672-87.
- Diamond, Jeffrey S. "A broad view of glutamate spillover." *Nature Neuroscience* 5 (2002): 291-292.
- Diamond, Jeffrey S. "Neuronal Glutamate Transporters Limit Activation of NMDA Receptors by Neurotransmitter Spillover on CA1 Pyramidal Cells." *The Journal of Neuroscience* 21 (2001): 8328-8338.

- Diehl, B., et al. "Postictal diffusion-weighted imaging for the localization of focal epileptic areas in temporal lobe epilepsy." *Epilepsia* 42 (2001): 21-28.
- DiGregorio, David A, Jason S Rothman, Thomas A Nielsen, and R. Angus Silver. "Desensitization properties of AMPA receptors at the cerebellar mossy fiber granule cell synapse." *J Neurosci* 27 (2007): 8344-8357.
- DiGregorio, David A, Zoltan Nusser, and R. Angus Silver. "Spillover of glutamate onto synaptic AMPA receptors enhances fast transmission at a cerebellar synapse." *Neuron* 35 (2002): 521-533.
- Dijkhuizen, Rick M, and Klaas Nicolay. "Magnetic resonance imaging in experimental models of brain disorders." *J Cereb Blood Flow Metab* 23 (2003): 1383-1402.
- Dobrunz, L. E., and C. F. Stevens. "Heterogeneity of release probability, facilitation, and depletion at central synapses." *Neuron* 18 (1997): 995-1008.
- Dong, Chen-Yuan, Karsten Koenig, and Peter So. "Characterizing point spread functions of two-photon fluorescence microscopy in turbid medium." *J Biomed Opt* 8 (2003): 450-459.
- Duong, T. Q., J. J. Ackerman, H. S. Ying, and J. J. Neil. "Evaluation of extra- and intracellular apparent diffusion in normal and globally ischemic rat brain via 19F NMR." *Magn Reson Med* 40 (1998): 1-13.
- Dyson, F. "A meeting with Enrico Fermi." *Nature* 247 (2004): 6972.
- Eccles, J. C. "The synapse: from electrical to chemical transmission." *Annu Rev Neurosci* 5 (1982): 325-339.
- Eghbali, M., J. P. Curmi, B. Birnir, and P. W. Gage. "Hippocampal GABA(A) channel conductance increased by diazepam." *Nature* 388 (1997): 71-75.
- Eid, Tore, Anne Williamson, Tih-Shih W Lee, Ognen A Petroff, and Nihal C de. "Glutamate and astrocytes--key players in human mesial temporal lobe epilepsy?" *Epilepsia* 49 Suppl 2 (2008): 42-52.
- Elson, Dan, et al. "Time-domain fluorescence lifetime imaging applied to biological tissue." *Photochem. Photobiol. Sci.* 3 (2004): 795-801.
- Ercińska, M., and I. A. Silver. "Metabolism and role of glutamate in mammalian brain." *Prog Neurobiol* 35 (1990): 245-296.
- et, D. A. "Accurate measurements of the viscosity of water in the temperature range 19.5–25.5°C." *Physica A: Statistical and Theoretical Physics* 151 (1988): 246-280.
- Fabene, P. F., P. Marzola, A. Sbarbati, and M. Bentivoglio. "Magnetic resonance imaging of changes elicited by status epilepticus in the rat brain: diffusion-weighted and T2-weighted images, regional blood volume maps, and direct correlation with tissue and cell damage." *Neuroimage* 18 (2003): 375-389.
- Fisher, R. S., T. A. Pedley, W. J. Moody, and D. A. Prince. "The role of extracellular potassium in hippocampal epilepsy." *Arch Neurol* 33 (1976): 76-83.
- Franks, Kevin M., Jr. Bartol, Thomas, and Terrence J. Sejnowski. "A Monte Carlo Model Reveals Independent Signalling at Central Glutamatergic Synapses." *Biophysical Journal* 83 (2002): 2333-2348.
- Furuta, A., J. D. Rothstein, and L. J. Martin. "Glutamate transporter protein subtypes are expressed differentially during rat CNS development." *J Neurosci* 17 (1997): 8363-8375.
- GARTHWAITE, G, GD WILLIAMS, and J GARTHWAITE. "GLUTAMATE TOXICITY AN EXPERIMENTAL AND THEORETICAL ANALYSIS." *EUROPEAN JOURNAL OF NEUROSCIENCE* 4 (1992): 353-360.
- Geinisman, Y., L. de Toledo-Morrell, F. Morrell, I. S. Persina, and M. Rossi. "Structural synaptic plasticity associated with the induction of long-term potentiation is preserved in the dentate gyrus of aged rats." *Hippocampus* 2 (1992): 445-456.
- Golgi, Camillo. "The neuron doctrine - theory and facts." 1906.
- Gorter, Jan A, Pedro M Gonçalves, Erwin A van, Eleonora Aronica, Fernando H Lopes, and Paul J Lucassen. "Neuronal cell death in a rat model for mesial temporal lobe epilepsy is

- induced by the initial status epilepticus and not by later repeated spontaneous seizures." *Epilepsia* 44 (2003): 647-658.
- Hakyemez, Bahattin, Cuneyt Erdogan, Harun Yildiz, Ilker Ercan, and Mufit Parlak. "Apparent diffusion coefficient measurements in the hippocampus and amygdala of patients with temporal lobe seizures and in healthy volunteers." *Epilepsy Behav* 6 (2005): 250-256.
- Harrevelde, A. Van, N. Dafny, and F. I. Khattab. "Effects of calcium on the electrical resistance and the extracellular space of cerebral cortex." *Exp Neurol* 31 (1971): 358-367.
- Harris, K. M., and P. Sultan. "Variation in the number, location and size of synaptic vesicles provides an anatomical basis for the nonuniform probability of release at hippocampal CA1 synapses." *Neuropharmacology* 34 (1995): 1387-1395.
- Harris, K. M., F. E. Jensen, and B. Tsao. "Three-dimensional structure of dendritic spines and synapses in rat hippocampus (CA1) at postnatal day 15 and adult ages: implications for the maturation of synaptic physiology and long-term potentiation." *J Neurosci* 12 (1992): 2685-2705.
- Harris, N. G., G. Zilkha, J. Houseman, M. R. Symms, T. P. Obrenovitch, and S. R. Williams. "The relationship between the apparent diffusion coefficient measured by magnetic resonance imaging, anoxic depolarization, and glutamate efflux during experimental cerebral ischemia." *JOURNAL OF CEREBRAL BLOOD FLOW AND METABOLISM* 20 (2000): 28-36.
- He, Yong, William G. M., J. D. Rothstein, and John H. Morrison. "Differential Synaptic Localization of the Glutamate Transporter EAAC1 and Glutamate Receptor Subunit GluR2 in the Rat Hippocampus." *The Journal of Comparative Neurology* 418 (2000): 255-269.
- Heinemann, U., A. Konnerth, R. Pumain, and W. J. Wadman. "Extracellular calcium and potassium concentration changes in chronic epileptic brain tissue." *Adv Neurol* 44 (1986): 641-661.
- Heiniger, P., et al. "Diffusion and perfusion MRI for the localisation of epileptogenic foci in drug-resistant epilepsy." *Neuroradiology* 44 (2002): 475-480.
- Herman, Melissa A, and Craig E Jahr. "Extracellular glutamate concentration in hippocampal slice." *J Neurosci* 27 (2007): 9736-9741.
- Holmes, W. R. "Modeling the effect of glutamate diffusion and uptake on NMDA and non-NMDA receptor saturation." *BIOPHYSICAL JOURNAL* 69 (1995): 1734-1747.
- Holz, Manfred, R. Heil Stefan, and Sacco Antonio. "Temperature-dependent self-diffusion coefficients of water and six selected molecular liquids for calibration in accurate 1H NMR PFG measurements." *Phys. Chem. Chem. Phys.* 2 (2000): 4740-4742.
- Homola, A., N. Zoremba, K. Slais, R. Kuhlen, and E. Sykova. "Changes in diffusion parameters, energy-related metabolites and glutamate in the rat cortex after transient hypoxia ischemia." *NEUROSCIENCE LETTERS* 404 (2006): 137-142.
- Hrabe, J., S. Hrabetova, and K. Segeth. "A model of effective diffusion and tortuosity in the extracellular space of the brain." *BIOPHYSICAL JOURNAL* 87 (2004): 1606-1617.
- Hrabetova, S. "Extracellular Diffusion Is Fast and Isotropic in the Stratum Radiatum of Hippocampal CA1 Region in Rat Brain Slices." *HIPPOCAMPUS* 15 (2005): 441-450.
- Hrabetova, S., J. Hrabe, and C. Nicholson. "Dead-space microdomains hinder extracellular diffusion in rat neocortex during ischemia." *J Neurosci* 23 (2003): 8351-9.
- Hufnagel, Andreas, et al. "Brain diffusion after single seizures." *Epilepsia* 44 (2003): 54-63.
- Jin, Rongsheng, Tue G Banke, Mark L Mayer, Stephen F Traynelis, and Eric Gouaux. "Structural basis for partial agonist action at ionotropic glutamate receptors." *Nat Neurosci* 6 (2003): 803-810.
- Jonas, P., G. Major, and B. Sakmann. "Quantal components of unitary EPSCs at the mossy fibre synapse on CA3 pyramidal cells of rat hippocampus." *J Physiol* 472 (1993): 615-663.
- Jones, M. V., and G. L. Westbrook. "The impact of receptor desensitization on fast synaptic transmission." *Trends Neurosci* 19 (1996): 96-101.

- Kandel, Jessell TM. *Principles of Neural Science*. McGraw-Hill, 2000.
- Kimiwada, Tomomi, et al. "Hippocampal and thalamic diffusion abnormalities in children with temporal lobe epilepsy." *Epilepsia* 47 (2006): 167-175.
- Kirkby, D. R., and D. T. Delpy. "Measurement of tissue temporal point spread function (TPSF) by use of a gain-modulated avalanche photodiode detector." *PHYSICS IN MEDICINE AND BIOLOGY* 41 (1996): 939-949.
- Korf, J., H. C. Klein, K. Venema, and F. Postema. "Increases in striatal and hippocampal impedance and extracellular levels of amino acids by cardiac arrest in freely moving rats." *J Neurochem* 50 (1988): 1087-1096.
- Krizaj, D, ME Rice, RA Wardle, and C Nicholson. "Water compartmentalization and extracellular tortuosity after osmotic changes in cerebellum of *Trachemys scripta*." *JOURNAL OF PHYSIOLOGY-LONDON* 492 (1996): 887-896.
- Kuffler, Stephen W. "Further study on transmission in an isolated nerve-muscle fibre preparation." *J Neurophysiol* 5 (1942): 309-322.
- Kukita, F. "Solvent effects on squid sodium channels are attributable to movements of a flexible protein structure in gating currents and to hydration in a pore." *J Physiol* 522 Pt 3 (2000): 357-373.
- Kullmann, D. M. "Synaptic and extrasynaptic roles of glutamate in the mammalian hippocampus." *Acta Physiol Scand* 166 (1999): 79-83.
- Kullmann, Dimitri M. "The neuronal channelopathies." *Brain* 125 (2002): 1177-1195.
- Kume-Kick, J., T. Mazel, I. Vorisek, S. Hrabetova, L. Tao, and C. Nicholson. "Independence of extracellular tortuosity and volume fraction during osmotic challenge in rat neocortex." *J Physiol* 542 (2002): 515-27.
- L, Timothy P, and Howard A Rowley. "Diffusion weighted magnetic resonance imaging in stroke." *Eur J Radiol* 45 (2003): 185-194.
- Lakowicz. *The Principle of fluorescent imaging*. 2006.
- Lee, S. H., S. Magge, D. D. Spencer, H. Sontheimer, and A. H. Cornell-Bell. "Human epileptic astrocytes exhibit increased gap junction coupling." *Glia* 15 (1995): 195-202.
- Lehre, K. P., L. M. Levy, O. P. Ottersen, J. Storm-Mathisen, and N. C. Danbolt. "Differential expression of two glial glutamate transporters in the rat brain: quantitative and immunocytochemical observations." *J Neurosci* 15 (1995): 1835-1853.
- Lehre, Knut Petter, and Dmitri Rusakov. "Asymmetry of Glia near Central Synapses Favours Presynaptically Directed Glutamate Escape." *Biophysical Journal* 83 (2002): 125-134.
- Lehre, Knut Petter, and Niels C. Danbolt. "The Number of Glutamate Transporter Subtype Molecules at Glutamatergic Synapses Chemical and Stereological Quantification in Young Adult Rat Brain." *The Journal of Neuroscience* 18 (1998): 8751-8757.
- Liang. "Neurocomputation by Reaction Diffusion." *Phys Rev Lett* 75 (1995): 1863-1866.
- Lin, C. I., et al. "Modulation of the neuronal glutamate transporter EAAC1 by the interacting protein GTRAP3-18." *Nature* 410 (2001): 84-88.
- Longworth, L. G. "Diffusion measurements at 25° of aqueous solutions of amino acids, peptides and sugars." *Journal of American Chemical Society* 75 (1953): 5705-5709.
- Lubkin, S. R., and X. Wan. "Optimizing detection of tissue anisotropy by fluorescence recovery after photobleaching." *Bull Math Biol* 68 (2006): 1873-1891.
- Magde, Douglas, Elliot Elson, and W. W. Webb. "Thermodynamic Fluctuations in a Reacting System -- Measurement by Fluorescence Correlation Spectroscopy." *Physical Review Letters* 29 (1972): 705-708.
- Matsuoka, Y., and K. A. Hossmann. "Cortical impedance and extracellular volume changes following middle cerebral artery occlusion in cats." *J Cereb Blood Flow Metab* 2 (1982): 466-474.
- Mazza, Davide, et al. "A New FRAP/FRAPa Method For 3-D Diffusion Measurements Based On Multi-photon Excitation Microscopy." *Biophys J*, 2008.

- McBain, C. J., and M. L. Mayer. "N-Methyl-D-Aspartic Acid Receptor Structure and Function." *Physiological Reviews* 74 (1994): 723-760.
- McBain, C. J., S. F. Traynelis, and R. Dingledine. "Regional variation of extracellular space in the hippocampus." *Science* 249 (1990): 674-677.
- Meisler, Miriam H, and Jennifer A Kearney. "Sodium channel mutations in epilepsy and other neurological disorders." *J Clin Invest* 115 (2005): 2010-2017.
- Mennerick, S., and C. F. Zorumski. "Presynaptic influence on the time course of fast excitatory synaptic currents in cultured hippocampal cells." *J Neurosci* 15 (1995): 3178-3192.
- Mennerick, S., et al. "Neuronal expression of the glutamate transporter GLT-1 in hippocampal microcultures." *J Neurosci* 18 (1998): 4490-9.
- Mikuni, N., T. L. Babb, and W. Christi. "Increased NR1-NR2A/B coassembly as a mechanism for rat chronic hippocampal epilepsy." *Neurosci Lett* 267 (1999): 165-168.
- Nicholson, C. "Diffusion and related transport mechanisms in brain tissue." *REPORTS ON PROGRESS IN PHYSICS* 64 (2001): 815-884.
- Nicholson, C., and E. Sykova. "Extracellular space structure revealed by diffusion analysis." *Trends Neurosci* 21 (1998): 207-15.
- Nicholson, C., and J. M. Phillips. "Diffusion of anions and cations in the extracellular microenvironment of the brain." *J Physiol* 296 (1979): 66P.
- Nicholson, C., and J. M. Phillips. "Ion diffusion modified by tortuosity and volume fraction in the extracellular microenvironment of the rat cerebellum." *J Physiol* 321 (1981): 225-257.
- Nicholson, C., and M. E. Rice. "Calcium diffusion in the brain cell microenvironment." *Can J Physiol Pharmacol* 65 (1987): 1086-1091.
- Nicholson, C., and M. E. Rice. "The migration of substances in the neuronal microenvironment." *Ann N Y Acad Sci* 481 (1986): 55-71.
- Nielsen, T. A., D. A. DiGregorio, and R. A. Silver. "Modulation of glutamate mobility reveals the mechanism underlying slow-rising AMPAR EPSCs and the diffusion coefficient in the synaptic cleft." *NEURON* 42 (2004): 757-771.
- Norris, D. G. "The effects of microscopic tissue parameters on the diffusion weighted magnetic resonance imaging experiment." *NMR IN BIOMEDICINE* 14 (2001): 77-93.
- Noskov, Sergei Yu, Simon Bernèche, and Benoît Roux. "Control of ion selectivity in potassium channels by electrostatic and dynamic properties of carbonyl ligands." *Nature* 431 (2004): 830-834.
- Nusser, Zoltan, Rafael Lujan, Gregor Laube, J. David B., Elek Molnar, and Peter Somogyi. "Cell Type and Pathway Dependence of Synaptic AMPA Receptor Number and Variability in the Hippocampus." *Neuron* 21 (1998): 545-559.
- Obrenovitch, T. P. "High extracellular glutamate and neuronal death in neurological disorders Cause contribution or consequence." *Ann N Y Acad Sci* 890 (1999): 273-86.
- Oertner, Thomas G, Bernardo L Sabatini, Esther A Nimchinsky, and Karel Svoboda. "Facilitation at single synapses probed with optical quantal analysis." *Nat Neurosci* 5 (2002): 657-664.
- Ogata, K., and T. Kosaka. "Structural and quantitative analysis of astrocytes in the mouse hippocampus." *Neuroscience* 113 (2002): 221-33.
- Oliet, S. H., R. Piet, and D. A. Poulain. "Control of glutamate clearance and synaptic efficacy by glial coverage of neurons." *Science* 292 (2001): 923-926.
- Otis, T. S., and C. E. Jahr. "Anion currents and predicted glutamate flux through a neuronal glutamate transporter." *J Neurosci* 18 (1998): 7099-110.
- Otis, T. S., Y. C. Wu, and L. O. Trussell. "Delayed clearance of transmitter and the role of glutamate transporters at synapses with multiple release sites." *J Neurosci* 16 (1996): 1634-44.

- Papadopoulos, M. C., D. K. Binder, and A. S. Verkman. "Enhanced macromolecular diffusion in brain extracellular space in mouse models of vasogenic edema measured by cortical surface photobleaching." *FASEB J* 19 (2005): 425-7.
- Partikian, A., B. Olveczky, R. Swaminathan, Y. Li, and A. S. Verkman. "Rapid diffusion of green fluorescent protein in the mitochondrial matrix." *J Cell Biol* 140 (1998): 821-9.
- Pérez-Pinzón, M. A., L. Tao, and C. Nicholson. "Extracellular potassium, volume fraction, and tortuosity in rat hippocampal CA1, CA3, and cortical slices during ischemia." *J Neurophysiol* 74 (1995): 565-573.
- Piet, R., L. Vargova, E. Sykova, D. A. Poulain, and S. H. Oliet. "Physiological contribution of the astrocytic environment of neurons to intersynaptic crosstalk." *Proc Natl Acad Sci U S A* 101 (2004): 2151-5.
- Prybylowski, Kate, et al. "Relationship between availability of NMDA receptor subunits and their expression at the synapse." *J Neurosci* 22 (2002): 8902-8910.
- Qiao, M., K. L. Malisza, M. R. Del, and U. I. Tuor. "Transient hypoxia-ischemia in rats changes in diffusion-sensitive MR imaging findings, extracellular space, and Na<sup>+</sup>-K<sup>+</sup>-adenosine triphosphatase and cytochrome oxidase activity." *Radiology* 223 (2002): 65-75.
- Racca, Claudia, F. Anne Stephenson, Peter Streit, J. David B., and Peter Somogyi. "NMDA Receptor Content of Synapses in Stratum Radiatum of the Hippocampal CA1 Area." *The Journal of Neuroscience* 20 (2000): 2512-2522.
- Raghavachari, Sridhar, and John E. Lisman. "Properties of Quantal Transmission at CA1 Synapses." *Journal of Neurophysiology* 92 (2004): 2456-2467.
- Rayner, M. D., J. G. Starkus, P. C. Ruben, and D. A. Alicata. "Voltage-sensitive and solvent-sensitive processes in ion channel gating. Kinetic effects of hyperosmolar media on activation and deactivation of sodium channels." *Biophys J* 61 (1992): 96-108.
- Rhodes, Thomas H, Carlos G Vanoye, Iori Ohmori, Ikuo Ogiwara, Kazuhiro Yamakawa, and Alfred L George. "Sodium channel dysfunction in intractable childhood epilepsy with generalized tonic-clonic seizures." *J Physiol* 569 (2005): 433-445.
- Rice, M. E., G. A. Gerhardt, P. M. Hierl, G. Nagy, and R. N. Adams. "Diffusion coefficients of neurotransmitters and their metabolites in brain extracellular fluid space." *Neuroscience* 15 (1985): 891-902.
- Roth, Yiftach, et al. "Quantification of water compartmentation in cell suspensions by diffusion-weighted and T(2)-weighted MRI." *Magn Reson Imaging* 26 (2008): 88-102.
- Rothstein, J. D., et al. "Localization of neuronal and glial glutamate transporters." *Neuron* 13 (1994): 713-25.
- Rusakov, D. A., E. Harrison, and M. G. Stewart. "Synapses in hippocampus occupy only 1-2% of cell membranes and are spaced less than half-micron apart: a quantitative ultrastructural analysis with discussion of physiological implications." *Neuropharmacology* 37 (1998): 513-521.
- Rusakov, Dmitri A. "The Role of Perisynaptic Glial Sheaths in Glutamate Spillover and Extracellular Ca<sup>2+</sup> Depletion." *Biophysical Journal* 81 (2001): 1947-1959.
- Rusakov, Dmitri A., and Dimitri M. Kullmann. "Extrasynaptic glutamate Diffusion in the hippocampus Ultrastructure Constraints, Uptake, and Receptor Activation." *The Journal of Neuroscience* 18 (1998): 3158-3170.
- Rusakov, Dmitri A., and Dimitri M. Kullmann. "Geometric and viscous components of the tortuosity of the extracellular space in the brain." *PNAS* 95 (1998): 8975-8980.
- Saftenu, E. E. "Modeling of slow glutamate diffusion and AMPA receptor activation in the cerebellar glomerulus." *JOURNAL OF THEORETICAL BIOLOGY* 234 (2005): 363-382.
- Sah, P., S. Hestrin, and R. A. Nicoll. "Tonic activation of NMDA receptors by ambient glutamate enhances excitability of neurons." *Science* 246 (1989): 815-818.
- Savtchenko, L. P., and D. A. Rusakov. "The optimal height of the synaptic cleft." *PROCEEDINGS OF THE NATIONAL ACADEMY OF SCIENCES OF THE UNITED STATES OF AMERICA* 104 (2007): 1823-1828.

- Savtchenko, L. P., N. Kulahin, S. M. Korogod, and D. A. Rusakov. "Electric fields of synaptic currents could influence diffusion of charged neurotransmitter molecules." *SYNAPSE* 51 (2004): 270-278.
- Savtchenko, L. P., S. M. Korogod, and D. A. Rusakov. "Electrodiffusion of synaptic receptors a mechanism to modify synaptic efficacy." *Synapse* 35 (2000): 26-38.
- Savtchenko, Leonid P., and Dmitri A. Rusakov. "Extracellular diffusivity determines contribution of high-versus low-affinity receptors to neural signaling." *NeuroImage* 25 (2005): 101-111.
- Schikorski, T., and C. F. Stevens. "Quantitative ultrastructural analysis of hippocampal excitatory synapses." *J Neurosci* 17 (1997): 5858-5867.
- Scimemi, Annalisa, Alan Fine, Dimitri M. Kullmann, and Dmitri A. Rusakov. "NR2B-Containing Receptors Mediate Cross Talk among Hippocampal Synapses." *The Journal of Neuroscience* 24 (2004): 4767-4777.
- Scott, Ricardo, and Dmitri A Rusakov. "Main determinants of presynaptic Ca<sup>2+</sup> dynamics at individual mossy fiber-CA3 pyramidal cell synapses." *J Neurosci* 26 (2006): 7071-7081.
- Selkirk, Julie V, et al. "Role of the GLT-1 subtype of glutamate transporter in glutamate homeostasis: the GLT-1-preferring inhibitor WAY-855 produces marginal neurotoxicity in the rat hippocampus." *Eur J Neurosci* 21 (2005): 3217-3228.
- Semyanov, Alexey, Matthew C Walker, Dimitri M Kullmann, and R. Angus Silver. "Tonically active GABA A receptors: modulating gain and maintaining the tone." *Trends Neurosci* 27 (2004): 262-269.
- Shepherd, G. M., and K. M. Harris. "Three-dimensional structure and composition of CA3-->CA1 axons in rat hippocampal slices: implications for presynaptic connectivity and compartmentalization." *J Neurosci* 18 (1998): 8300-8310.
- Silva, M. D., T. Omae, K. G. Helmer, F. H. Li, M. Fisher, and C. H. Sotak. "Separating changes in the intra- and extracellular water apparent diffusion coefficient following focal cerebral ischemia in the rat brain." *MAGNETIC RESONANCE IN MEDICINE* 48 (2002): 826-837.
- Small, E. W., and I. Isenberg. "HYDRODYNAMIC PROPERTIES OF A RIGID MOLECULE - ROTATIONAL AND LINEAR DIFFUSION AND FLUORESCENCE ANISOTROPY." *BIOPOLYMERS* 16 (1977): 1907-1928.
- Sniekers, Y. H., and C. C. van. "Determining Diffusion Coefficients in Inhomogeneous Tissues Using Fluorescence Recovery after Photobleaching." *Biophysical Journal* 89 (2005): 1302-1307.
- Sotak, C. H. "Nuclear magnetic resonance (NMR) measurement of the apparent diffusion coefficient (ADC) of tissue water and its relationship to cell volume changes in pathological states." *Neurochem Int* 45 (2004): 569-82.
- Swanson, Geoffrey T., Sunjeev K. Kamboj, and Stuart G. Cull-Candy. "Single-Channel Properties of Recombinant AMPA Receptors Depend on RNA Editing, Splice Variation, and Subunit Composition." *The Journal of Neuroscience* 17 (1997): 58-69.
- Sykova, E. "Extrasynaptic volume transmission and diffusion parameters of the extracellular space." *Neuroscience* 129 (2004): 861-76.
- Sykova, E., and L. Vargova. "Extrasynaptic transmission and the diffusion parameters of the extracellular space." *Neurochem Int* 129 (2007): 861-876.
- Sykova, Eva. "Diffusion properties of the brain in health and disease." *Neurochemistry International* 45 (2004): 453-466.
- Sykova, Eva. "Glia and volume transmission during physiological and pathological states." *J Neural Transm* 112 (2005): 137-147.
- Sylantsev, Sergiy, et al. "Electric fields due to synaptic currents sharpen excitatory transmission." *Science* 319 (2008): 1845-1849.
- Takamori, Shigeo, et al. "Molecular anatomy of a trafficking organelle." *Cell* 127 (2006): 831-846.

- Takumi, Y., A. Matsubara, E. Rinvik, and O. P. Ottersen. "The arrangement of glutamate receptors in excitatory synapses." *Ann N Y Acad Sci* 868 (1999): 474-482.
- Takumi, Y., V. Ramírez-León, P. Laake, E. Rinvik, and O. P. Ottersen. "Different modes of expression of AMPA and NMDA receptors in hippocampal synapses." *Nat Neurosci* 2 (1999): 618-624.
- Tanaka, Hidenobu, Sonja Y. Grooms, Michael V. L., and R. Suzanne Zukin. "The AMPAR subunit GluR2 still front and center-stage." *Brain Research* 886 (2000): 190-207.
- Tanaka, Jun-ichi, et al. "Number and Density of AMPA Receptors in Single Synapses in Immature Cerebellum." *The Journal of Neuroscience* 25 (2005): 799-807.
- Tanaka, K., et al. "Epilepsy and exacerbation of brain injury in mice lacking the glutamate transporter GLT-1." *Science* 276 (1997): 1699-702.
- Tao, L., and C. Nicholson. "Maximum geometrical hindrance to diffusion in brain extracellular space surrounding uniformly spaced convex cells." *J Theor Biol* 229 (2004): 59-68.
- Tichelaar, Willem, Markus Safferling, Kari Keinanen, Holger Stark, and Dean R. Madden. "The Three-dimensional Structure of an Ionotropic Glutamate Receptor Reveals a Dimer-of-dimers Assembly." *Journal of Molecular Biology* 344 (2004): 435-442.
- Tong, G., and C. E. Jahr. "Block of glutamate transporters potentiates postsynaptic excitation." *Neuron* 13 (1994): 1195-203.
- Tovar, K. R., and G. L. Westbrook. "The incorporation of NMDA receptors with a distinct subunit composition at nascent hippocampal synapses in vitro." *J Neurosci* 19 (1999): 4180-4188.
- Traub, R. D., et al. "A possible role for gap junctions in generation of very fast EEG oscillations preceding the onset of, and perhaps initiating, seizures." *Epilepsia* 42 (2001): 153-170.
- Trommald, M., V. Jensen, and P. Andersen. "Analysis of dendritic spines in rat CA1 pyramidal cells intracellularly filled with a fluorescent dye." *J Comp Neurol* 353 (1995): 260-274.
- Trugnan, Germain, Philippe Fontanges, Danile Delautier, and Tounsia Ait-Slimane. "FRAP FLIP FRET BRET FLIM PRIM De nouvelles techniques pour voir la vie en couleur." *MEDECINE/SCIENCES* 20 (2004): 1027-34.
- Tzingounis, Anastassios V, and Jacques I Wadiche. "Glutamate transporters: confining runaway excitation by shaping synaptic transmission." *Nat Rev Neurosci* 8 (2007): 935-947.
- VanDeVen, M., M. Ameloot, B. Valeur, and N. Boens. "Pitfalls and their remedies in time-resolved fluorescence spectroscopy and microscopy." *JOURNAL OF FLUORESCENCE* 15 (2005): 377-413.
- Ventura, R., and K. M. Harris. "Three-dimensional relationships between hippocampal synapses and astrocytes." *J Neurosci* 19 (1999): 6897-6906.
- Wadiche, J. I., J. L. Arriza, S. G. Amara, and M. P. Kavanaugh. "Kinetics of a human glutamate transporter." *Neuron* 14 (1995): 1019-27.
- Wadiche, Jacques I, and Craig E Jahr. "Patterned expression of Purkinje cell glutamate transporters controls synaptic plasticity." *Nat Neurosci* 8 (2005): 1329-1334.
- Wahl, L. M., C. Pouzat, and K. J. Stratford. "Monte Carlo simulation of fast excitatory synaptic transmission at a hippocampal synapse." *J Neurophysiol* 75 (1996): 597-608.
- Wang, G. J., et al. "Dihydrokainate-sensitive neuronal glutamate transport is required for protection of rat cortical neurons in culture against synaptically released glutamate." *Eur J Neurosci* 10 (1998): 2523-31.
- Wegener, W. A., V. J. Koester, and R. M. Dowben. "A GENERAL ELLIPSOID CANNOT ALWAYS SERVE AS A MODEL FOR THE ROTATIONAL DIFFUSION PROPERTIES OF ARBITRARILY SHAPED RIGID MOLECULES." *Proc Natl Acad Sci U S A* 76 (1979): 6356-6360.
- WHO. "Epilepsy: aetiology, epidemiology and prognosis." World Health Organisation, 2001.

- Wieshmann, U. C., C. A. Clark, M. R. Symms, G. J. Barker, K. D. Birnie, and S. D. Shorvon. "Water diffusion in the human hippocampus in epilepsy." *Magn Reson Imaging* 17 (1999): 29-36.
- Wieshmann, U. C., M. R. Symms, and S. D. Shorvon. "Diffusion changes in status epilepticus." *Lancet* 350 (1997): 493-494.
- Wu, Xin-Sheng, Lei Xue, Raja Mohan, Kenneth Paradiso, Kevin D Gillis, and Ling-Gang Wu. "The origin of quantal size variation: vesicular glutamate concentration plays a significant role." *J Neurosci* 27 (2007): 3046-3056.
- Yernool, Dinesh, Olga Boudker, Yan Jin, and Eric Gouaux. "Structure of a glutamate transporter homologue from *Pyrococcus horikoshii*." *Nature* 431 (2004): 811-818.
- Zampighi, G. A., and R. S. Fisher. "Polyhedral protein cages encase synaptic vesicles and participate in their attachment to the active zone." *J Struct Biol* 119 (1997): 347-359.
- Zipfel, W. R., and W. W. Webb. *In vivo diffusion measurements using multiphoton excitation fluorescence photobleaching recovery and fluorescence correlation microscopy*. (In *Methods in Cellular Imaging*). Oxford University Press, 2001.
- Zuber, Benoit, Irina Nikonenko, Paul Klauser, Dominique Muller, and Jacques Dubochet. "The mammalian central nervous synaptic cleft contains a high density of periodically organized complexes." *PNAS* 102 (2005): 19192-19197.

# Appendix A. Two-Dimensional Monte-Carlo Model

The 2D model assumes that a single release of 3000 non-interactive point mass glutamate neurotransmitters in one time step at a specified position on a membrane surface, which then follows a random walk algorithm with uniform angular distribution and a distance  $r$  (a modifiable parameter through diffusivity  $D$ ). Both AMPA and NMDA Receptor with desensitised mechanism (Jonas *et al.*, 1993; Lester & Jahr, 1998) are implemented, and both seen as circular/spherical sites of  $100\text{\AA}$  in diameters (Tichelaar, 2004). Simple transporter mechanism implemented is a reduced scheme of Diamond 2001 (Figure 6), with assumed site diameter of  $60\text{\AA}$  (Yernool *et al.*, 2004). All state transitions are assumed to be Poisson processes and kinetic rates are listed in Table 1. Suitable variable time step (Fermi-Dirac function) is used to ensure Poisson process accuracy (i.e.  $\text{rate} \times dt \ll 0.1$ ) and walking step is comparable to site dimension (i.e.  $\sqrt{4 \times D \times dt} \times dt < \text{site radius}$ ), but also speed up simulation when particles are sparse and reaction rate becomes the limiting criterion rather than the walking step. Boundary Conditions are assumed to be absorbing to ensure the particles disperse into the surrounding neighbourhoods.

Almost all modelling parameters are allowed to be changed in the form of configuration files rather than the code itself. Some of the essential physiological parameters are set according to the literature. The 2D model environment is a dimension reduced view as we squash 20nm wide synaptic cleft into zero (Figure 35). The 80 AMPARs and 20 NMDARs (Tanaka *et al.*, 2005; Takumi *et al.*, 1999) are inserted before every simulation run in a 300nm wide circular disc, the active zone. Various number of transporter are scattered around the active zone in a manually select patch of area. Both transporters and receptors are distributed uniformly and randomly in a non-overlapping fashion in preselected areas of physiological dimensions.

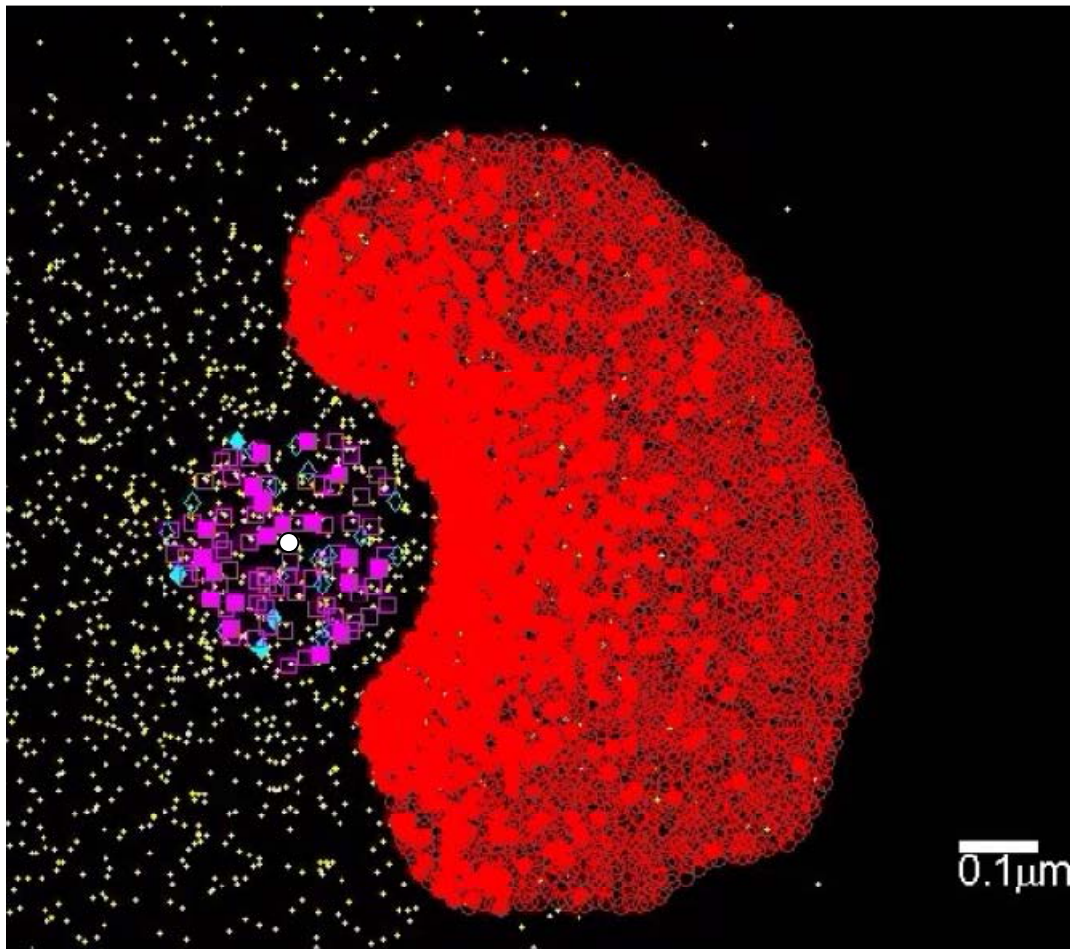


**Figure 35 Two-dimensional Monte Carlo Simulation Environment**

Snapshot at  $100\mu\text{s}$  post release from the centre of synaptic active zone (white circle) in 2D MC simulation environment, where diffusing glutamate molecules (yellow dots) bind with AMPARs (Square; Solid, opened receptor; Hollow, receptor in closed conformations), NMDARs (Diamond; Solid, opened receptor; Hollow, receptor in closed conformations) and EAAT1/2 transporters (Red circle; Solid, glutamate bound; Hollow, free). Symbol sizes are not in accordance with the scale.

Normal diffusivity of the neurotransmitter is chosen to be  $0.4\mu\text{m}^2\text{ms}^{-1}$ , as a representative value between estimated intracellular diffusivity ( $0.23\text{-}0.33\mu\text{m}^2\text{ms}^{-1}$ ) according to electrophysiology (Nielsen, 2004; and CHAPTER 4) and estimated extracellular diffusivity in CHAPTER 5.

Several scenarios were explored to test various factors' influence on synaptic responses. (Figure 36) Scenario A shows where the distance ( $d$ ) is varied at 200nm (Figure 36A Solid semicircle), 300nm, 350nm, 400nm, 450nm, 500nm and 1200nm. Scenario B depicts the circular arrangement of the transporter patch rather the normal semicircular format, where the transporter numbers are kept roughly equal at around 3000. Scenario C displays the test where the release site is moved away from the centre of the

synaptic cleft by a distance  $l = -400\text{nm}$ ,  $-200\text{nm}$ ,  $-100\text{nm}$ ,  $0\text{nm}$ ,  $100\text{nm}$ ,  $200\text{nm}$ ,  $300\text{nm}$ ,  $400\text{nm}$  and  $500\text{nm}$ . Scenario D alters the density/number of transporter sites in a normal (B) and a larger (D) concentric ring patch. Six densities were tested in both concentric patch, they are  $0\text{mM}$  (0,0 numbers for normal and larger rings respectively),  $0.05\text{mM}$  (37,207),  $0.13\text{mM}$  (107,624),  $0.25\text{mM}$  (206,1246),  $0.37\text{mM}$  (298,1744),  $0.5\text{mM}$  (406,2510). Tests were also carried out on a range of plausible diffusivity values at  $0.1$ ,  $0.3$ ,  $0.4$ ,  $0.5$  and  $0.7\mu\text{m}^2\text{ms}^{-1}$ . Single instantaneous release of  $3000$  glutamate molecules is monitored for at least  $10\text{ms}$  for AMPARs and  $100\text{ms}$  for NMDARs. At least  $200$  trials for each single case were carried out in order to get a stable population mean.

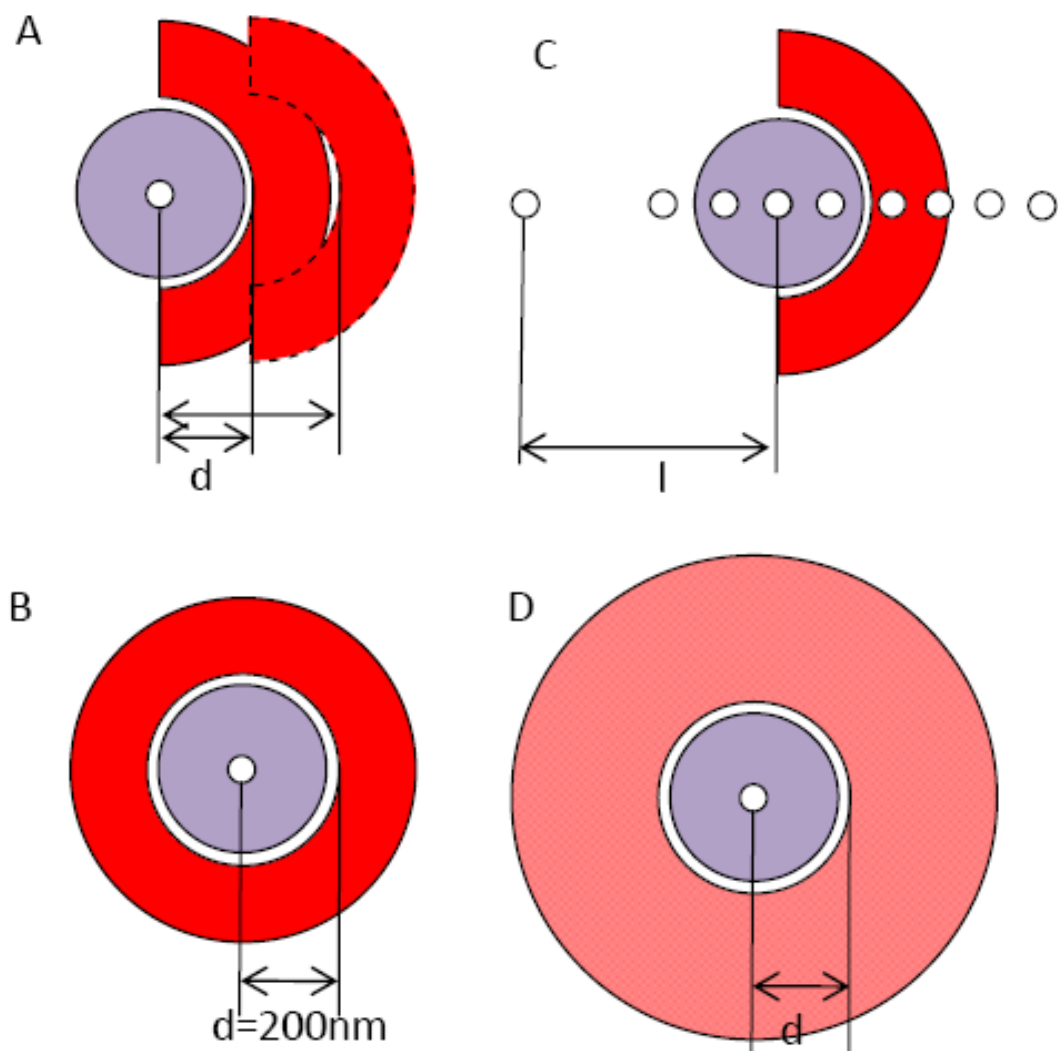


**Figure 36 2D Monte Carlo Simulation Test Scenarios**

Red Patch = Transporters; Grey Patch = Receptors; White Circle = Release Site  
 $d$  and  $l$  are labelled for later references

Simulation programme is written in MATLAB7.0 and all trials were carried out on a Pentium IV portable computer (Appendix E).

## Appendix B. Derivation of photo-bleaching factor

The photobleaching factor is assumed to be linear over the three time intervals, namely  $I_{\parallel}^a \leftrightarrow I_{\perp}^a$ ,  $I_{\perp}^a \leftrightarrow I_{\perp}^b$ ,  $I_{\perp}^b \leftrightarrow I_{\parallel}^b$ . By assuming linearity, we mean the percentage of molecule photobleached over each interval is the same. Let's define that factor to be PB, so that  $I_{\parallel}^a \cdot (1-PB) = I_{\perp}^a$ ,  $I_{\perp}^a \cdot (1-PB) = I_{\perp}^b$ ,  $I_{\perp}^b \cdot (1-PB) = I_{\parallel}^b$ . We also define a new variable  $PB_3 = (I_{\parallel}^a - I_{\parallel}^b) / I_{\parallel}^a$ . One can simply substitute  $I_{\parallel}^b$  with  $I_{\parallel}^a \cdot (1-PB)^3$ , which give  $PB_3 = 1 - (1-PB)^3$ . To rewrite it in a more useful form  $1 - PB_3 = (1-PB)^3$ .

After averaging,  $I_{\parallel}^{ave} = (I_{\parallel}^a + I_{\parallel}^b) / 2$  and  $I_{\perp}^{ave} = (I_{\perp}^a + I_{\perp}^b) / 2$ , one can work out that by substituting  $I_{\parallel}^b$ ,  $I_{\perp}^a$ ,  $I_{\perp}^b$  with  $I_{\parallel}^a$ . Hence  $I_{\parallel}^{ave} = (I_{\parallel}^a + I_{\parallel}^a \cdot (1-PB)^3) / 2 = I_{\parallel}^a \cdot (1 + (1-PB_3)) / 2 = I_{\parallel}^a \cdot (2 - PB_3) / 2$ , and  $I_{\perp}^{ave} = (I_{\parallel}^a \cdot (1-PB) + I_{\parallel}^a \cdot (1-PB)^2) / 2 = I_{\parallel}^a \cdot ((1-PB_3)^{1/3} + (1-PB_3)^{2/3}) / 2$ .

Because the difference between  $I_{\parallel}^{ave} = \int I_{\parallel}(t) dt$  and  $I_{\perp}^{ave} = \int I_{\perp}(t) dt$ , namely  $\int r(t) dt$  is very small compare to either  $I_{\parallel}^{ave}$  or  $I_{\perp}^{ave}$ , the correction factor to the first order approximation that should apply to  $I_{\perp}^{ave}$  to bring it comparable to  $I_{\parallel}^{ave}$ , is simply  $I_{\perp}^{ave} / Z = I_{\parallel}^{ave}$ . Hence  $Z = I_{\perp}^{ave} / I_{\parallel}^{ave} = [I_{\parallel}^a \cdot ((1-PB_3)^{1/3} + (1-PB_3)^{2/3}) / 2] / [I_{\parallel}^a \cdot (2 - PB_3) / 2]$ , which simplifies to  $Z = ((1-PB_3)^{1/3} + (1-PB_3)^{2/3}) / (2 - PB_3)$ .

## Appendix C. Linux Cluster Configuration

Linux operating system is high customizable which makes it ideal for custom building PC clusters for HPC (High power computing). Gentoo Linux is a Linux distribution which is based on the idea of customisability for Linux OS, where one could build on top of a few megabyte of basic Linux system to a server or workstation or anything else by choose exactly which programmes to install. Therefore it is chosen to be the base system for our cluster.

To minimise financial cost and installation time and later on upgrade and maintenance time, it was decided that a diskless cluster should be implemented. The system will only have hard disk on the master PC, where folders containing basic Linux kernel and essential library file reside for each slave which could be uploaded to the slave PC through TFTP protocol and NFS protocol. Another advantage of Linux system is that one can tune it so that recent programmes that was or is running could be buffered in the RAM; hence there is less strain on the gigabit network bandwidth.



Figure 37 PC Cluster Image

The master PC runs the TFTP, NFS, DHCP, NTP (Network Time Protocol for time synchronisation) server, and job scheduling (custom written in BASH script), MPI. In order to maintain responsiveness a Core 2 Quad (Q6600) PC is designated as the master PC, whereas all slaves are Pentium IV based with hyper-threading enabled. 32bit Linux kernel vanilla 2.6.25.11 is built for both master and slave with slaves

having only essential parts of the kernel for lightweight loading during TFTP transfer.

All slave PCs are connected to a bonded Ethernet interface (containing two gigabit Ethernet card to give load-balancing) through a 16-port Gigabit D-Link switch.

For all basic diskless cluster setup in Gentoo and other server application setups, instructions and resources are followed from the excellent guides on Gentoo user forum.

Code listing for the master\_scheduler.sh for distributing MATLAB jobs to slaves:

```
#!/bin/bash
#two input argument,function name and number of jobs
job_total=$2
sim_name=$1
#gather slave information
node_name=$(awk '/host-name/ {pos=index($3,",");print(substr($3,2,pos-3))}'
/etc/dhcp/dhcpd.conf)
node_no=$(echo "$node_name" | wc -l)
Outfile=$(date -u +%Y%m%d_%H:%M:%S_%N)_outputs.out
for i in `seq 1 $node_no`
do
    node[i]=$(echo "$node_name" | sed -n "$i'p'")
    cpuno[i]=$(ssh ${node[$i]} grep processor /proc/cpuinfo | wc -l)
    echo "slave ${node[$i]} has ${cpuno[i]} brains" >> $Outfile
    if [ ${cpuno[i]} -eq 0 ]; then
        unset node[$i]
    fi
done
node_no=${#node[*]}
echo "There are $node_no of slaves to command... Work started @ $(date -u
+%Y%m%d_%H:%M:%S)" >> $Outfile
#Allocates Jobs
#loop till finish required total allocated
current=$job_total
while [ $current -gt 0 ]
do
    j=0;
    for i in ${node[@]}
    do
        running=$(ssh $i pgrep -f MATLAB | wc -l)
        j=$((j+1))
        #running=${#temp[*]}
        torun=$(( ${cpuno[j]} - $running)
        echo "$i has ${cpuno[j]} cpus and is currently running $running jobs and has
got $torun to run"
        if [ $torun -ge 1 ]; then
            ssh $i
/home/share/ION/Computational_Model/Parallel_DM3DMC/scriptrun.sh $sim_name &
sleep 10s
```

```

        PID[$current]=$(ssh $i pgrep -fn MATLAB)
        current=$((current-1))
        if [ $current -eq 0 ]; then
            break
        fi
        echo "$current job left to distribute" >> $Outfile
    fi
done
sleep 10s
for i in `seq 1 $node_no`
do
    cpuno[$i]=$(ssh ${node[$i]} grep processor /proc/cpuinfo | wc -l)
    if [ ${cpuno[$i]} -eq 0 ]; then
        unset node[$i]
    fi
done
sleep 10s
done
echo "All jobs are distributed, waiting for slaves to finish work..." >> $Outfile
current=$job_total;
while [ $current -gt 0 ]
do
    found=0
    for i in ${node[@]}
    do
        result=$(ssh $i ps -p ${PID[$current]} -o pid=)
        if [ $result ]; then
            found=1
            break
        fi
    done
    if [ $found -eq 0 ]; then
        echo "job ID= ${PID[$current]} has finished" >> $Outfile
        unset PID[$current]
        echo "${#PID[*]} jobs left" >> $Outfile
        current=$((current-1))
    fi
    sleep 2s
done
echo "All quotas are done @ $(date -u +%Y%m%d_%H:%M:%S), slaves are taking breaks" >>
$Outfile
echo "Jobs have finished @ $(date -u +%Y%m%d_%H:%M:%S) , need supervision, read
$Outfile" | mail -s "Simulation Message From H14" K.Zheng@ion.ucl.ac.uk
exit

```

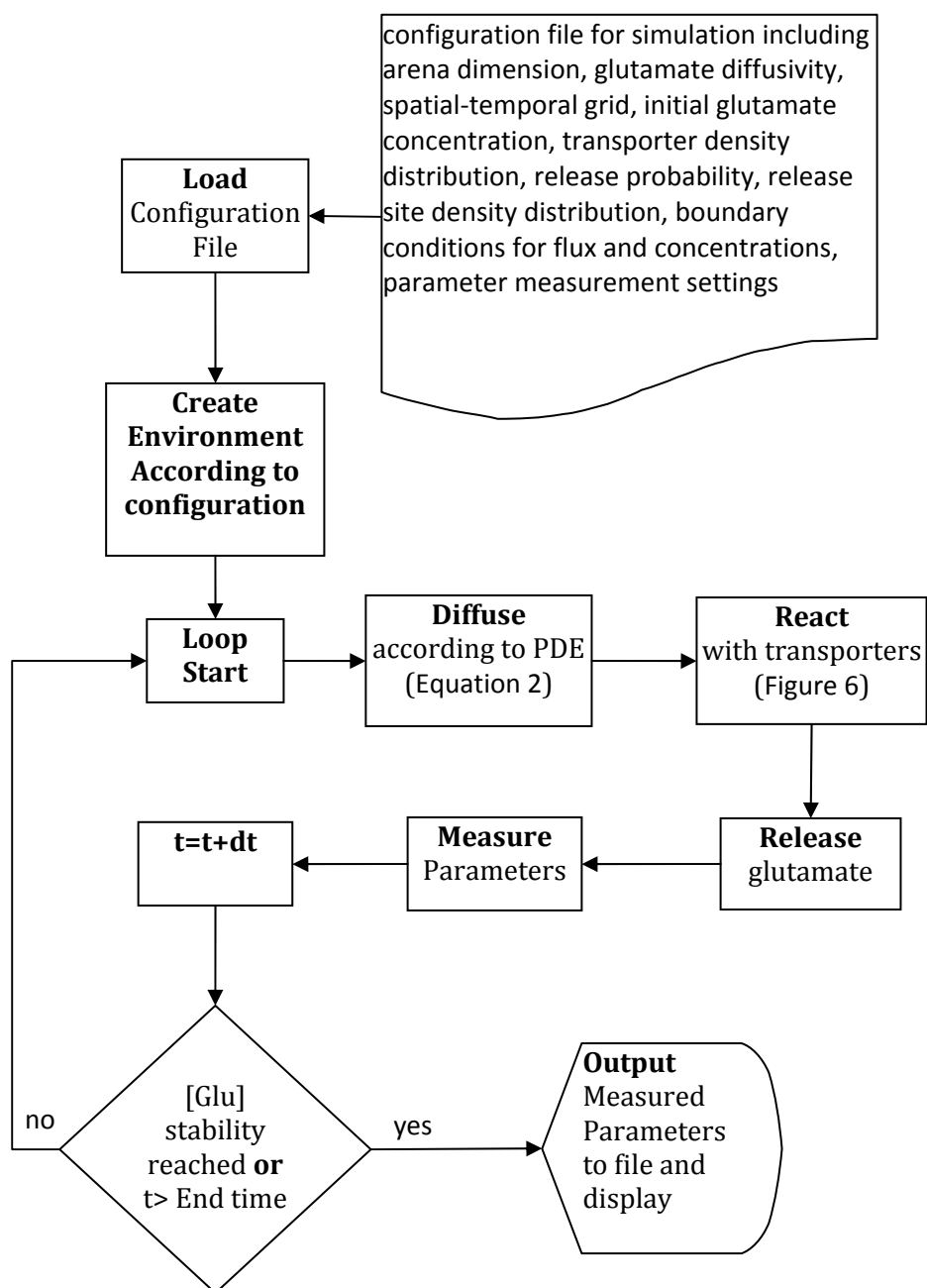
And the function call to scriptrun.sh is listed below:

```

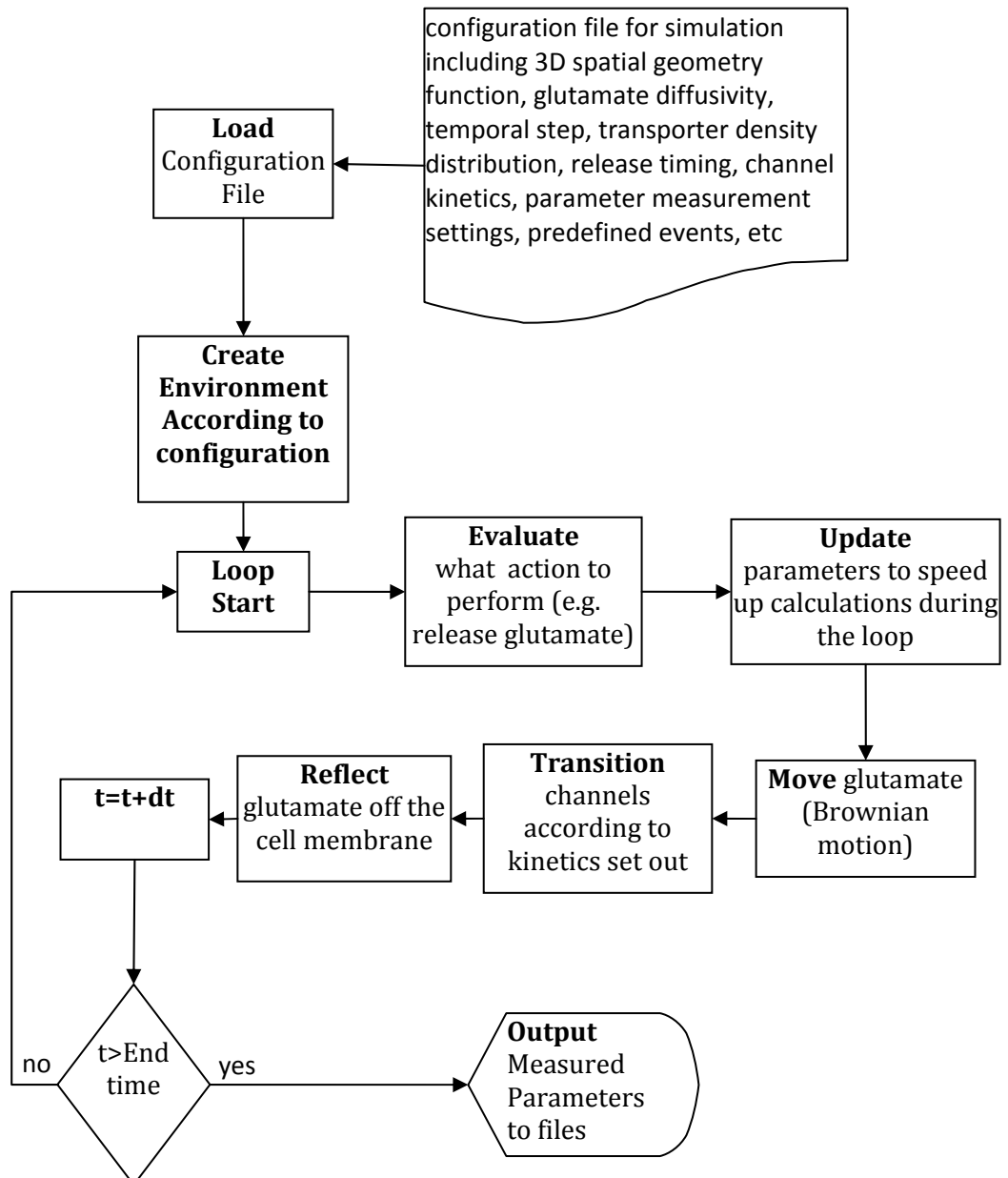
#!/bin/bash
cd /home/share/ION/Computational_Model/Parallel_DM3DMC;
MFUNC=$1
Outfile=$(hostname)_$(date -u +%y_%m_%d_%H_%M_%S_%N)_script.out
touch $Outfile
export TMW_HEARTBEAT_INTERVAL=-1
nohup /usr/local/MATLAB/bin/MATLAB -nojvm -nodisplay -nosplash -nodesktop -r $MFUNC >
$Outfile
exit

```

## Appendix D. Three-Dimensional Compartmental Model Pseudo Code

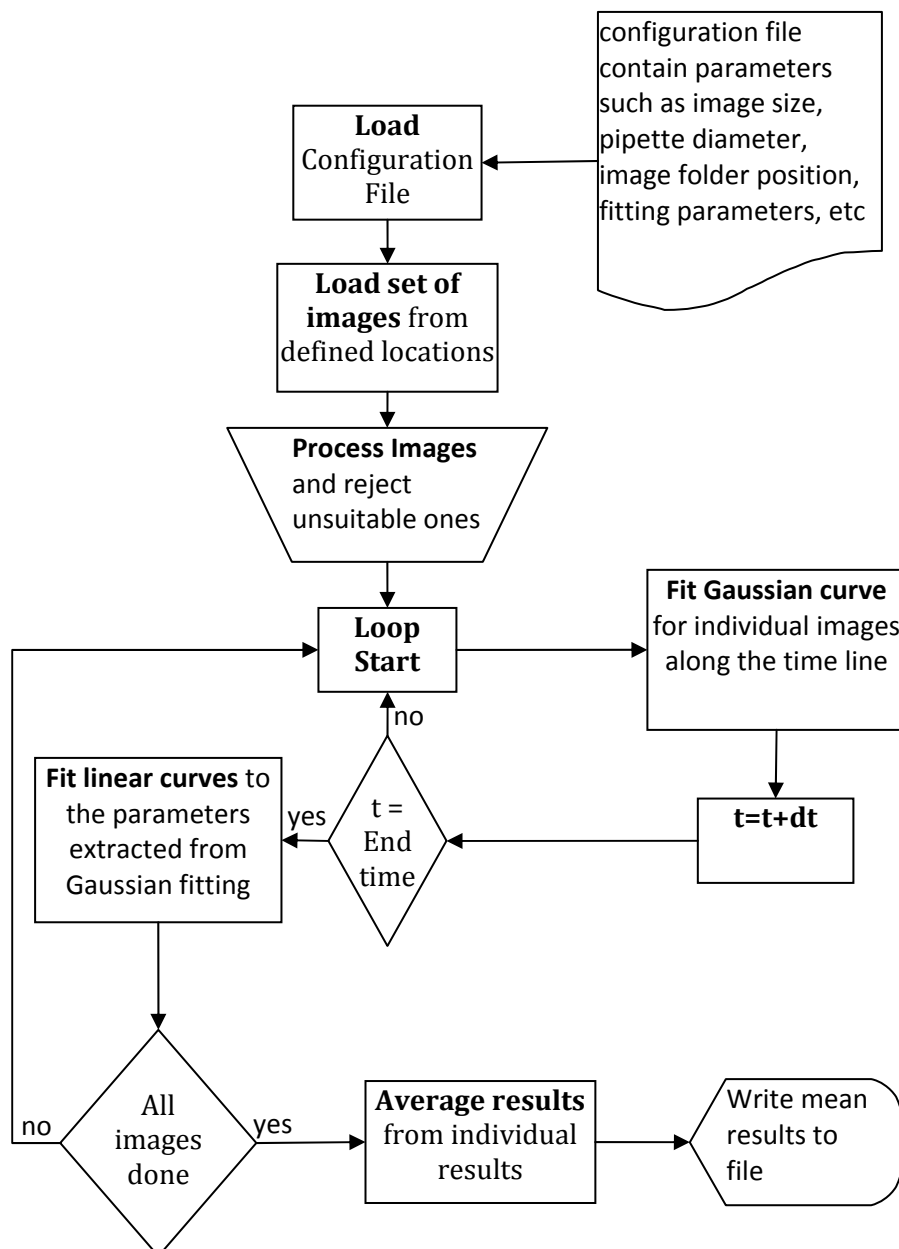


## Appendix E. Three Dimensional Monte-Carlo Model Pseudo-Code



# Appendix F. Point Source Analysis

## Pseudo-Code



# Appendix G. TR-FAIM Analysis

## Pseudo-Code

